UNIVERSITY OF CALIFORNIA SAN DIEGO

Anode Study for Achieving Higher Energy Density in All-Solid-State Batteries

A Dissertation submitted in partial satisfaction of the requirements
for the degree Doctor of Philosophy

in

Materials Science and Engineering

by

So-Yeon Ham

Committee in charge:

Professor Ying Shirley Meng, Chair
Professor Eric Fullerton, Co-Chair
Professor Zheng Chen
Professor Ping Liu

2024

The Dissertation of So-Yeon Ham is approved, and it is acceptable in quality and form for publication on microfilm and electronically.

University of California San Diego

2024

DEDICATION

To my family and friends, for their unwavering support and encouragement.

TABLE OF CONTENTS

LIST OF FIGURES

LIST OF TABLES

ACKNOWLEDGEMENTS

I would like to thank my advisor Professor Ying Shirley Meng for her unwavering support and guidance throughout my doctoral research, which has greatly contributed to my professional development. I would like to express my deepest gratitude to my committee co-chair and members, Professor Eric Fullerton, Professor Zheng Chen and Professor Ping Liu for their support and their valuable feedback.

I am grateful to work with such an amazing individual in my current solid-state subgroup, Dr. Darren Tan, Dr. Jean-Marie Doux, Dr. Jihyun Jang, Dr. Erik Wu, Ashley Cronk, Dr. Yu-Ting Chen, Grayson Deysher, Philip Ridley, Jerry Yang, Dr. Ben Huang, Jaehee Park. I could not have finished my work without your help, feedback and inspiration.

I would also like to thank colleague at LG Energy Solution, Dr. Jeongbeom Lee and Dr. Minsang Song for their unlimited support, for all the discussion made to enable the next generation technology translated to commercial level.

I would like to thank the collaborators outside my department, Dr. Elias Sebti (UCSB), Tyler Pennebaker (UCSB), Professor Raphaële Clément, Dr. Amir Avishai (USC), Dr. Keunyoung Kim (NCMIR), Dr. Eric Bushong (NCMIR), Dr. Jeff Wu (Nano 3)

Chapter 1, in part, is a reprint of the material as it appears in "S.-Y. Ham, A. Cronk, Y.S. Meng, J. Jang, Characterizing the critical challenges of Li-metal solid-state batteries: From micrometer to centimeter, *MRS Bulletin* **48** (2023) 1269–1279."

Chapter 2, in full, is a reprint of the material as it appears in "S.-Y. Ham, H. Yang, O. Nunez-cuacuas, D.H.S. Tan, Y.-T. Chen, G. Deysher, A. Cronk, P. Ridley, J.-M. Doux, E.A. Wu, J. Jang, Y.S. Meng, Assessing the critical current density of all-solid-state Li metal symmetric and

full cells, Energy Storage Materials 55 (2023) 455–462." The dissertation author was the first author of this paper, all authors contributed to this work.

Chapter 3, in full, is a reprint of the material as it appears in "S.-Y. Ham, E. Sebti, A. Cronk, T. Pennebaker, G. Deysher, Y.-T. Chen, J.A.S. Oh, J.B. Lee, M.S. Song, P. Ridley, D.H.S. Tan, R.J. Clément, J. Jang, Y.S. Meng, Overcoming low initial coulombic efficiencies of Si anodes through prelithiation in all-solid-state batteries, Nat Commun 15 (2024) 2991." The dissertation author was the first author of this paper, all authors contributed to this work.

VITA

2015 Bachelor of Science in Chemical Engineering, Konkuk University

2018 Master of Science in Chemical Engineering, Konkuk University

2024 Doctor of Philosophy in Materials Science and Engineering, University of California San Diego

ABSTRACT OF THE DISSERTATION

Anode Study for Achieving Higher Energy Density in All-Solid-State Batteries

by

So-Yeon Ham

Doctor of Philosophy in Materials Science and Engineering

University of California San Diego, 2024

Professor Ying Shirley Meng, Chair
Professor Eric Fullerton, Co-Chair

All-solid-state batteries (ASSBs) have gained lots of attention by both science and industry field. There are numerous benefits of adopting ASSB. First, because of inorganic solid-state electrolytes (SSEs), ASSBs have less safety concerns compared to the conventional liquid lithium-ion batteries (LIBs). Another reason is that, the energy density of ASSBs could exceeds that of LIBs with the premise of utilizing alloy-type or Li metal anode. Despite the extensive studies for

decades, the alloy-type, especially Si anode, and Li metal failed to achieve reasonable cyclability up to the practical level. However, the recent studies shed light on excellent compatibility of argyrodite solid electrolyte, Li6PS5Cl, and anode-free (Li metal) anode and pure Si anode.

First half of this dissertation is on the study of critical current density (CCD) of Li metal-ASSBs. The low CCD of Li metal-ASSBs hindered the practical operation of the cell, whereas inconsistent CCDs reported in academia. The variation of CCDs could be attributed to the various factors, such as temperature, solid electrolyte chemistry or pressure. The relationship between the fabrication pressure contact hold time of Li metal vs CCD is reported, elucidating the effect of controlled Li deformation on CCD. Further, the volumetric expansion of full cell configuration of Li metal-ASSB was mitigated to achieve higher CCDs at room temperature.

Alloy-type Si anode was investigated in this thesis as well. Si-ASSBs have shown promising performance without continual solid-electrolyte interface (SEI) growth. However, the first cycle irreversible capacity loss yields low initial Coulombic efficiency (ICE) of Si, limiting the energy density. To address this, we adopt a prelithiaiton strategy to increase ICE and conductivity of Si-ASSBs. A significant ICE was observed for Li1Si anode paired with lithium cobalt oxide (LCO) cathode. A high areal capacity of up to 10 mAh cm^{-2} was attained using this Li_1Si anode, suggesting that the prelithiation method may be suitable for high-loading next-generation all-solid-state batteries. The N/P ratio of Si in ASSBs showed peculiar behavior compared to liquid LIBs, which further broaden a usage of Si not only as anode but potentially as part of current collector.

Overall, this dissertation offers an understanding of high-capacity anode for ASSBs which could lead to safe and high energy density cells, one step closer to commercialization.

Chapter 1 Introduction

1.1 Growing Demands for Batteries

The global demand for lithium-ion batteries (LIBs) is anticipated to surge dramatically over the coming decade, driven largely by the growing popularity of electric vehicles (EVs). Many major car manufacturers have announced their intention to focus solely on EVs in the near future. This trend highlights the crucial role batteries in replacing fossil fuels in the mobility sector. Additionally, emerging technologies and startups are exploring the potential of battery powered aviation, which significant efforts being made to develop electric vertical take-off and landing (eVTOL) aircraft and small air taxis.

However, significant challenges remain in making battery successful for both EVs and eVTOLs, particularly in terms of increasing energy and power density. Energy density measures how much energy a battery can store per unit mass or volume, expressed in Wh/kg or Wh/L, while power density indicates how quickly energy can be delivered, measured in W/kg or W/L. The driving range of EVs could be significantly extended if the current energy density of 265 Wh/kg is increased to 500 Wh/kg. Regarding power density, eVTOLs requires extreme power demands, with a discharge rate of 15C used to simulate the power needed during the rapid climb.[1] However, such a high rate of discharge would yield low amount of viable capacity with current battery technology.

One of the major concerns with battery technology is safety. Batteries store energy through a chemical potential difference between the cathode and anode. If this separation fails, it can result in a short-circuit and thermal runaway, which is a rapid release of energy as heat. This can cause adjacent cells to catch fire, posing substantial safety risks.

Therefore, despite the current established LIB technology, there is a pressing need for new types of batteries that address limited energy/power density and safety challenges.

1.2 Towards Safer and Higher Capacity Batteries – All-Solid-State Batteries

All-solid-state batteries (ASSBs) have emerged as the next generation technology to replace LIBs to solve all the problems mentioned in the previous sections. ASSBs are structurally similar to LIBs, however, the liquid electrolyte of LIBs is replaced to solid state ion conductor, without a separator layer. Also, the solid electrolyte is incorporated in the cathode as a composite as a catholyte to make solid to solid Li ion conductive pathway. The reason behind ASSBs being a candidate to replace are mostly from two distinguish advantage coming from solid state electrolyte and anode.

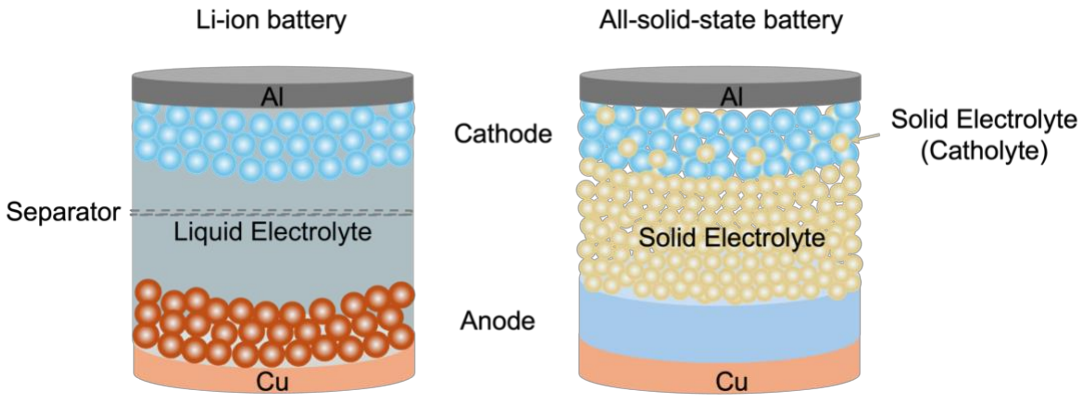

Figure 1.1 Schematics of Li-ion battery (left) and all-solid-state battery.

Using SSEs instead of liquid electrolyte comes with lots of benefits. First, the SSEs of ASSBs are intrinsically much safer compared to the liquid electrolyte because it is inflammable. Moreover, the lithium-ion transference number close to 1 contributes to the fast charging capability.

Anodes in ASSBs have shown remarkable progress recently, opening up new possibilities for battery research. Alloy and Li metal anodes, which are ideal but typically difficult to use, have been reported to exhibit stable cyclability in ASSBs. Utilizing high-capacity materials as anodes can greatly enhance the energy density of batteries. The ultimate form of ASSBs should ideally feature Li metal, anode-free, silicon anodes. Consequently, this dissertation will focus on high-capacity anodes, including Li metal and Si anodes. In this chapter, remaining challenges of Li metal anodes and the multi-length scale characterization tool to will be covered in the following section.

1.3 Lithium metal solid-state batteries

Lithium metal solid-state batteries (LiMSSBs) are currently one of the most promising next-generation energy storage strategies to enable high energy density batteries while combating the safety challenges associated with Li metal and liquid electrolytes. As the prevalence of electric vehicles (EVs) increases, the demand for better performance like longer range and faster charging times is required to make EVs more desirable than their fossil fuel counterparts.[2] Currently, state-of-the-art lithium-ion batteries have limited energy and power density originating from the use of liquid electrolyte and graphite anodes, which possess limited specific capacity (372 mAh g^{-1}) and lithiation rates.[3] Moreover, the thermal runaway issue coming from the flammable conventional organic liquid electrolyte can be mitigated by changing to non-flammable solid-state electrolytes (SSEs).[4–8] In addition, all-solid-state batteries utilizing lithium metal anodes can possibly deliver gravimetric and volumetric energy densities up to 400 Wh kg^{-1} and 900 Wh L^{-1}, respectively,[9] which can deliver longer ranges and enable currently unattainable electrified applications like electrified aircraft. The increase in energy density is due to lithium metal's high specific capacity

(3860 mAh g^{-1}) and the lowest reaction voltage (– 3.04 V vs. NHE). It also has the potential compatibility with stable SSE to combat interphase growth and mass transfer limitations present within lithium metal liquid systems.[10,11] However, in practice, the implementation of lithium metal within solid-state batteries has presented multi-scale obstacles (**Figure 1.2**), from interface to full-cell and practical level. There are numerous interfaces between each component of LiMSSBs, such as cathode composite and catholyte SSE, lithium metal and SSE, and the SSE layer itself. These interfaces can be subjected to chemical and electrochemical instability [12,13] leading to irreversible lithium loss, large resistance growth, and chemo-mechanical degradation of SSE films. It will eventually cause low usable current densities, limiting charge/discharge rates and power densities for practical applications as well as dendritic growth. At the full cell level, accumulated interface level challenges and larger scale volume change originating from the imbalance of cathode/anode expansion/shrinkage during the cycling [14,15] create the pores and dead region where it cannot participate in the reaction, which leads non-uniform current and thus dendritic lithium metal growth which can generate the short circuit behavior. Further, transitioning from lab-scale pellet-type full cells to larger form factors like pouch cells requires careful consideration in material selection and compatibility as chemo-mechanical degradation from anode and cathode volume change in addition to interfacial instability are exacerbated as areal capacity increases. All these combined problems at various length scales contribute to the cell failure of LiMSSBs. Without deconvoluting individual factors of cell degradation by identifying the root cause, the realization of LiMSSBs is questionable. Therefore, characterization strategies are imperative to diagnose cell failure and facilitate the development of analysis methods to aid in the material selection, design, and improvement of all-solid-state lithium metal batteries.

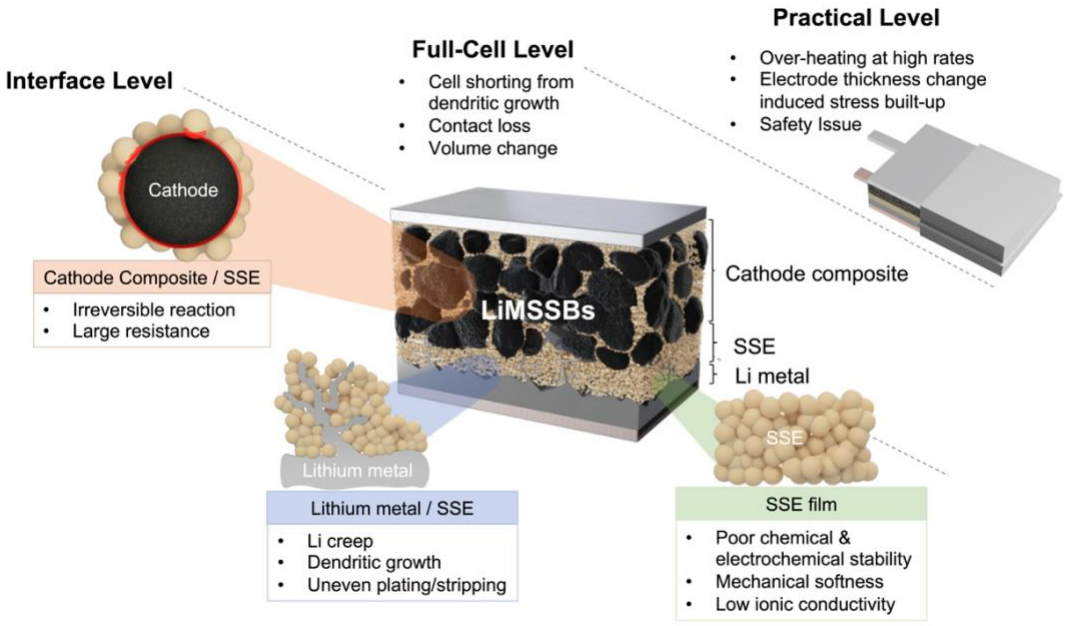

Figure 1.2 Schematics of the list of multi-scale challenges for LiMSSBs to overcome from interface molecular level to practical cell level.

1.3.1 Issues for lithium metal solid-state batteries

One of the limiting factors of solid-state versus conventional liquid is lithium-ion transport within the electrodes. Liquid electrolytes can easily percolate through porous electrodes whereas in solid-state, lithium-ion transport is limited by solid-solid diffusion. An ideal SSE would exhibit high bulk ionic conductivity and low electronic conductivity, while also maintaining good contact and deformability with the active materials and cathode/anode interfaces. With the discovery of $Li_{10}GeP_2S_{12}$ (LGPS) a superionic electrolyte with ionic conductivity competitive with conventional liquid electrolytes at room temperature (12 mS cm^{-1}),[16] interest in SSE development surged. Other SSE candidates like Li_2S-P_2S_5 sulfide ceramic glasses were also reported with ionic conductivity higher than liquid electrolytes of up to 17 mS cm^{-1}.[17] Despite the advances in SSE development from an ion conduction perspective, other material properties should be considered critically for performance like interfacial stability. For instance, despite their high ionic

conductivity, sulfide-based SSEs demonstrate narrow electrochemical windows, nonetheless the reduced degradation products exhibit desirable properties that allow lithium passivation at lower potentials.[13,15,18] This makes sulfide-based SSEs a usual choice as an anolyte or as a separator layer within the solid-state system. In order to be implemented within the cathode composite, coating cathode active materials with electronically insulating and lithium-ionically conducting layers is one widely used strategy to minimize interfacial degradation.[19–21] The use of more stable SSEs such as chlorides and oxides is another strategy to minimize interfacial degradation at the cathode potentials but usually at the cost of ionic conductivity [22,23] or deformability.[24] Therefore, in addition to SSE selection, methodologies to analyze the (electro)chemical stability at the cathode or anode interface are necessary to develop better solid-state batteries.

The mechanical property of lithium is one of the most important aspects to consider when building LiMSSBs. This is because the reported yield strength values of polycrystalline lithium metal in micrometer size dimensions are below 1 MPa in compression mode,[25] which is way smaller pressure than common cycling conditions of solid-state cells. With this in mind, the most important mechanical property of lithium metal in solid-state battery setup would be the continual deformation under persistent compression loads, which is called “creep”. Creep plays a crucial role when forming intimate contact between lithium and the SSE layer, affecting the critical current density. The creep rate is dependent on several factors such as applied pressure, temperature, and lithium thickness.[26] The study examining all these factors on lithium foil showed that applied pressure of less than 2 MPa was enough to induce significant creep deformation for all samples. On the other hand, an appropriate creep rate could facilitate better contact between lithium metal and adjacent layers. In fact, some studies reported that the stack pressure of solid-state batteries induced creep contributions to a higher fraction of contact between lithium metal and SSE both in

the computational model [27] and in the experiment [28]. However, recent research on Li metal showed that Li metal with submicron size could support over 200 MPa, indicating there is clear difference in yield strength between bulk Li metal and nano-meter scale Li whisker.[29] The result implies the mechanical properties of bulk Li in anode side and dendritic Li within SSE should be carefully considered when designing LiMSSBs.[30] Also, the mechanical properties of SSE itself are another important factor to consider, since the densification of the SSE layer also contributes to the critical current densities, where pores and grain boundaries of SSE could act as preferable sites for lithium dendrite growth.[31] The complexity of the plastic deformation of Li and grain boundaries and pores of SSE layer all contribute to dendrite propagation leading to the cell shorting. Accordingly, examining the mechanical properties and degradation of lithium and SSE is vital to understanding the performances and degradations of LiMSSBs.

Low critical current density (CCD) is a widely accepted problem of LiMSSBs. The CCD is often defined as the current density at which lithium dendrite penetrates the SSE separator and makes the cell fail by short-circuiting. The reported room temperature CCD of LiMSSB is limited to 1mA cm^{-2}, which is way lower than a commercial requirement. The reported CCD values in literature widely vary since CCD is dependent on various factors such as cell stack pressure, plating capacity, cell component chemistry, and areal capacity. The mechanism of dendritic lithium growth is still under study but it is closely related to Li/SSE interfacial void formation which leads to subsequent porosity, surface roughness, and contact loss. There are many reports showing lithium dendrites nucleate at interfacial voids and cracks at the lithium metal and SSE interfaces. The interfacial void formation originates from the imbalance between lithium-ion fluxes at the Li/SSE interface. In the LiMSSB cycling condition with certain stack pressure, there are three lithium-ion fluxes involved: 1) $J_{Lithium\text{-}ion\ migration}$: lithium-ion migration driven from applied

current, 2) $J_{Lithium\text{-}ion\ diffusion}$: Self-diffusion of lithium atoms driven by the concentration gradient, 3) $J_{Lithium\ creep}$: Lithium creep driven by the stack pressure. To suppress the void formation and subsequent lithium dendrite growth, maintaining the balance is crucial.[32] Therefore, Chapter 2 will discuss the evaluation of CCD in Li metal cells and propose strategies to prevent cell shorting by balancing the mentioned fluxes.

1.3.2 Interface-level (micrometer-level) characterization

1.3.2.1 Chemical and Electrochemical Stability of SSEs

Beyond ionic conductivity, the stability of the SSE at the anode or cathode interface, within the cathode composite, and the separator layer itself is crucial for realizing highly energy-dense solid-state batteries. In an ideal case, the SSE should exhibit good stability at both electrodes, facilitating lithium transport as the cell is cycled. If the SSE is not (electro)chemically stable, degradation products can be formed either from chemical or electrochemical reactions. These formed products can potentially be detrimental to the entire system, creating growing interphase layers that could be insulative and hinder lithium transport. To evaluate the (electro)chemical stability, electrochemical techniques like linear sweep voltammetry and cyclic voltammetry are typically employed to extract the electrochemical stability window as done so in prior work.[18,33–35] In these works, cell set-up and electrode configurations are critical in order to obtain accurate results (**Figure 1.3**). Han et al. highlight the importance of mixing the SSE with high surface area conductive material within the composite electrode in order to facilitate sufficient interfacial reactions and accurately obtain electrochemical stability windows of LGPS and $Li_7La_3Zr_2O_{12}$ (LLZO) SSEs, expanding on previous stability results (**Figure 1.3a, 1.3b**).[16] Electrochemical stability and redox activity of argyrodite Li_6PS_5Cl (LPSCl) and garnet LLZO were also

investigated by Schwietert et al. where constant current charge and discharge were used to perform differential capacity analysis (**Figure 1.3c**). These results coupled with ^{31}P NMR and first-principles calculations were used to further identify redox species after (de)lithiation, where their electrochemical stability was determined by the oxidation and reduction potentials of S and P for LPSCl and O and Zr for LLZO. Some SSEs exhibit reversible or irreversible behavior, depending on the operating voltage and the resulting decomposition products that are formed. The reversibility of LPSCl was also studied by Tan et al. where ^{31}P and ^{7}Li NMR coupled with X-ray photoelectron spectroscopy (XPS) was employed to confirm decomposition products at certain cut-off potentials. The relationship between electrochemical stability windows and resulting decomposition products are significant factors that affect the overall performance of LiMSSBs.

1.3.2.2 Characterizing SEI/CEI Interface

The (electro)chemical stability of SSEs determines the interfacial reactions that occur at the cathode and anode potentials. Electrochemical impedance spectroscopy (EIS) can be used to study the impedance of interfacial layers formed at the surface between SSE and active materials, and allow the characterization of the solid electrolyte interface (SEI) or cathode electrolyte interface (CEI). Typically, EIS is used to study the resistance of a system or resulting ionic conductivities of SSEs as shown in **Figure 1.3d**, for example, Bron et al. used equivalent circuit fitting results to deconvolute impedance contributions from doping LGPS with low-cost elements like Al, Sn, and Si.[36] EIS was also employed to study the pressure-dependent SEI resistance of garnet LLZO electrolytes when in contact with lithium metal.[37] Krauskopf et al. reported negligible interfacial resistance (0 Ohm cm^{-2}) when LLZO was pressed at 100 MPa, owing these results to

good contact geometry where the interface remains morphologically stable at current densities of 100 μA cm^{-2} (**Figure 1.3e**).

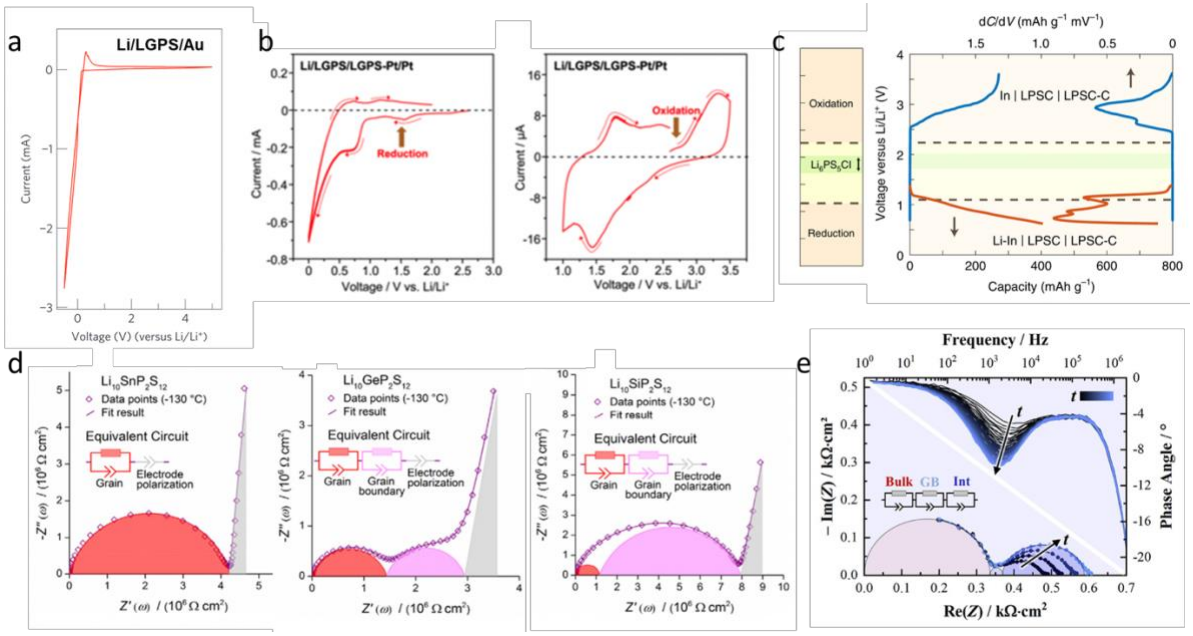

Figure 1.3 a) Cyclic voltammetry of LGPS using Li/LGPS/Au cell configuration. Reproduced with permission[16]. b) Cyclic voltammetry scans of LGPS using Li/LGPS/LGPS-Pt/Pt cell configuration showing the difference in obtained electrochemical stability depending on cell set up. Reproduced with permission[16]. c) Constant current charge and discharge and dQ/dV of Li-In/LPSCl/carbon cells. Reproduced with permission [33]. d) Nyquist plots of doped LGPS electrolytes with various dopants Sn and Si showing respective impedance contributions. Reproduced with permission[1]. e) Nyquist plots of LLZO electrolyte showing resistance growth with lithium metal stripping. Reproduced with permission[37].

Beyond indirect tools like impedance quantification, direct evidence like visualizing SEI growth is a powerful tool that allows the direct observation of interfacial layers, decomposition products, and lithium dendritic growth. Wang et al. used a combination of EIS with Time of flight Secondary Ion Mass Spectrometry (ToF-SIMS) high-resolution imaging and depth profiling of the $Li_{1.15}Y_{0.15}Zr_{1.85}(PO_4)_3$ (LYZP) electrolyte to relatively quantify the interfacial species after in contact with lithium metal and study their distribution. This work demonstrated that even highly

stable SSEs can still promote dendritic growth, for this case, LYZP reduced to form high electronic conductivity metallic Zr, and its distribution was mapped in 3D (**Figure 1.4a**).[12] Operando analysis is another tool to investigate interfacial dynamics in real time. Davis *et al.* used operando XPS and video microscopy to investigate the interfacial decomposition of LGPS and LPSCl in anode-free cells, studying the difference in degradation properties and how it either facilitates interfacial growth or stabilizes (**Figure 1.4b**). As lithium was plated on the LPSCl, the growth of Li_xP and Li_3P was confirmed which eventually stabilized. While for the LGPS case, in addition to Li_xP, Li_3P, metallic Ge was also detected which is electrically conducting and continually consumes lithium.[38] This work shed light on SSE selection for anode-free configurations and how degradation products influence battery performance.

In addition to studying the anode interface, SSE compatibility with the cathode interface is also important. Jang et al. developed a methodology to use EIS in order to study the chemical compatibility of LPSCl with the high voltage $LiNi_{0.5}Mn_{1.5}O_4$ (LNMO) cathode material, where an interlayer was formed even before cycling (**Figure 1.4c**). In that work, SSE selection in addition to cathode coatings to mitigate CEI growth was highlighted, enabling the improved performance of the LNMO cathode within the all-solid-state system.[39] Interfacial stability of the CEI can also be investigated using XPS, which allows the local determination of chemical species at the surface. Auvergniot et al. compared the performance of the sulfide-based LPSCl electrolyte with $LiNi_{1/3}Mn_{1/3}Co_{1/3}O_2$ (NMC111), $LiMn_2O_4$ (LMO), and $LiCoO_2$ (LCO) cathodes (**Figure 1.4d**). It was observed that the LMO cathode exhibited the worst cycling performance versus NMC and LCO when paired with LPSCl. XPS results from the S 2p and P 2p spectra showed clear signs of decomposition of the LMO-LPSCl system even in the pristine state, reinforcing the chemical incompatibility and reactivity of LPSCl at the LMO surface. XPS and SEM confirmed the

decomposition of LPSCl into elemental sulfur, polysulfides, P_2S_x species, and phosphates.[40] These decomposition results were further supported by Cronk et al. where degradation of LPSCl at the carbon-coated $LiFePO_4$ (LFP) interface was ascribed to its poor performance and lack of studies within inorganic all-solid-state batteries. XPS, EIS, XRD, and Raman spectroscopy were used to confirm the formation of insulative decomposition products, while the use of a more stable SSE such as Li_2ZrCl_6 (LZC) was employed to mitigate CEI growth and enable high rate and long cycling of LFP in all-solid-state batteries.[35]

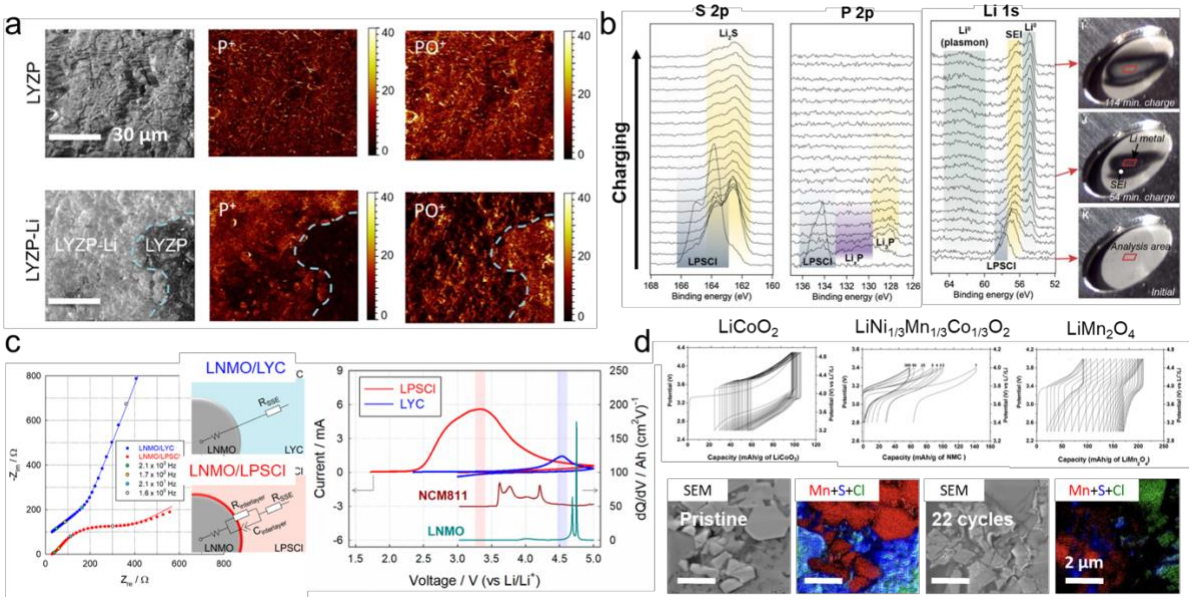

Figure 1.4 a) TOF-SIMS mapping of LYZP and LYZP-Li. Reproduced with permission[12]. b) (Left) *Operando* XPS of LPSCl and lithium metal at different states of charge (Right) corresponding optical images of the cell. Reproduced with permission[38]. c) (Left) Nyquist plot from EIS measurement and the equivalent circuit. (Right) CV curves of LPSCl/C (red) and LYC/C (blue) composites all-solid-state half-cells and the first cycle dQ/dV plots of two cathodes (NCM811 and LNMO) half-cells in the liquid electrolyte. Reproduced with permission[39]. d) (Top) Voltage profiles of LCO, NMC111, and LMO using LPSCl electrolyte (Bottom) SEM images of LMO cathode in a pristine state and after 22 cycles showing LPSCl decomposition. Reproduced with permission[40].

1.3.2.3 Mechanical Properties of SSEs

In addition to ionic conductivity and (electro)chemical stability, the mechanical properties of SSEs are another important feature of LiMSSBs. This is because good interfacial contact is required between cathode active materials, SSE, and anode to facilitate uniform current density and lithium diffusion between all layers. Therefore, easily deformable, mechanically compliant SSEs are desirable for not only fabrication ease but also to accommodate volume change within the cathode composite or at the anode interface. Previous reports found that higher shear modulus prevents dendrite formation and ductile SSEs better accommodate stress-strain.[41] However, characterizing the mechanical properties of SSEs can be challenging due to their instability in ambient conditions requiring air-tight measurements. Atomic force microscopy and indentation is a popular method to determine the local mechanical properties of materials including hardness and has been evaluated in prior work.[42] Due to the air-tight requirements of SSEs, these techniques are usually done in the glove box. One non-destructive method is the ultrasonic pulse method, which is a technique that enables the determination of shear modulus, Poisson's ratio, elastic modulus, and bulk modulus by measuring the time it takes for vibrational energy to travel through a medium, measuring the velocity. Sakuda et al. employed the ultrasonic pulse method to study the elastic modulus of the garnet-type LLZO and sulfide glasses ($75Li_2S{\cdot}25P_2S_5$).[43] Their work confirmed the high elastic modulus of oxide electrolytes and why sintering is usually required to create densified oxide pellets. In addition, they found that the Li_2S content heavily influenced the elastic modulus, where a higher molar content increased the SSE stiffness. It was also found that doping the sulfide glasses with lithium halides reduced the elastic modulus, facilitating more deformable electrolytes.[44] That being said, densification can also be evaluated using a scanning electron microscope-focused ion beam (SEM-FIB) where SSE is compacted under fabrication pressures

and milled to determine the porosity. This method was used by Cronk et al. where cross-sectional SEM-FIB validated the hypothesis that halide SSEs exhibit less porosity and more intimate contact.

1.3.3 Cell-level (millimeter-level) characterization

1.3.3.1 Dendritic Lithium Growth

For lithium dendrite growth being the detrimental part of LiMSSBs, characterizing lithium dendrite has been extensively studied with various equipment. However, because the initiation and propagation of dendrite is buried in the SSE layer, the characterization should be conducted in a way that involves either sensing lithium dendrite in a non-destructive way or cutting the cell to expose the dendrite. Marbella et al. used ^{7}Li nuclear magnetic resonance (NMR) chemical shift imaging (CSI) to probe lithium microstructure changes and chemical information.[45] **Figure 1.5a** shows the cell data from constant current plating and stripping at the same current density of 0.5 mA cm^{-2}, and stopped at different times. By correlating top cell voltage data and bottom ^{7}Li CSI data, the evolution of lithium dendrite growth and its microstructural change was observed without damaging the cell. Neutron depth profiling (NDP) is another non-destructive tool to investigate lithium concentration in solid electrolyte separators. Han et al. performed NDP on solid-state batteries with three different SSEs and monitored the dynamic evolution of lithium profiles.[46] SSEs with relatively higher electronic conductivity, LLZO and Li_3PS_4, showed an increase in lithium concentration with longer plating of lithium (**Figure 1.5b**). This higher lithium NDP count increased with higher temperatures due to the higher electronic conductivity at elevated temperatures. This study showed that electronic conductivity also plays a crucial role in regulating dendrite growth in solid-state batteries, thus when selecting the SSE, not only the lithium-ion ionic

conductivity but also the electronic conductivity of SSE itself should be a crucial parameter to take into consideration. Since the buried interface hinders the observation of dendrite growth, the direct morphological observation of lithium dendrite of contact loss requires the cross-sectional cut using FIB. There are various kinds of ion beam sources for FIB; Ga^+ is a more conventional source and the plasma such as Xe^+ or Ar^+ are emerging sources for their higher milling rate and less redeposition with certain materials.[47] Lu et al. used the plasma-FIB to cut the whole lithium metal layer and observe the Li/LPS interface.[48] The study showed the evolution of contact loss with stripping capacity accumulation, which will lead to uneven plating of lithium for the next cycle and eventually become dendrite. The Ga^+ source also could be used in investigating lithium metal interphase in a cryo-environment to minimize the beam-induced damage as Cheng et al. did in the cryogenic transmission electron microscopy study of the Li/lithium phosphorus oxynitride (LiPON).[49] In the study, the cryo-Ga^+ FIB milling was performed to preserve the Li/LiPON interphase, and the lift-out process was also demonstrated in the cryo-environment utilizing the redeposition as the connecting agent between the lamella and the lift-out probe (**Figure 1.5c**).

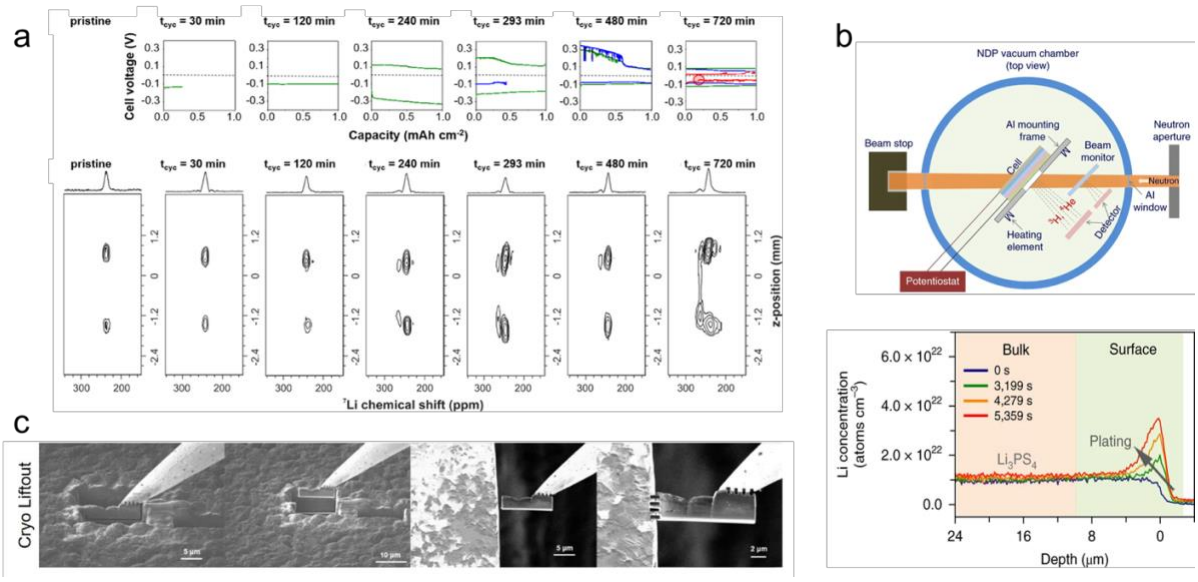

Figure 1.5 a) The constant current plating and stripping (top) correlated with the ^{7}Li NMR CSI (bottom) which shows the lithium dendritic growth. Reproduced with permission[45]. B) The experimental set-up of NDP for probing lithium in the solid electrolyte layer (left) and lithium concentration from the depth profiling. Reproduced with permission[48]. c) The demonstration of cryo-lift out for lithium metal electrode and LiPON interface. Reproduced with permission[49].

1.3.3.2 *Operando* Characterization

The *operando* study of LiMSSB shed light on a better understanding of how the cell actually operates, correlating the electrochemical data to chemical and morphological characterization. X-ray tomography (XTM) is useful in a way that it is non-destructive and could be measured *in situ* or *operando* to provide porosity, surface area, tortuosity, and volume change with the appropriate cell design.[50] However, the contrast in the images is dominated by the X-ray attenuation coefficient of each material,[51] missing chemical information. There have been many studies that applied XTM to battery research, especially synchrotron radiation operando X-ray tomography (SRXTM) could be used to directly observe the nanometer- to micrometer-level reaction. Lewis et al. performed operando SRXTM to investigate the interphase evolution during the plating and stripping of lithium metal in Li/$Li_{10}SnP_2S_{12}$ (LSPS)/Li solid-state cell.[52] The 3D-

reconstructed and segmented renderings are shown in **Figure 1.6a**, showing the voids were formed to induce contact loss as more lithium was stripped. The 2D X-ray images were used to investigate the interface of Li/LSPS further, showing void growth and reduction at 1 to 4 mA cm^{-2} current density range. Another X-ray-based technique; energy dispersive X-ray diffraction (EDXRD) offers chemical information of LiMSSBs. *Operando* EDXRD was used to investigate the structural stabilities of $Li_{6.6}Ge_{0.6}Sb_{0.4}S_5I$ and FeS_2 [53] where cathode composite consisted of FeS_2/$Li_{6.6}Ge_{0.6}Sb_{0.4}S_5I$/Carbon additive paired with Li-In as anode. The diffraction contour plot of the full cell was shown in **Figure 1.6b** top right, showing the preferred orientation of the large crystallites of $Li_{6.6}Ge_{0.6}Sb_{0.4}S_5I$. EDXRD was interpreted both by spatial position and time, for instance, the (220) reflection of $Li_{6.6}Ge_{0.6}Sb_{0.4}S_5I$ was compared in intensity from different positions (**Figure 1.6b** bottom left) and peak shift as a function of time (**Figure 1.6b** bottom right). In solid-state cell setup, especially in LiMSSB, the stack pressure of the cell is a crucial parameter to control.[54] However, one thing we need to consider is controlling the cycling pressure of the LiMSSB since the volume expansion of lithium metal is severe as it is plated as lithium metal. Therefore, *operando* electrochemical pressiometry gives us a reasonable insight into how to control the actual cycling pressure of the full cell. The recent study relating the critical density of LiMSSB to cell pressure change during cycling demonstrated that the higher cycling pressure would induce the early cell shorting, therefore, the cell cycling pressure should be actively controlled to minimize the cycling pressure change.[28] In **Figure 1.6c**, The cell with springs to maintain constant cycling pressure showed only 0.2 MPa pressure change whereas the fixed gap cell suffered 2 MPa of pressure change.

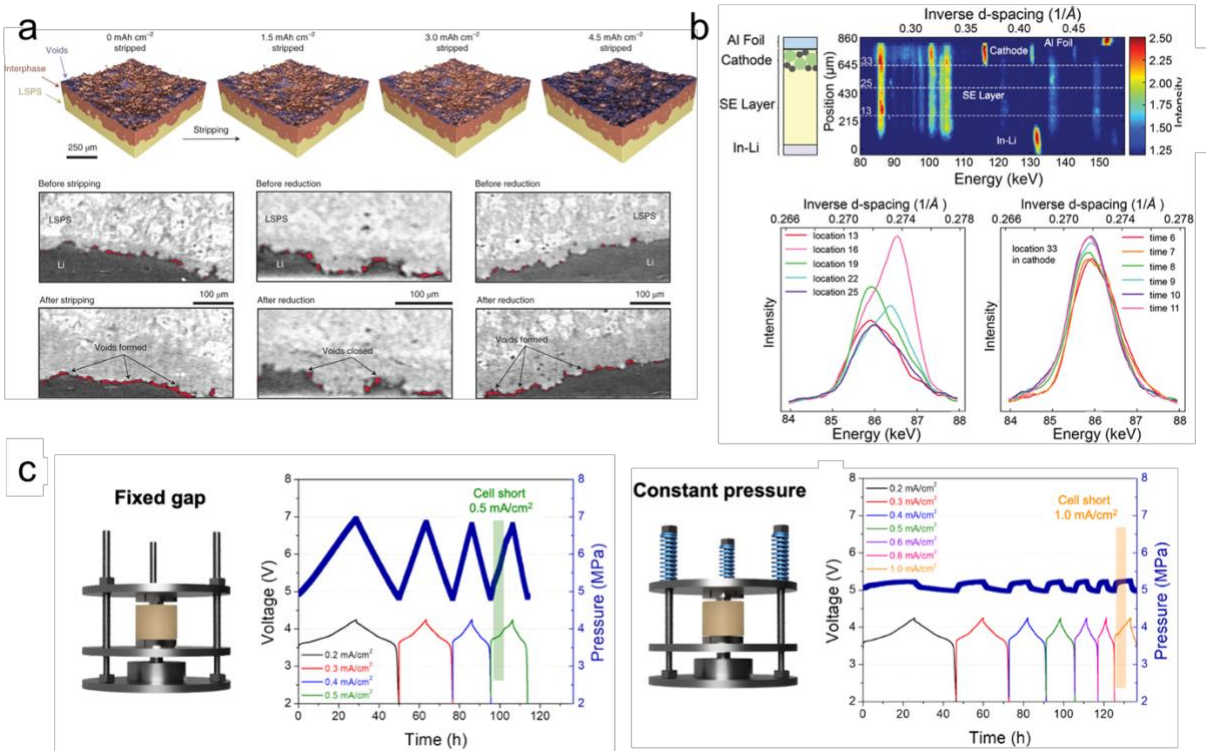

Figure 1.6 a) 3D reconstructed and segmented scans of Li/LSPS interphase (top) and 2D X-ray images showing the contact loss. Reproduced with permission[52]. b) The diffraction contour plot using EDXRD of LiMSSB (top) and the XRD spectra of specific energy range as a function of spatial position (bottom left) and time (bottom right). Reproduced with permission[53]. c) The *operando* electrochemical pressiometric measurement for the fixed gap (left) and the constant pressure setup (right). Reproduced with permission[28].

1.3.4 Practical-level (centimeter-level) characterization

1.3.4.1 Operando Characterization on Real Cells

Monitoring the battery during operation is a high-demand technique since it is directly correlated to the safety of the battery. In the practical-level cells, the volume change and contact loss would get more severe since they operate for much higher capacity than the lab-scale cells. Unlike liquid electrolyte acting as buffer even after the volume change, LiMSSBs rely on solid-solid contact, which leads to contact loss and higher local current density. Therefore, further understanding of the true chemo-mechanical properties of solid-state batteries is crucial, where

traditional battery management systems' voltage, current and pack temperature information could not deliver. Note that the literature discussed in the practical-level section is not limited to the LiMSSB but a broader spectrum of technologies that could be applicable for investigating LiMSSB. This is because the majority of LiMSSB studies so far are limited to the lab-scale level, thus characterizing the practical-level SSB is one of the future direction to enable Li metal anode in the market level cells.

The optical Fiber Bragg grating (FBG) sensors are more advanced sensing technology in a way that they could be used to probe heat and stress evolution inside the batteries. The working mechanism of optical fiber is that the photo-induced FBG sensor acts as a reflector for a specific wavelength (Bragg wavelength, $\lambda_B = 2n_{eff}\,\Lambda$). Any changes in temperature (T), pressure (P), and strain to FBG sensor results in the shift of Braff wavelength, induced by the change in n_{eff} or Λ.[55] In fact, the study of *operando* temperature monitoring 18650 cells compared the implanted FBG and thermocouple's response as the cell cycle.[56] In **Figure 1.7a**, the temperature difference between FBG measure internal temperature and the thermocouple measure external temperature was shown. At a lower rate of 0.5C (yellow shaded), the temperature difference between the two sensors was almost identical. However, as the cycling rate got higher, the temperature difference between the two sensors got preeminent. Figure 6c showed the clear trend of increased discrepancies from 0.95 ^{o}C for 1C to 3.71 ^{o}C for 2C discharge. This result indicates that a FBG sensor would be a more accurate option to assess the temperature change in higher-rate cycling. FBG sensor could be used to evaluate the stress/strain measurement at the surface and inside the battery. Blanquer et al. performed an extensive study on *operando* stress monitoring in both liquid and solid-state electrolytes with the FBG fiber embedded within the $Li_{0.6}In$ electrode, showing the Bragg wavelength shift induced by the cell's stress change.[57]

1.3.4.2 Morphology Study on Real Cells

For characterizing the whole pouch cell, a different length scale measurement tool is needed. The computed tomography mentioned in the previous section is all limited to a reduced-size *operando* cell set-up to be measured in a synchrotron setup. The synchrotron setup with high photon flux and monochromatic beam energy profile enables the nano-meter scale resolution and segmentation, however, it is far away from applicable to investigate the real scale pouch cell since it requires miniaturized cell setup. The lab-scale micro-CT has the advantage of still being able to deliver high spatial resolution with a reasonable sample stage size. The study performed micro-CT on 402035-size pouch cells and demonstrated the full multi-scale imaging capability (**Figure 1.7b**).[58] The scale of the scan varied from the full cell level scan with 9 μm resolution to the particle-level scan with a resolution of 340 nm. This research highlights how powerful CT could be in the battery field to investigate micro-to-cell-level phenomena.

Another tool to characterize the practical cells in a non-destructive way is to utilize the ultrasonic instrument. Due to the high sensitivity to mechanical properties and porosity of materials, ultrasonic technology has been adopted to investigate the state of charge[59], metal defect detection[60], and wetting[61] of the batteries. Yi et al. demonstrated the capability of ultrasonic tomography to detect a defect of metal inside the pouch cell where the change in amplitude of the sound wave is the indicator for the presence of defect. In **Figure 1.7c**, the point where amplitude intensity dropped, blue regime in the middle of the pouch, is the Cu defect points. Beyond this defect, the sound wave gained back the amplitude (black dotted area) and pass across the rest of the pouch, indicating the defect did not absorb the sound waves.

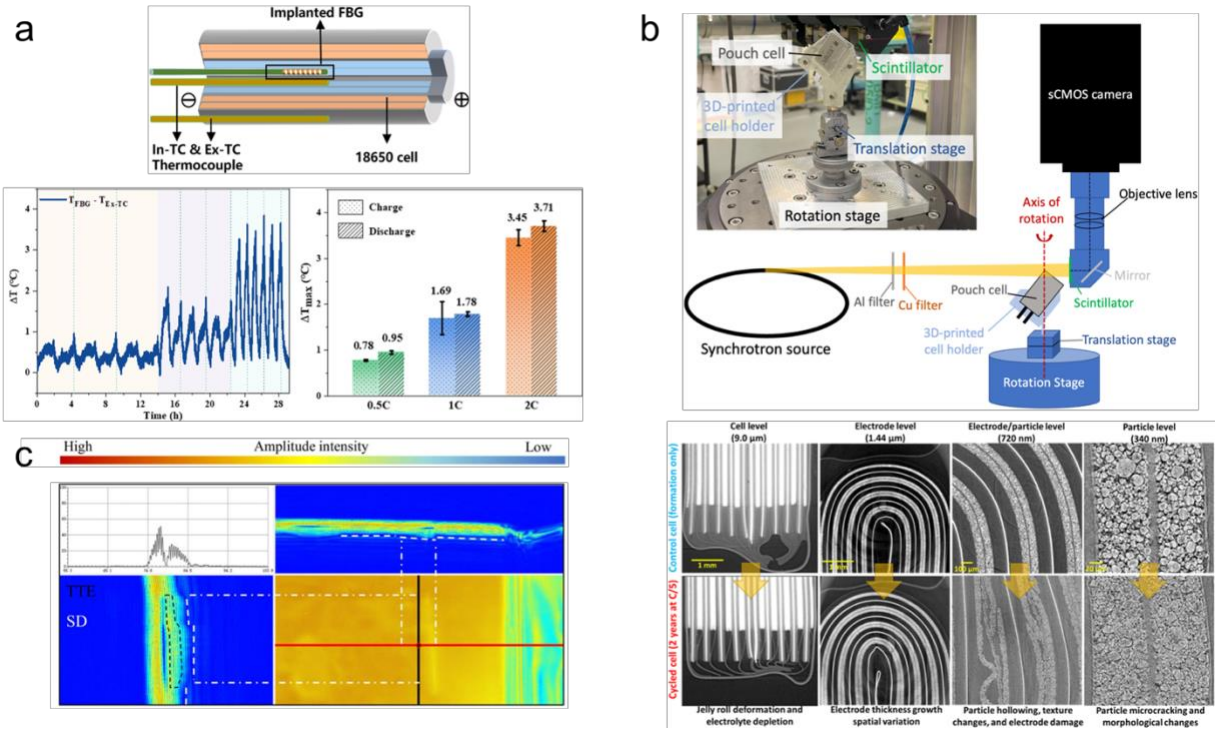

Figure 1.7 a) Comparison of the thermocouple and FBG measured temperature of the 18650-cell at different cycling rates. Reproduced with permission[56]. b) The multi-scale 3D reconstruction from X-ray CT on 402035-size pouch cell. Reproduced with permission[58]. c) Ultrasonic reflection images of Cu-foil defects at the anode side of the pouch cell. Reproduced with permission[60].

1.3.5 Summary and perspective of characterizing lithium metal solid-state batteries

Realizing high energy dense solid-state batteries is one of the most pressing environmental and technological challenges posed to the energy storage community. Solving the major issues currently known will ultimately demand perspectives from various disciplines and skillsets. This comprehensive review paper has shed light on the critical analysis of LiMSSBs, with a particular focus on the challenges and opportunities arising from interface-, cell-, and practical-level components. As we strive to unlock the full potential of these advanced energy storage systems, it becomes evident that collaborative efforts for overcoming the obstacles within the materials community are essential for driving innovation and progress.

1. The interfaces in LiMSSBs have been identified as key elements influencing the overall performance and stability of the system. Throughout this review, we have explored how these interfaces introduce new challenges, such as dendrite formation, interfacial resistance, and limited ion diffusion, and how we analyze those challenges for pursuing commercial-level consideration. By leveraging interdisciplinary approaches and fostering collaboration, we can devise innovative solutions to manipulate and engineer the interfaces, paving the way for enhanced performance and safety of LiMSSBs.
2. From an industry perspective, it is imperative to emphasize the implementation of non-destructive and post-modern advanced testing and analyzing methods to ensure the integrity and reliability of LiMSSBs. By adopting methodologies introduced in this review paper, industry professionals can gain valuable insights into the internal structure and performance of batteries.
3. To accelerate learning and progress in the field of LiMSSBs, building comprehensive databases and promoting correlative characterization approaches are paramount. A centralized database that consolidates data from various researchers will serve as valuable resources. Furthermore, adopting correlative characterization techniques that combine multiple analytical methods will yield a more in-depth understanding of several levels of issues, and thus, the impact on battery performance. This integrative approach will provide a more accurate representation of complex interfacial phenomena and accelerate the development of innovative materials and designs.

The analysis of LiMSSBs presented in this review paper emphasizes the need for collaborative efforts. By collectively addressing the challenges posed by various scale issues including materials, electrodes, cells, and large-scale systems, we can propel the advancement of

LiMSSBs and revolutionize energy storage technologies. Together, we embark on a journey of discovery and innovation, shaping a sustainable future for energy storage that holds great promise for global sustainability and prosperity.

Acknowledgement

Chapter 1, in full, is a reprint of the material as it appears in "S.-Y. Ham, A. Cronk, Y.S. Meng, J. Jang, Characterizing the critical challenges of Li-metal solid-state batteries: From micrometer to centimeter, *MRS Bulletin* **48** (2023) 1269–1279." The dissertation author was the first author of this paper, all authors contributed to this work.

Chapter 2 Assessing Critical Current Density of Li metal ASSB

2.1 Introduction

Lithium metal batteries, with their promise of high energy density, have gained much attention in recent years due to the high energy densities achieved through the use of Li metal anodes with high theoretical capacity (3860 mAh/g) and the lowest electrochemical potential (−3.04 V vs Standard Hydrogen Electrode) [62]. However, it still presents a myriad of challenges including poor Coulombic efficiency from continued irreversible reaction with liquid organic electrolyte and Li dendritic growth resulting in an abnormal safety issue [63]. All-solid-state Li metal batteries (Li-ASSBs) have recently emerged with the intrinsic advantages of the absence of organic materials which can react as resources of combustion and inhibition subsequent electrolyte decomposition [64]. However, Li-ASSBs are also often limited by low critical current densities (CCDs). The CCD can be defined as the certain current density (mA/cm^2) at which a cell failure occurs when the growth of Li dendrite from the Li metal anode reaches the cathode side through the solid-state electrolyte (SSE) separator making a short circuit between cathode and anode, which results in vigorous self-discharge and thus safety issue in a real cell 3]. Extensive research on Li-ASSBs has resulted in architectures that can achieve 1000 cycles at 3.4 mA/cm^2 at 60°C by enabling dendrite-free Li metal anode [65]. Although high CCDs are obtained at elevated temperatures which is comparable with conventional lithium metal batteries having liquid electrolytes, achieving improved room temperature performance needs further investigation. Interestingly, the CCDs of Li-ASSBs reported in the literature vary widely, as summarized in Figure 2.1. While CCD is dependent on the cell chemistry, cell stack pressure, and plating capacity, there are still large CCD variations reported even for similar cell configurations [66,67], and showed the wide range of CCDs even in our work in which the same configuration was used (the variable

here will be discussed later). This indicates that there are vital parameters during cell fabrication which have not yet been considered or compared in the previous literature. Nonetheless, general trends can be observed throughout all the Li-ASSB CCDs reported. First, it is clear that cells under elevated temperature operation exhibit higher CCDs compared to those at room temperature. This is widely attributed to the improved diffusion kinetics and favorable mechanical properties that promote uniform Li metal plating [68,69]. However, if the room or near-room temperature remains to be the favorable operating condition for practical Li-ASSBs, greater focus should be placed on increasing the CCD without the use of elevated temperatures.

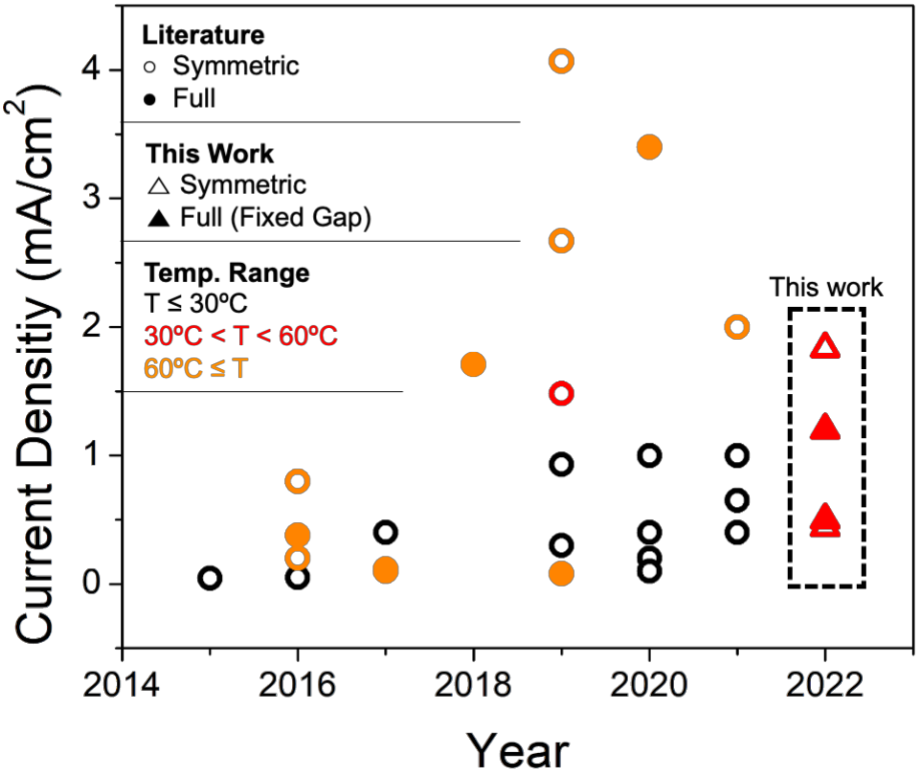

Figure 2.1 Current densities of all-solid-state Li metal cells reported in the literature and this work. The symbol shapes indicate the cell type (empty circle for symmetric cell [69–83], filled circle for full cell [65,77,84–86]) Please note that there are large variations even in our work which will be discussed later (empty triangle for symmetric cell and filled triangle for fixed gap operated full cell). The color of symbols denotes the cell cycling temperature.

When comparing cell architectures, studies using only symmetric cells [69–83] often report higher CCDs compared to full cells [65,77,84–86] at a similar cycling temperature. While the reason for this disparity is not yet understood, it is clear that high CCD values reported in the literature using symmetric cell configurations cannot be reproduced in full cell formats at room temperature 28]. As a result, some full cell performance reports adopt elevated temperature (>55°C) to demonstrate cyclability, citing the need to overcome slow diffusion kinetics at the cathode-solid electrolyte interface [90]. However, this explanation is inconsistent with studies reporting high current densities (>5.0 mA/cm^2) operations at room temperature using similar composite cathode and alloy-based anodes such as lithium-indium or silicon anodes [91]. One plausible explanation was rationalized through the misinterpretation of the cell shorting voltage features. Yang *et al*. described this as the "fake stable" phenomena, where symmetric cell polarization curves are easy to be misinterpreted as stable when in fact a short circuit has already occurred [92]. In such scenarios, a typical flat voltage curve is still observed even when cycled at high current densities (>10 mA/cm^2), where polarization originated from the ohmic resistance of the electron pathway within the shorted circuit. This misunderstanding cannot occur in a full cell where the cell voltage is determined by the state-of-charge of the cathode electrode, thus any occurrence of a short circuit would manifest as an obvious voltage fluctuation from the typical cathode charge curve. Lewis *et al.* also proposed the need to consider the areal capacity difference used in symmetric cell versus full cell tests, where the cell short phenomenon was found to only occur when an areal capacity of > 3 mAh/cm^2 for lithium plating and stripping was used [93]. This value is far more than most areal capacities used in symmetric cell tests, which typically use long hours of plating and stripping with < 1 mAh/cm^2 areal capacity [89]. There have been studies to mitigate the cell shorting by improving Li metal and SSE interface. Su *et al.* demonstrated that using graphite on the Li side would prevent chemical

reaction between SSE and Li and also serve as mechanical constriction to enable high pressure cycling [87]. Another approach was to form more stable SEI by introducing polymer electrolyte initiator [94] and adding Li_xSiO_x-enriched layer [95]. Li metal dentrite could form within solid electrolyte layer if the electronic conductivity is not low enough. Han *et al.* studied the Li deposition within the various SSE layers. [46] The group demonstrated that Li dendritic growth within the electrolyte layer was not significant at room temperature due to the low electronic conductivity. The electrolytes used in the research were LLZO and Li_3PS_4, having the electronic conductivity of $5.8 \cdot 10^{-8}$ to 10^{-7} S/cm. The electronic conductivity of Li_6PS_5Cl (LPSCl) used in our study was $1.78 \cdot 10^{-8}$ S/cm (Figure 2.2), lower than LLZO and Li_3PS_4. Therefore, due to the lower electronic conductivity of LPSCl, there is low changce of forming Li dendrite from the electronic pathway of electrolyte layer. In addition, stack pressure is one of the most important factors that dictate a CCD of Li-ASSB. Previous studies have found that relatively small changes in stack pressures can greatly affect the CCD, where it was reported that the CCD improves with increasing stack pressure, within a pressure range of 0.4 – 7 MPa [96,97]. However, the stack pressure on a Li-ASSB cannot be exceedingly high because that can induce both mechanical short due to Li deformation along with separator layer or an electrochemical short-circuit during Li metal plating, as shown in our previous work [54]. Yan *et al.* also showed the adjustment of stack pressure could resolve void formation by the Li deformation due to the low modulus characteristic of Li metal [98]. Interestingly, the symmetric cell shows much less volume change during cycling since the volumetric expansion arising from Li plating is compensated at the counter electrode which undergoes stripping simultaneously. However, this is not the case in full cell configurations, where a large amount of volumetric expansion due to Li plating cannot be compensated for the cathode side during de-intercalation. Thus, dynamic stack pressure effects on CCD during cycling must be

investigated, but most studies only have adopted fixed gap cell setups where cell stack pressure is defined before cell operation. Given the stack pressure effects on CCD, it is reasonable to think that variable stack pressures in full cells can result in vast disparities in CCD findings compared to symmetric cells.

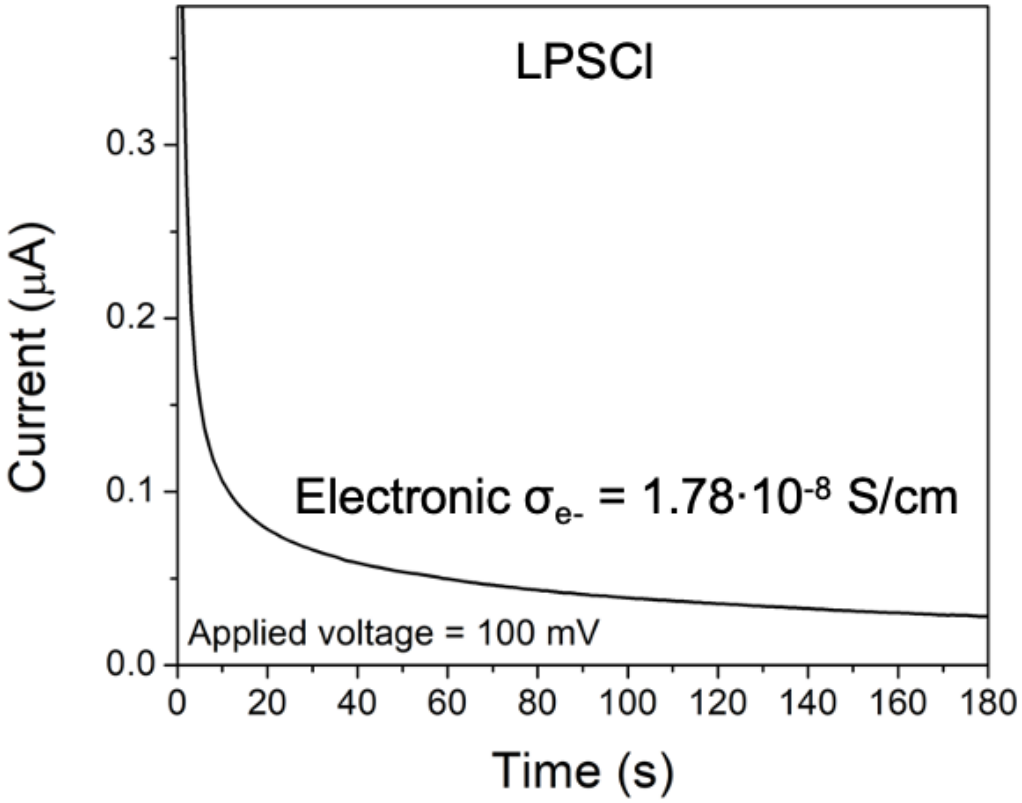

Figure 2.2 Direct current polarization of Li_6PS_5Cl (LPSCl) solid state electrolyte used in this study. The electronic conductivity of LPSCl was calculated to be 1.8×10^{-8} S/cm.

In this work, we discuss the stack pressure factors governing CCDs of both Li metal symmetric and full cells using common Li-ASSB cell configurations, Li | LPSCl | Li symmetric cell and NCM811 | LPSCl | Li full cell. We demonstrate that, among the fabrication and operation parameters, the contact time between Li and SSE while fabrication can be also the critical factor which can dramatically affect the CCD values in symmetric cells. In addition, we also systemically

addressed the root cause of CCD disparities between symmetric and full cells through the *operando* pressure monitoring while cell preparation and cycling. Finally, we reveal that the use of a constant pressure cell design can release pressure variation-driven stresses inside the cell while cycling which helps to achieve a higher CCD in Li-ASSBs operating near room temperature.

2.2 Material and methods

2.2.1 Materials preparation

Li_6PS_5Cl (LPSCl, NEI Corporation, USA) was used for solid-state electrolyte (SSE) separator layer and cathode composite preparation. For cathode composite purpose, the LPSCl particle size was reduced using EMAX ball mill (Retsch, Germany). The ball milling was conducted for 2 hours at 300 rpm, using anhydrous xylene as a medium. Vapor grown carbon fiber (VGCF) was purchased from Sigma Aldrich (Graphitized, Iron-free), and dried overnight at 160°C under vacuum to remove moisture. NCM811 (LG Chem, Republic of Korea), coated with a boron-based layer, was used as received. Cathode composite was prepared by hand-mixing using a weight ratio of NCM811: LPSCl : VGCF = 66 : 31 : 3. Li metal (FMC, USA) foil was cleaned by scratching of the oxide layer and subsequently punched into 0.785 cm^2 area.

2.2.2 Materials Characterization

Versa 510 (Zeiss/Xradia) X-ray microscope was used to investigate computed tomography (CT) of Li metal symmetric cell, with an objective of 20X, a source voltage of 80 kV and a power of 6.5 W, using the LE2 filter. The 360-degree scan was conducted in 15 sec exposure setting, for 2401 projections. The reconstruction of data was performed with Amira 2019.1 (ThermoFisher Scientific). After the reconstruction, the 3D view of inside was shown using box cutting function

of Amira 2019.1 software. The solid-state cell was built in custom-made 2 mm internal diameter drilled PTFE rod. The reduced size cell was required for X-ray CT setup for placing X-ray source as close as possible to the specimen yielding smaller voxel size and better resolution. FEI Scios Dualbeam (ThermoFisher Scientific) was used for cross-sectional images. The sample transferred was performed using air-tight transfer arm from Ar-filled glovebox to FEI Scios Dualbeam chamber for no air exposure during the transfer process. After the sample mount, liquid nitrogen and the heat exchanger was set to perform cryogenic ion beam milling and electron beam imaging to minimize the Li damage. The ion-beam milling to prepare the cross-section of samples were performed using Ga^+ source. The sample was milled at 30 kV and 65 nA, and cleaned at 30 nA and 15 nA afterwards. All the electron beam imaging was done using 5 kV and 0.1 nA settings.

2.2.3 Electrochemical Characterization

Two titanium rods were used as current collectors at each end of the Li metal. The solid-state cell was fabricated by first putting 75 mg of LPSCl in a 10 mm inner diameter polyether ether ketone holder, which was then compressed between two titanium rods at 370 MPa. For Li metal symmetric cells, punched Li metal was inserted on top and bottom of as-fabricated LPSCl pellet. After enclosing solid state cell of Li-SSE-Li using titanium rods, the cell was pressed at 25 MPa to facilitate better contact between the Li metal and SSE interface for 1 min. to 24 hr. The cells were released to 5 MPa before cycling starts. For a constant pressure setup, blue dye springs (McMaster-Carr, 1804N16) were placed between top plate and nuts for all three screws. Springs were selected based on two criteria: (i) Maximum load of spring (53 lb) should be larger than load from cell cycling pressure. The cell load was calculated based on 5 MPa for the area of 0.785 cm^2 cell. The calculated load was divided by three since the load is divided by three springs, yielding

29.4 lb of load for each spring (ii) Spring rate should be high enough not need to be compressed too much to achieve certain pressure. With the spring rate of 5.5 lb/mm in this work, 5.35 mm compression is needed to achieve 5 MPa. The full cell configuration follows the same protocol except one Li side is replaced with cathode composite. Cathode composite loadings for full cell ranged from 6.4 mg/cm^2 to 51.0 mg/cm^2. All cell cycling were performed at 40°C using the compact muffle furnace (MTI KSL-1100X) in the Argon-filled atmosphere glovebox. The battery cells were cycled using a Neware Battery cycler and analyzed with BTS900 software. During the cycling, in-situ home-made load reader was used to get the pressure reading every 10 sec. For the EIS cell, the 13 mm diameter plunger (area of 1.33 cm^2) was used to fabricate Li | LPSCl | Li cell. 300 mg of LPSCl was compressed at 370 MPa to make the pellet and Li chip was inserted on both end of the pellet. EIS measurements were conducted using Solartron 1260 impedance analyzer for Li | LPSCl | Li symmetric cell every 20 minutes after setting the cell stack pressure to 25 MPa. The frequency range was from 10 MHz to 0.1 Hz, with an applied AC potential of 10 mV. Direct current polarization was conducted to measure the electronic conductivity of LPSCl by applying the voltage of 100 mV for 3 min.

2.3 Results and Discussion

2.3.1 The critical current densities of Li metal symmetric cells

The current fabrication process for the Li metal cell, schematized in Figure 2.4a, consists of three steps: 1) densifying the LPSCl pellet at 370 MPa, 2) adding Li metal foils on both ends of the cell and 3) pressing at 25 MPa briefly to ensure good Li metal/SSE contact. Lastly, the pressure is then released to 5 MPa for the cell cycling. These protocols were described in our previous work

[54] and the *operando* pressure monitoring was conducted with our custom-built pressure recording system (Figure 2.3**).**

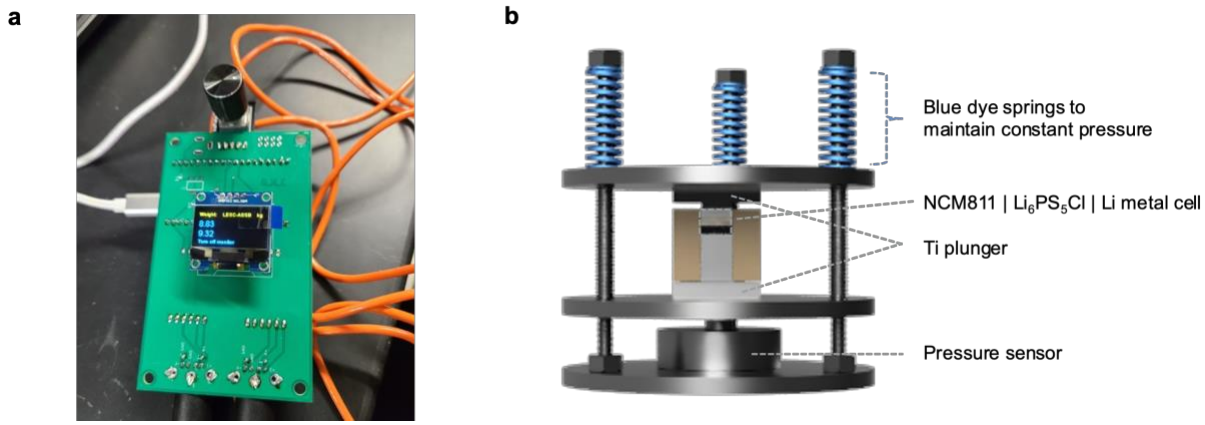

Figure 2.3 a) The custom-built pressure monitor used in this work. Pressure values were read every 10 seconds during the cycling of cells. b) Schematic diagram of constant pressure cell setup used in this work.

While the amount of compaction pressure used to fabricate ASSBs is routinely reported, the amount of time pressure applied when the Li metal anode is added and thus, the degree of Li metal deformation and uniformity has never been reported in the previous reports. The degree of Li metal deformation will affect the degree of contact and uniformity at the Li metal/SSE interface. To verify the validity of our pressure control setup, the stack pressures of the Li symmetric cell were monitored during both the initial contact at 25 MPa and the subsequent plating/stripping cycling at 5 MPa. Figure 2.4b shows that the pressure drop during the initial contact was severe, where stack pressures dropped from 25 MPa applied initially to 21.1 MPa after 24 hours. Subsequently, the cell was released to 5 MPa and started plating/stripping, during which little to no change was observed (Figure 2.4b, yellow shaded). The cycling data after setting to 5 MPa will be discussed later. To rule out any effects of different thermal expansion coefficients from various cell components, the stack pressures of an empty cell and the standard symmetric cell were

monitored and compared (Figure 2.4c, d). From the pressure trends (24-hour monitoring at room temperature and 40°C), both cells showed a rapid pressure drop during the first 30 minutes, losing 2.2 MPa (room temperature) and 5.6 MPa (40°C) during the initial 30 minutes, followed by a gradual decrease in pressure after one hour. The amount of pressure drop after 24 hours is smaller at room temperature (Figure 2.4c) compared to at 40°C (Figure 2.4d), which indicates a larger amount of Li deformation under elevated temperature conditions. This is consistent with the lower yield strength of Li at higher temperatures [99], which facilitates deformation and is consistent with our observations. The Li symmetric cell pressure trend highlights two important points: i) When 25 MPa of stack pressure is applied during cell fabrication, Li metal deformation occurs, and saturation of the deformation is observed after 10 hours. ii) The pressure during the plating/stripping of the Li metal symmetric cell remains unchanged at all times.

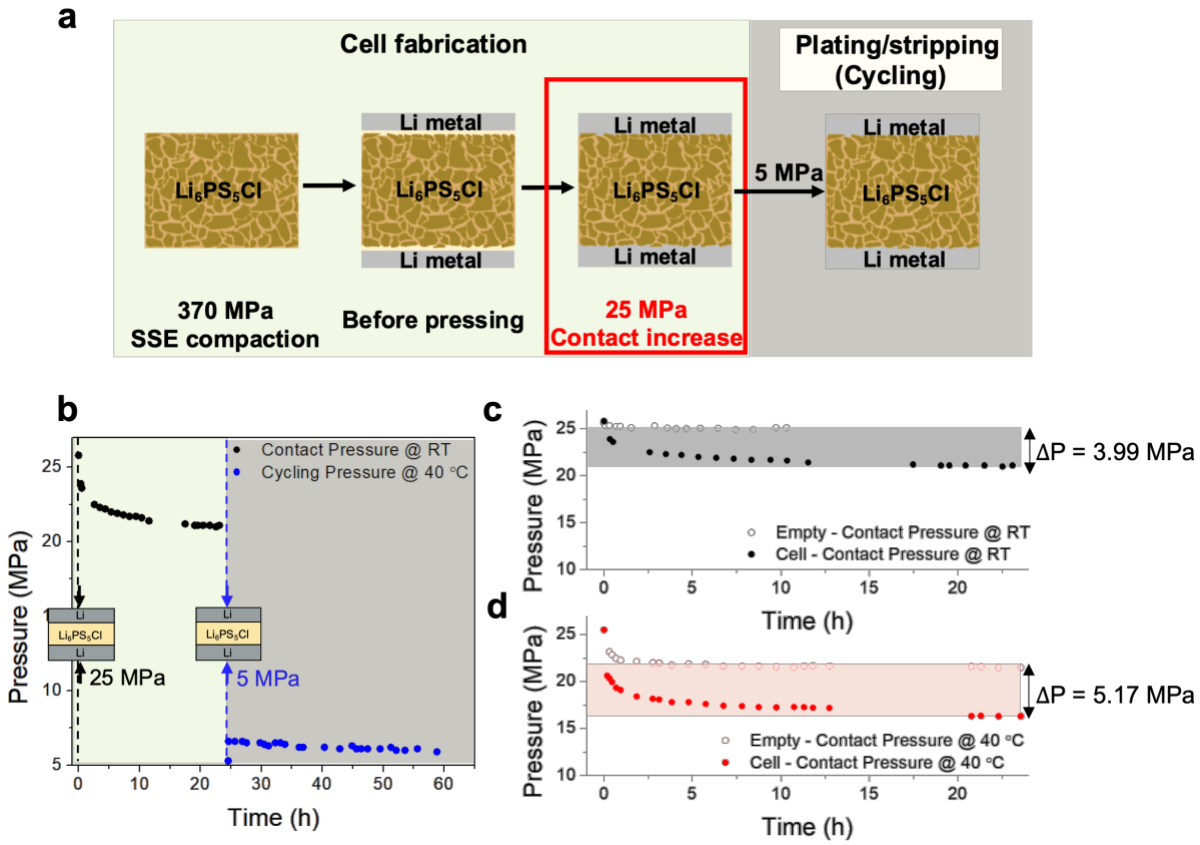

Figure 2.4 a) Schematic showing the fabrication protocol of Li metal symmetric cell, where 25 MPa is applied to improve the Li metal/SSE contact interface. b) Pressure monitoring during contact hold after applying 25 MPa at room temperature for 24 hours (green) and plating/stripping at 5 MPa and 40°C (yellow). Pressure monitoring of empty plunger cell and Li metal symmetric cell after applying 25 MPa at c) room temperature and d) 40°C for 24 hours.

Following pressure monitoring during contact hold time, ramp tests (a stepwise increase of the constant current plating/stripping of lithium) of the symmetric cells were conducted (Figure 2a). This experiment allows us to evaluate the CCD of Li metal in a Li | LPSCl | Li symmetric cell and compare it to the literature. However, as seen in Figure 2a, we noticed that depending on the contact hold time, the CCD of the cells showed inconsistent values, such as 0.88 mA/cm^2 when pressure was applied for 1 min, and 2.15 mA/cm^2 after a 30 min contact hold. Figure 2b shows the CCD trend as a function of the 25 MPa contact hold time. It was found that the CCD increased as

the hold time was increased up to 30 min, the CCD increased, but it decreased when it held longer than 30 min. The CCD range in our experiment (0.3 – 2.15 mA/cm^2) agrees with the wide range of CCDs reported in the literature 39, 40]. The CCD increase over the first 30 mins can be attributed to improved contact between the Li metal and SSE, leading to a lower effective current density due to the higher area of contact and more uniform current flow distribution. From the onset at 25 MPa, the pressure dropped to 23 MPa within 30 min (Figure 2.4b), indicating that any voids at the interface between Li metal and the SSE were filled with deformed Li metal. Impedance measurements were also conducted during this period, showing an initial rapid drop in impedance during the first 20 min and slowly decaying afterward (Figure 2.5).

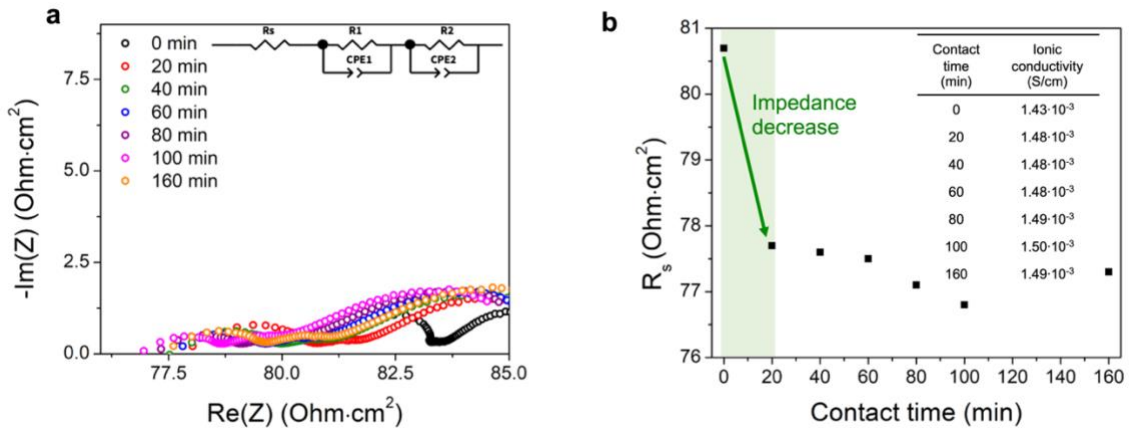

Figure 2.5 a) Nyquist plot of electrochemical impedance spectroscopy (EIS) measurement during 25 MPa contact hold step. b) Resistance (R_s) obtained from EIS measurements as a function of 25 MPa contact hold time.

After the 1-min holding cell was shorted at 0.88 mA/cm^2, the X-ray computed tomography (CT) was used to observe the Li/SSE interface and 3-dimensional morphology of the solid-state cell (Figure 2.6, Figure 2.7c). Disparities in image contrast were used to assign the white regions and gray areas in the 3D reconstructed image to Li metal and SSE, respectively. Evidence of Li dendrite growth was observed within the SSE layer originating from the Li metal. The voltage

response after cell shorting was caused by the Li dendrite growth and its penetration through the SSE layer. When the contact time is longer than 30 min, CCDs are reduced again as shown in the red region in Figure 2.7b. This could be attributed to the excessive creep behavior of Li metal inside the SSE pellet which results in the more favorable short-circuit at a lower CCD [54].

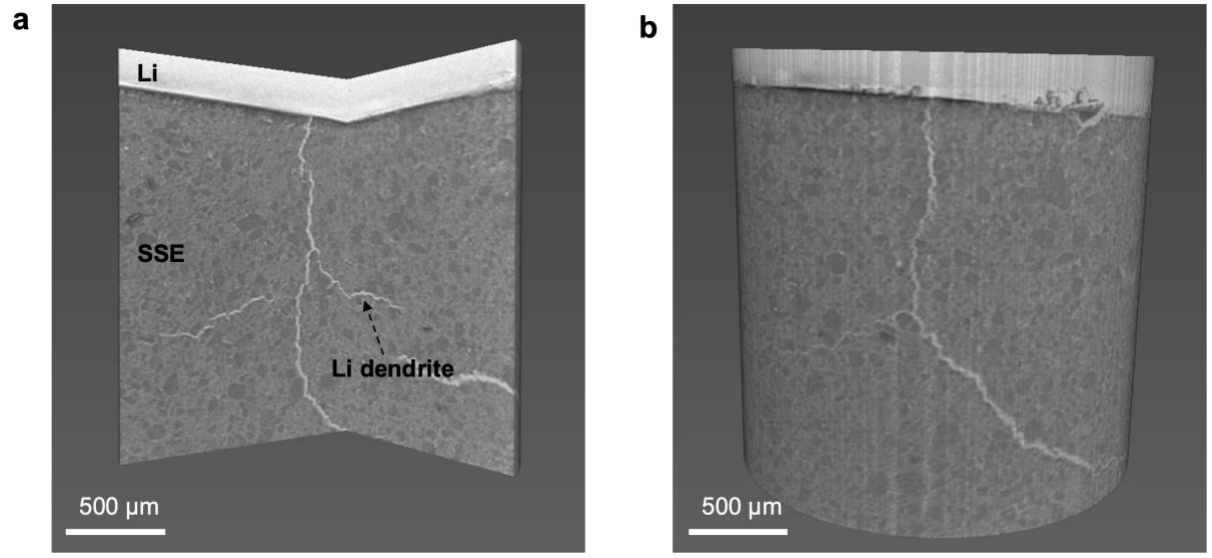

Figure 2.6 a) X-ray computed tomography (CT) of one end of the Li metal symmetric cell after shorting. b) X-ray CT reconstruction before the box cutting of the cell.

By increasing the holding time, the effective contact area between Li metal and the SSE will increase due to the deformation of Li metal at the interface which can improve the uniformity for local current distribution and thus CCD. The correlation between Li deformation and the measured CCD was investigated with the microscopic observation of a cross-sectional image by using a cryogenic focused ion beam (cryo-FIB) after pressing the Li metal anode on the SSE pellet. Since ion beam milling at room temperature can damage Li metal which results in both an altered morphology and chemistry [103], cryo-FIB was used to obtain intact Li metal interface images. Figure 2.7d shows the cross-sectional scanning electron microscope (SEM) images for 25 MPa pressured Li/SSE interface after contact-holding a 1 min and a 30 min. These cells were not cycled

to investigate interfacial contact as a function of contact hold time. For the 30-min holding sample, the interface between the Li and SSE has no pores and the Li is fully in contact with the SSE, while the 1-min holding sample shows numerous voids at the interface, indicating poor Li contact with the SSE. The result of having better contact for longer contact hold time is expected based on previous studies investigating Li metal deformation near room temperature. The mechanical deformation test showed Li metal can substantially fill the voids, even at pressures less than 5 MPa measured by Ding *et al* [104]. Moreover, Zhang *et al.* demonstrated that Li-SSE contact area increased over time under 1.5 – 7.5 MPa of stack pressure [105]. This study implied that the contact area of Li and SSE could increase over time through mechanical deformation of Li. The fraction in contact increased with time, showing the Li deformation-induced contact increase was rapid for the first 30 min and slowly decayed after that, which corresponds well with our pressure reduction due to Li deformation in Figure 2b, d. Thus, considering the soft mechanical properties of Li and its time-dependent deformation, the Li metal contact time under applied pressure is a vital parameter to report.

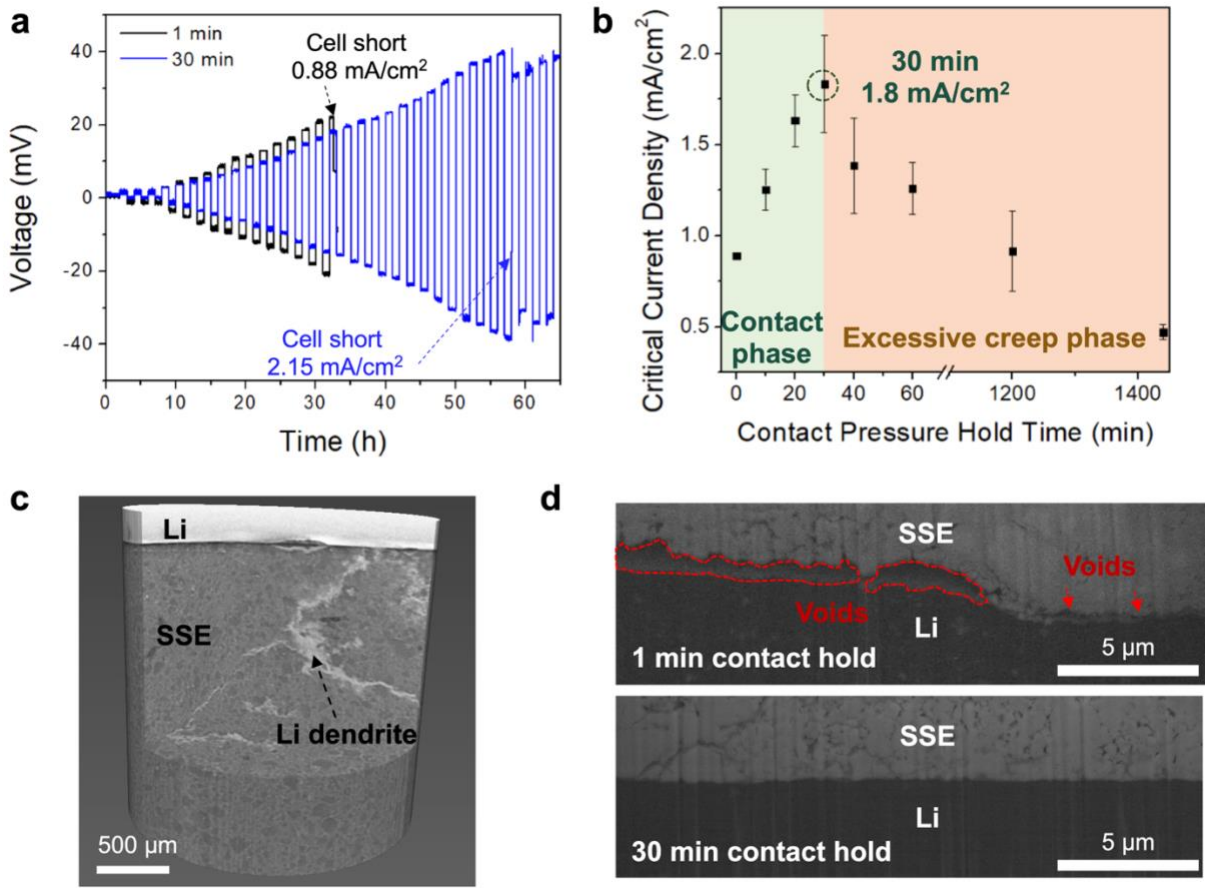

Figure 2.7 a) Critical current density (CCD) ramping test of Li symmetric cells, where a contact pressure of 25 MPa was applied for 1 min (black) and 30 min (blue). b) The CCD trend as a function of the contact hold time at 25 MPa. c) X-ray computed tomography of one end of the Li metal symmetric cell after shorting. d) Cross-sectional SEM images of Li/SSE interface contacted at 25 MPa for 1 min and 30 min. The electron imaging and FIB milling were conducted in cryogenic conditions to minimize damage to the Li metal.

2.3.2 The critical current density of Li metal full cells

As previously mentioned, reports using Li metal full cells appear to display a lower CCD compared to Li metal symmetric cells. Most literature reports attribute low CCDs to the intrinsic interfacial instability between Li metal and various SSEs, or high impedance growth at the Li metal – SSE interface [69]. However, these explanations do not agree with the symmetric vs full cell trends observed. As the same Li metal – SSE interface is utilized in both the symmetric and full cells, it

indicates that the contrasting CCDs reported in both cell configurations are not correlated with the Li metal – SSE's interfacial properties, but rather a cell level phenomenon induced by the fact that a cathode is used in the full cell and not in a symmetric cell. Given the understanding that Li metal undergoes a significant volume change during plating and stripping (1 $mAh/cm^2 \approx 5$ μm) [106], overall cell volume change in full cells is expected to be substantial compared to symmetric cells where negligible net volume change is expected, regardless of areal capacity exchanged. Thus, unlike in symmetric cells, it is necessary to consider both cathode and anode expansion/shrinkage in full cells, because volume changes during cycling can induce significant changes in cell stack pressure, and in turn, affect its CCD.

As a thought experiment, the volume change scenario for a symmetric cell and a full cell model is illustrated in Figure 2.8a**.** The pressure does not change during symmetric cell cycling theoretically, because stripped Li from one side would be plated on the counter electrode. However, in a full cell, Li metal will grow in thickness while the cathode shrinkage is significantly smaller when the cell is charged, leading to an overall volume expansion of the whole cell (Table 2.1). During discharge, almost all the Li will be sent back to the cathode, and the volume will once again shrink. Therefore, pressure increase/decrease apparent during charge and discharge is mainly due to the volume change of the Li metal anode. As the volume change largely comes from Li metal plating, a higher degree of pressure change is expected when the cell capacity is increased, resulting in conditions deviating further away from that of a symmetric cell.

Table 2.1 Expected electrode layer thickness calculation for 4 mAh/cm^2 NCM811 | LPSCl | Li cell. The cathode volume thickness calculation was based on SEM measurement. The anode thickness change calculation was estimated based on treating 1 mAh/cm^2 as 5 μm Li metal thickness change [106].

	$\Delta Thick_{Cathode}$	$\Delta Thick_{Anode}$	$\Delta Thick_{net}$ ($\Delta Thick_{Cathode}+\Delta Thick_{Anode}$)
Pristine (μm)	-	-	0
Charge (μm)	-1	+20	+19
Discharge (μm)	+1	-20	0

To probe the CCDs of full cells, NCM811 | LPSCl | Li cells with different cathode loadings were cycled using the stepwise current ramping protocol (Figure 2.8b). Please note that the optimum fabrication protocol of Li metal anode which is the 30-min contact at 25 MPa followed by release to 5 MPa was used for an anode preparation. With higher cathode loadings, pressure changes during charge/discharge were more severe because the amount of plated Li on the anode during charging is larger. Therefore, the stack pressure change during cycling has a linear correlation with the cathode loading (Figure 2.8c). In particular, with a cathode loading of 6.4 mg/cm^2, the absolute pressure change is 0.73 MPa whereas the absolute pressure change reaches 2.14 MPa for loading of 25.5 mg/cm^2 and 6.2 MPa for loading of 51.0 mg/cm^2. The CCDs obtained from full cells were in the range of 0.3 – 1.0 mA/cm^2, showing a decreasing trend with higher cathode loading. The low CCD for higher loading cells could be attributed to higher cell pressure from thicker Li plating. There are three major Li^+ migrations and Li fluxes involved during plating/stripping of lithium: i) Li^+ migration from applied current during cycling ($J_{Li^+ migration}$), ii) Self-diffusion of Li atoms from concentration gradient ($J_{Li\ diffusion}$), 3. Li creep deformation from the stack pressure ($J_{Li\ creep}$) [96]. If these three fluxes maintain the balance, ($J_{Li^+ migration} = J_{Li\ diffusion} + J_{Li\ creep}$), the dendritic growth of Li could be inhibited [107]. For the Figure 2.8d

case, cells with the same initial stack pressure but with various cathode loadings, the $J_{Li^+\ migration}$ would be similar for all cells at the same current densities. However, the higher cathode loading cells would eventually operate at higher pressure due to the thicker Li plating on the anode side. This higher operating pressure would yield a larger flux of Li ($J_{Li\ creep}$) to the interface, which results in the imbalance of the fluxes and shorts the cells.

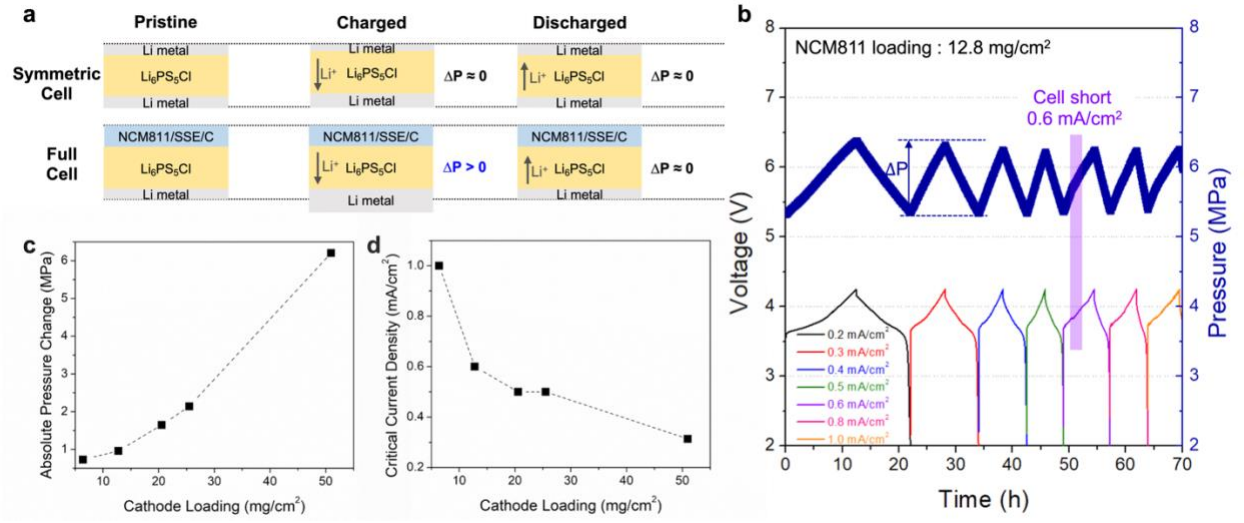

Figure 2.8 a) Schematic of the pressure change during cycling in a Li metal symmetric cell and a full cell. b) The *operando* pressure monitoring and voltage curve during cycling of Li metal full cells. All cells were cycled with the stepwise constant current; 0.2 to 1.0 mA/cm^2. c) Absolute pressure changes during cycling and d) Critical current densities of Li metal full cells as a function of cathode loading. The absolute pressure change was calculated by subtracting the first cycle minimum pressure from the first cycle maximum pressure. All of the cyclings were performed at an initial stack pressure of 5 MPa and 40°C.

2.3.3 The operating pressure control of Li metal full cells

Given that the cathode loading presents a direct impact on the degree of pressure change and the resulting CCD, operating the cells at a constant pressure could create conditions more similar to symmetric cells and allow for higher CCDs in full cells. Therefore, the cell setup was modified to incorporate springs that can compensate for the volume expansion and shrinkage of

the cell. This constant pressure setup, therefore, allows us to cycle the full cell at nearly constant pressure. The springs were selected based on their maximum load (which should be higher than the load applied during cycling) and their spring constants, to ensure that we can reach the target pressure with a reasonable compression of the springs.

The CCDs for Li-ASSB cells using setups with no springs (the fixed gap, Figure 2.9a) and with springs (the constant pressure, Figure 2.9b) in the cell holder were examined using similar ramping tests. In the fixed-gap cell, severe pressure change was observed during the charge and discharge process, around 140% pressure increase (6.96 MPa after 1st cycle charge) at the end of charge, exhibiting shorted behavior during the charging at a current density of 0.5 mA/cm^2 (Figure 2.9c, e). However, in the cell with springs, the pressure deviation was only 104% (5.21 MPa after 1st cycle charge) which is much less severe than fixed-gap cell and more stable during charging and discharging as expected, allowing the cell to cycle at a much higher current density until shorting at 1.0 mA/cm^2 (Figure 2.9d, f). The creep deformation rate of Li metal increases as the external compressive pressure gets higher [104]. The Li creep rate at 30°C was 0.06 μm/h at 2.2 MPa and 0.42 μm/h at 3.5 MPa. From this data, we could see only 1.2 MPa difference in stack pressure would result in 7 times higher creep rate of lithium. Therefore, by changing fixed gap setup to constant pressure setup, the Li would not have such high Li creep rate within the full cell. The fixed gap and constant pressure setup were examined also for the long time period (Figure 2.10). With the same loading and the cycling protocol of 0.5 mA/cm^2 long cycling after the formation cycles, the fixed gap setup cell shorted at 2nd cycle, whereas the constant pressure cell operated more than 50 cycles without shorting. As such, the CCD of the Li metal full cell can be improved by enabling the constant pressure cycling, which gives us the methodologic clue to solve the volume change deriven pressure accumulation in the practical Li metal full cell.

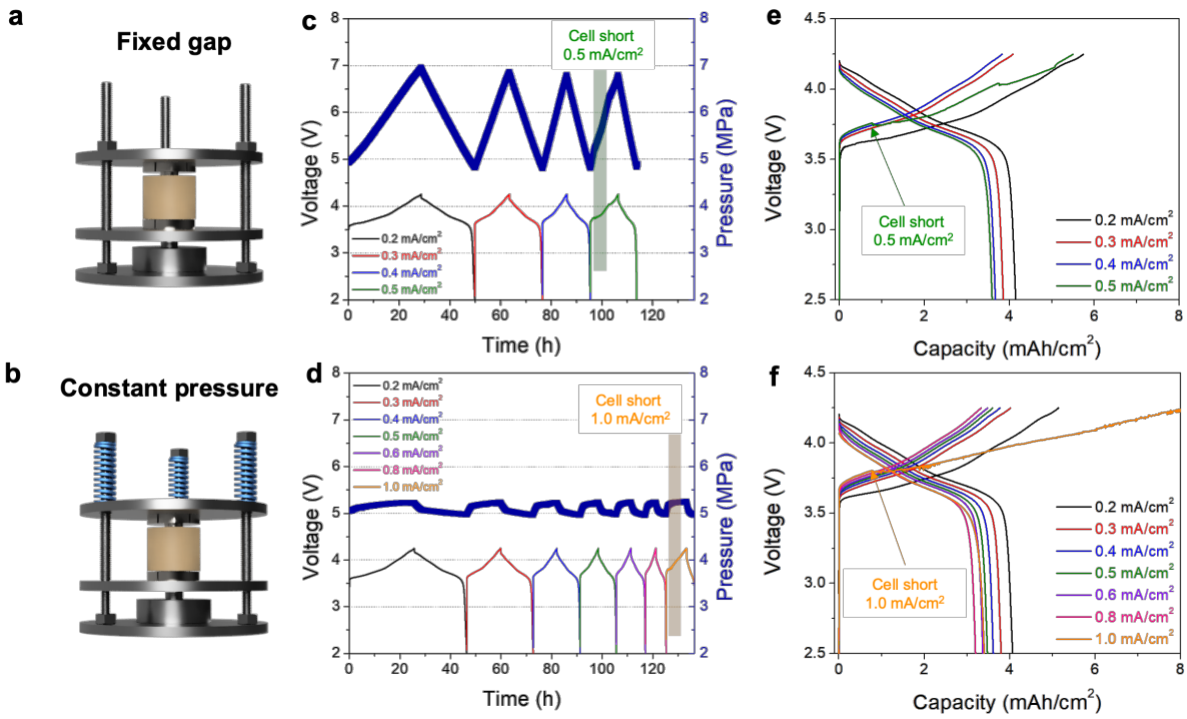

Figure 2.9 The schematic of the cell cycling setups for a) fixed gap and b) constant pressure. The NCM811 loading of both cells were 25.5 mg/cm^2. The *operando* pressure monitoring and corresponding voltage profiles of NCM811 | LPSCl | Li metal cells with c, e) fixed gap and d, f) constant pressure setup at ramping current densities. All the cycling was performed at an initial stack pressure of 5 MPa at 40°C.

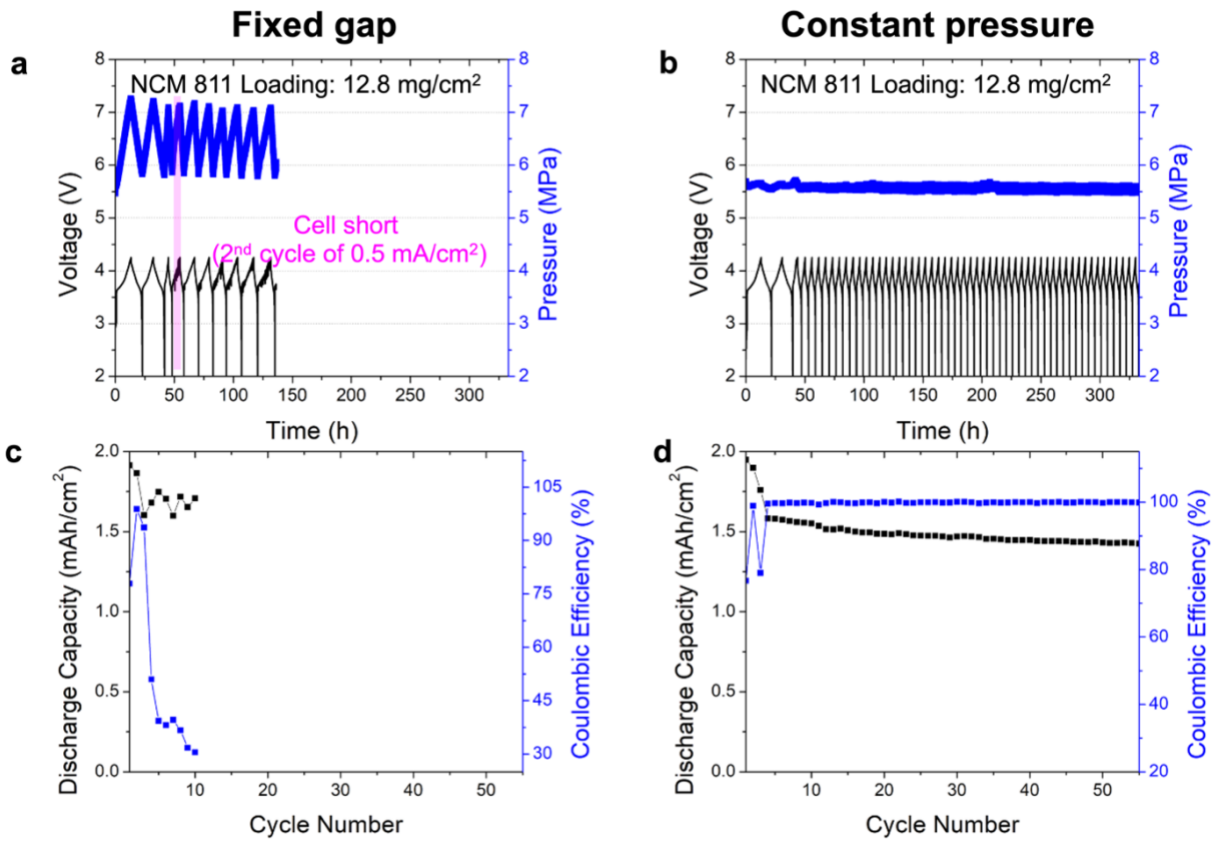

Figure 2.10 a, c) Fixed gap and b, d) constant pressure cycling of NCM811 | LPSCl | Li full cells. Cycling program for both cells were the same: Activation cycles for 2 cycles at 0.2 mA/cm^2 and long cycling at 0.5 mA/cm^2. For fix gap setup, the cell shorted during the second cycle of 0.5 mA/cm^2 whereas constant pressure cell cycled more than 50 cycles.

To probe the effects of constant pressure at lower pressures, fixed gap and constant pressure cells were tested at 1 MPa, 3 MPa and 5 MPa (Figure 2.11). At 1 MPa, both constant gap and constant pressure cells showed the same low CCD of 0.3 mA/cm^2, whereas constant pressure cell exhibited slightly higher CCD of 0.6 mA/cm^2 than constant gap cell of 0.4 mA/cm^2 at 3 MPa. Constant pressure effect dominates more from 5 MPa, where the CCD difference of constant pressure and fixed gap is 0.6 mA/cm^2. This trend is not surprising based on the Li creep behavior observed in Figure 2.4 and Figure 2. At 1 MPa, the stack pressure applied is insufficient to provide a creep deformation rate high enough to ensure good interfacial contact between the Li metal and

the SSE. This results in non-uniform Li plating and results in early cell failure regardless of the effects of constant pressure. While a higher creep deformation rate at 3 MPa allows the effects of constant pressure applied to be detected, previous reports have also found void accumulation at the interface at 3 MPa [96], indicating that 3 MPa is still insufficient to maintain good contact. At 5 MPa, sufficient Li creep was achieved and thus able to effectively double the CCD detected when constant pressure is applied. This pressure value agrees with the literature reported values for ideal Li ASSB full cells [65]. While higher stack pressures may produce greater effects on CCD, stack pressures of 10 MPa or greater have been found to induce excessive Li creep into and through the SSE separator, also inducing cell failure [54]. The results in this work, along with findings in the literature suggests that Li ASSBs are best operated within a narrow range of stack pressures, highlighting the need for constant pressure operation to maximize CCD in Li ASSBs.

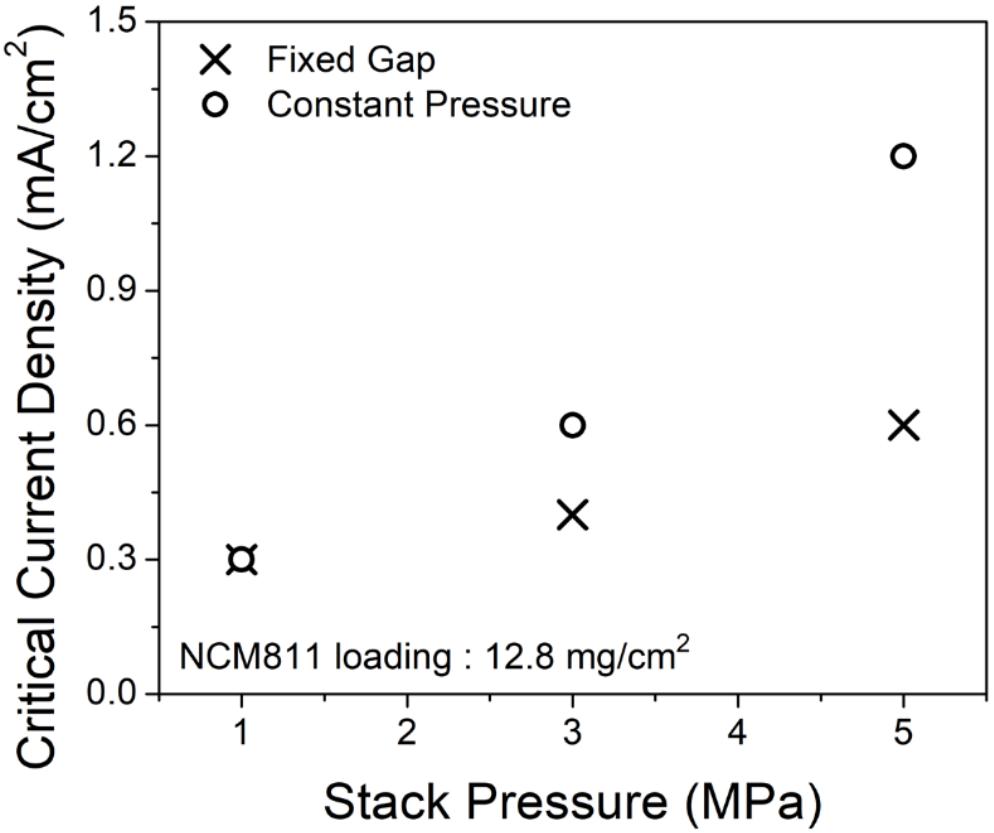

Figure 2.11 The CCD trends of fixed gap (cross symbol) and constant pressure (circle symbol) cells with the initial stack pressure of 1, 3, and 5 MPa. The NCM811 loading of all cells were 12.8 mg/cm^2.

2.4 Conclusions

The previously reported CCDs of Li-ASSBs exhibited extensive variations, with evident disparities between Li metal symmetric cells and Li metal full cells. In this study, we investigated critical fabrication parameters that can resolve the discrepancies the in reported CCDs. In particular, the contact hold time during cell assembly is a crucial consideration, which affects the formation of solid physical contact between Li metal and SSE. During this hold time, Li metal undergoes time dependent mechanical deformation that can alter the effective contact area. By improving the interfacial contact and uniformity, the CCD can thus be improved and achieved

more reproducibly. In addition, we have confirmed the mismatch in terms of CCDs and corresponding performance between symmetric and full cell, where contributions from the cathode must be considered. The volume change in Li metal full cells is inevitable due to expansion and contraction of electrodes from Li metal plating and stripping at anode during cell cycling which cannot compensate from the cathode side. The continuous volume change driven stress accumulation within the confined cell was examined via the *operando* pressure monitoring during cell cycling. The increased stack pressure resulted in the premature shorting of the full cell and the trend was correlated to the cathode loading, which showed that cells with higher cathode loading exhibited much more severe pressure change, subsequently shorting at lower current densities. We have identified anode volume change, which accumulates to net stack pressure change, as an important cause of cell shorting and have designed a constant pressure cell architecture which utilizes springs to mitigate pressure changes during cycling. This improved setup demonstrates the necessity of maintaining constant stack pressure during cycling and has enabled higher current density operation for Li-ASSBs, specifically near room temperature.

Acknowledgements

Chapter 2, in full, is a reprint of the material as it appears in "S.-Y. Ham, H. Yang, O. Nunez-cuacuas, D.H.S. Tan, Y.-T. Chen, G. Deysher, A. Cronk, P. Ridley, J.-M. Doux, E.A. Wu, J. Jang, Y.S. Meng, Assessing the critical current density of all-solid-state Li metal symmetric and full cells, Energy Storage Materials 55 (2023) 455–462." The dissertation author was the first author of this paper, all authors contributed to this work.

Chapter 3 Overcoming Low Initial Coulombic Efficiencies of Si anodes through Prelithiation in All-solid-state Batteries

3.1 Introduction

All-solid-state batteries (ASSBs) have drawn considerable attention as safer and potentially more energy-dense devices as compared to conventional liquid cells. Achieving high energy density ASSBs depends on the development of high-capacity electrodes in a solid-state architecture.[108,109] On the anode side, potential candidate materials or architectures include Li metal,[28,54,81,101] anode-free,[110] and alloy-type anodes such as Li-Si,[111,112] Li-In,[113–116] Li-Sn,[117] Li-Al,[118,119] Li-Sb,[120] and Li-Mg.[121] However, high specific capacity and low propensity for Li dendrite growth and cell shorting make alloy-type anodes the most promising for next-generation ASSBs.

Si has been extensively studied in lithium-ion batteries (LIBs) for decades. Many reports have suggested that the use of pure Si as the anode is impractical due to its poor interfacial stability with liquid electrolytes and pulverization during cycling.[122,123] However, a recent study demonstrated the use of a 99.9 wt. % micro-silicon (μSi) anode in combination with an argyrodite solid electrolyte (Li_6PS_5Cl) to produce an ASSB with a high areal current density and high areal loadings.[91] The successful use of μSi as an anode was attributed to the passivation of the sulfide electrolyte-Si interface, limiting the growth of a poorly-conducting solid-electrolyte interphase (SEI).

Although Si-based all-solid-state cells with a passivating SEI and a high energy density have already been demonstrated, further performance improvements can be achieved, including increases in the initial Coulombic efficiency (ICE), electronic conductivity, and Li^+ diffusivity

(**Figure 3.1**). Notably, the prelithiation of Si, which has traditionally been implemented in LIBs,[124] could be a good approach to enable such improvements.

One of the well-established prelithiation methods is electrochemical prelithiation.[125–128] In this approach, a Si electrode is lithiated by building an electrochemical cell comprising a Li metal counter electrode and a non-aqueous electrolyte. The redox potential difference of the two electrodes results in spontaneous lithiation of Si and SEI formation. However, the extent of "electrochemical" prelithiation must be well controlled, since insufficient lithiation cannot improve the ICE due to remaining Li trapping sites, while over-lithiation could start the lithium plating on the anode surface.[129] Due to the high chemical reactivity of Li, one of the challenges to implementing the successful prelithiation lies in finding stable prelithiation reagents (Li source). As such, Cao et al. introduced a polymer to protect the Li source, where the metallic Li source for prelithiation was shielded by the polymer before being made into the full cell.[130] More commercially viable option for prelithiation reagent is the stabilized lithium metal powder (SLMP). Ai et al. developed a solution process to coat SLMP on anode material, where both graphite/NMC and SiO/NMC full cells exhibited 31% higher ICE after the prelithiation of the anodes.[131] Forney et al. deposited SLMP on a Si – carbon nanotube (CNT) anode and used a mechanical press to apply a pressure of 100-300 PSI to the stack for 30-60 s to crack the electronically insulating Li_2CO_3 coating of SLMP and facilitate the prelithiation process.[132] Another study showed that mere contact between passivated Li metal powder (PLMP) and a Si/graphite electrode could induce prelithiation.[133]

The first Si-based all-solid-state battery with prelithiation of the Si anode was recently reported,[134] where prelithiation of Si was completed by ball-milling with Li metal in anhydrous hexane. Starting from the prelithiated Si, further mechanochemical milling was needed to mix the

Li_xSi active material, the solid electrolyte, and the carbon additive to form the composite anode. The Li_xSi composite electrode was paired with a sulfur cathode and the full cell demonstrated a stable capacity for over 500 cycles. While such performance is impressive, this work required an extra high-energy ball-milling step in organic solvent to prelithiate the Si, adding complexity to the ASSB fabrication process. Prelithiation method using SLMP without electrolyte has been reported in the past as well. Jang et al. successfully implemented the prelithiation of Si without carbon paired with fluorinated polymer to mitigate SEI in liquid electrolyte.[135] Lee et al. enabled the SLMP-induced prelithiation of graphite-silicon without electrolyte in all-solid-state batteries.[136]

Here, we introduce a simple pressure-induced prelithiation strategy for Si anodes during ASSB fabrication and the prelithiated Si anode was characterized using solid-state nuclear magnetic resonance (ssNMR). The performance of our prelithiated Si anode was evaluated in symmetric-, half-, and full-cells. In this work, the effectiveness of the prelithiation in ASSB was assessed depending on cathode selection and N/P ratio for the first time. Regarding long term cyclability, a cell of prelithiated Si paired with LCO showed a high ICE of over 95% with a stable cyclability for 1000 cycles at 5 mA cm^{-2} current density.

Interestingly, we revealed that cathode irreversibility determined the effect of prelithiation on the full-cell and high N/P ratio Si cells behaved completely different from the liquid counterparts with the presence of excess Si. For solid-state cells, instead of having a low state of charge within the anode, Si becomes partially lithiated at its 2D interface and consistently acts like a cell with N/P ratio of 1. This behavior can be translated within a full cell, where the ICE was constant regardless of the N/P ratio. Moreover, the improved ICE was achieved even with a high loading of 10 mAh cm^{-2} from the prelithiated Si, showing the true viability of the Si anode with a

high-loading cathode. Based on the novel understanding, our work provides the insight to properly adopt prelithiated Si in ASSB configuration.

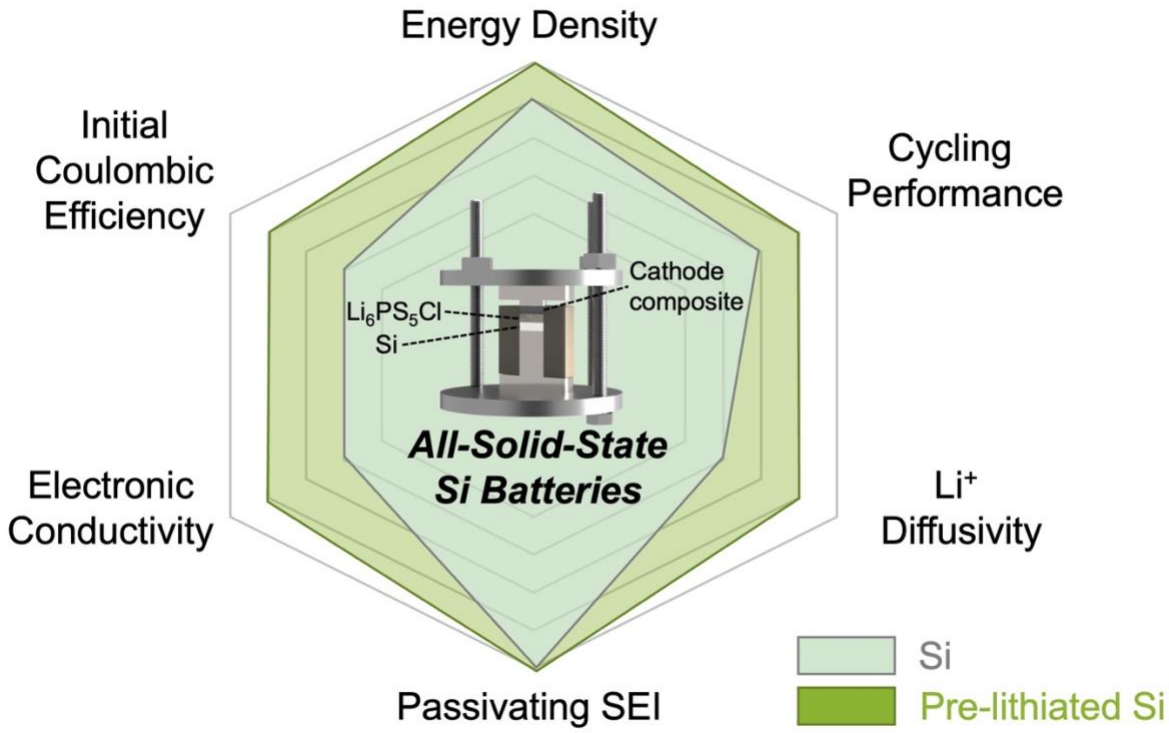

Figure 3.1 Comparison of Si and prelithiated Si for all-solid-state batteries. A radar comparison chart of Si (light blue shade) and prelithiated Si (green shade) anodes for various electrochemical properties and battery performance metrics.

3.2 Methods

3.2.1 Materials Preparation

Li_6PS_5Cl (LPSCl, NEI Corporation, USA) was used for the solid-state electrolyte (SSE) separator layer and cathode composite preparation. For cathode composite purposes, the LPSCl particle size was reduced using an EMAX ball mill (Retsch, Germany). The ball milling was

conducted for 2 hours at 300 rpm, using anhydrous xylene as a medium. Lithium cobalt oxide (LCO, MSE Supplies, USA), coated with a niobium-based layer, was used as received. The cathode composite was prepared by hand-mixing using a weight ratio of LCO : LPSCl = 70 : 30. For the preparation of lithiated μSi, μSi (Sigma Aldrich, USA) and stabilized Li metal powder (FMC, USA) was vortex mixed for 3 min. The mixture was subsequently pressed using a hydraulic press at 100 MPa for 30 s.

3.2.2 Materials Characterization

For the ^{7}Li solid-state NMR (ssNMR) measurements, all one-dimensional spectra were acquired at 18.8 T (800 MHz for ^{1}H) on a Bruker Ultrashield Plus standard bore magnet equipped with an Avance III console. The measurements were carried out using a 3.2 mm HXY MAS probe, and 3.2 mm single cap zirconia rotors packed and closed with a Vespel cap under Ar with a PTFE spacer between the sample and cap to further protect the sample from air exposure. A flow of N_2 gas at 2000 L h^{-1} was used to protect the sample from moisture contamination. Data were obtained using a static spin-echo pulse sequence (30°-TR-60°-TR-ACQ) with a 10 μs echo delay (TR). Rotors were kept static throughout each measurement to avoid sample evolution caused by frictional heating during magic angle spinning (MAS). 30° and 60° flip angles of 1.617 μs and 3.234 μs at 200 W, respectively, were used, and recycle delays of 10-90 s between scans were applied according to the longitudinal (T_1) relaxation properties of the sample. ^{7}Li chemical shifts were referenced to a 1 mol/L LiCl liquid solution at 0 ppm. Pulse lengths were calibrated on a liquid solution consisting of 80% volume saturated LiCl and 20% volume 1 mol/L $CuSO_4$. All spectra were processed with Topspin 3.6 and fitted with an in-house python code. T_2* measurements on each sample were also conducted to compensate for uneven signal decay of the

Li metal and diamagnetic components during the 10 μs echo delay. On each sample, a series of static spin-echos (30°-TR-60°-TR-ACQ) with variable echo delays was acquired and the spectra were integrated from 240-280 ppm and –200-200 ppm to account for Li metal and the overlapping diamagnetic signals, respectively.

FEI Scios Dualbeam (ThermoFisher Scientific) was used for cross-sectional images. The sample transfer was performed using an air-tight transfer arm from the Ar-filled glovebox to the FEI Scios Dualbeam chamber for no air exposure during the transfer process. After the sample mount, liquid nitrogen and the heat exchanger were set to perform cryogenic ion beam milling and electron beam imaging to minimize Li damage. The ion-beam milling to prepare the cross-section of samples was performed using a Ga^+ source. The sample was milled at 30 kV and 65 nA and cleaned at 30 nA and 15 nA afterward. All the electron beam imaging was done using 5 kV and 0.1 nA settings.

3.2.3 Electrochemical Characterization

Two titanium rods were used as current collectors at each end of the Li metal. The solid-state separator layer was fabricated by first putting 75 mg of LPSCl in a 10 mm inner diameter polyether ether ketone holder, which was then compressed between two titanium rods at 370 MPa. LCO cathode composite of 30 mg (active loading of 26.7 mg/cm^2) was placed on top of the LPSCl separator pellet and pressed at 370 MPa using a hydraulic press. 5 mg of Si was put for all Si and lithiated Si cells in this work. Si and Li_xSi were inserted onto the other side of the LPSCl separator pellet and pressed at 100 MPa. The cells were set to 75 MPa before cycling started. The full cell configuration follows the same protocol except one Li side is replaced with a cathode composite. All cell cycling was performed at room temperature using in the Argon-filled atmosphere

glovebox. The battery cells were cycled using a Neware Battery cycler and analyzed with BTS900 software. EIS measurements were conducted using Biologic SP-200. The frequency range was from 10 MHz to 0.1 Hz, with an applied AC potential of 10 mV. Direct current polarization was conducted to measure the electronic conductivity of Li_xSi by applying the voltage of 100 mV for 3 min.

3.3 Results and Discussion

3.3.1 Pressure-induced Prelithiation of Si

3.3.1.1 Morphology of Pressure-induced Prelithiation of Si

Prelithiation of Si was conducted via a simple mixing process coupled with a pressurizing step. In this work, an anode composed of vortex-mixed μSi and SLMP was introduced for the first time in an ASSB. Different amounts of SLMP were mixed with μSi powder to produce Li_xSi alloys with a molar ratio x = 0.25, 1, and 2 (e.g., $Li_{0.25}Si$, Li_1Si and Li_2Si). We note that those x values assume that the SLMP in μSi powders have fully reacted. The morphology of μSi and SLMP was investigated with scanning electron microscopy (SEM), indicating a particle size distribution of 2 – 5 μm for μSi and 10 – 60 μm for spherical SLMP (**Figure 3.2a, b**). From **Figure 3.3a**, we find that Si and Li domains in the final Li_1Si powder retain the morphology of the precursor particles. The absence of energy dispersive X-ray spectroscopy (EDS) signal from spherical regions within the Li_1Si powder sample allow their assignment to pure lithium metal due to the low energy of the Li X-ray transition (**Figure 3.3a**). In **Figure 3.3b**, a cross-sectional focused ion beam scanning electron microscopy (FIB-SEM) image was obtained on a 200 MPa pressed Li_1Si pellet. The pressed Li_1Si sample exhibits two types of domains: 1) regions comprised of distinct μSi and Li sub-domains, and 2) regions where the μSi and Li precursors alloyed to form a

new chemical composition. In the first type of domain, Li sub-domains are sandwiched between μSi domains, resulting in a different morphology from the SLMP precursor powder. Again, no EDS signal could be detected from those Li-rich sub-domains. The second type of domain has an entirely different morphology from the pristine μSi and SLMP powders, that is more comparable to charged (lithiated) Si where the gap between individual Si particle disappears and large Si blocks are formed instead. Additionally, Si EDS signal can be detected from those regions. Those analysis indicate that after pressing at 200 MPa for 30 s, the Li_1Si anode exhibits unreacted Li and μSi, as well as a Li-Si alloy phase. During the pressure-induced lithiation, Si is lithiated by diffusion of Li which would follow the Fick's second law of diffusion at the contact point of Li and Si. However, the contact area of Li and Si particles is limited when the Li and Si mixture is pressed at low pressure (**Figure 3.4a**). In **Figure 3.4b-c**, the 400 MPa pressed Li_1Si showed less remaining Li metal compared to 200 MPa the pressed pellet.

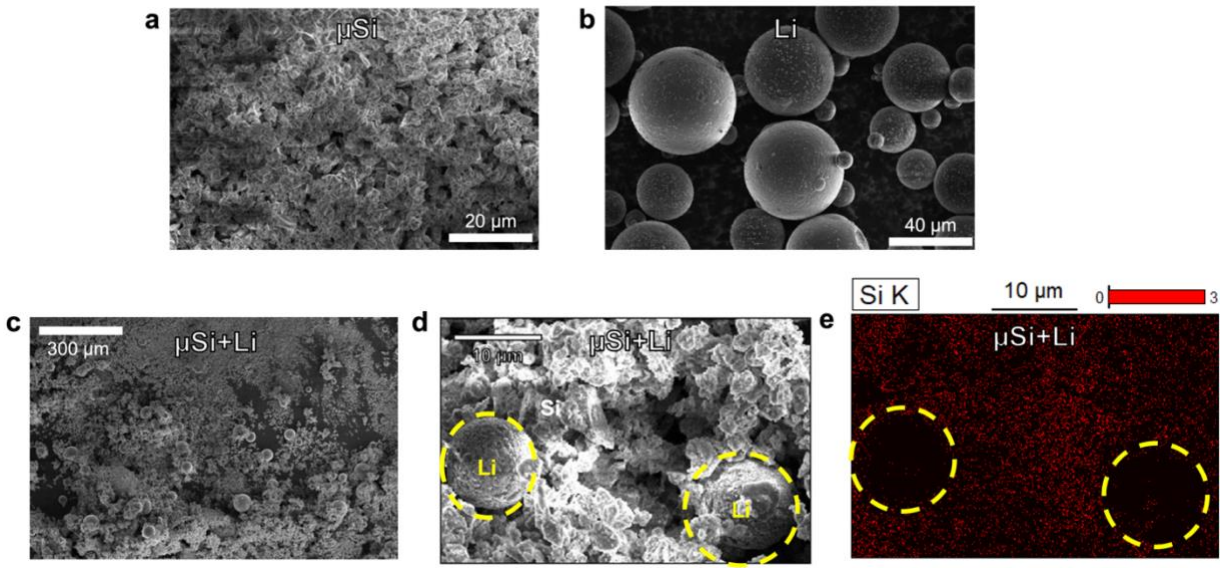

Figure 3.2 SEM images of (a) μSi, (b) SLMP (Li), (c) vortex mixed μSi and Li. (d) SEM image of vortex mixed μSi and Li and corresponding Si EDS from the same area.

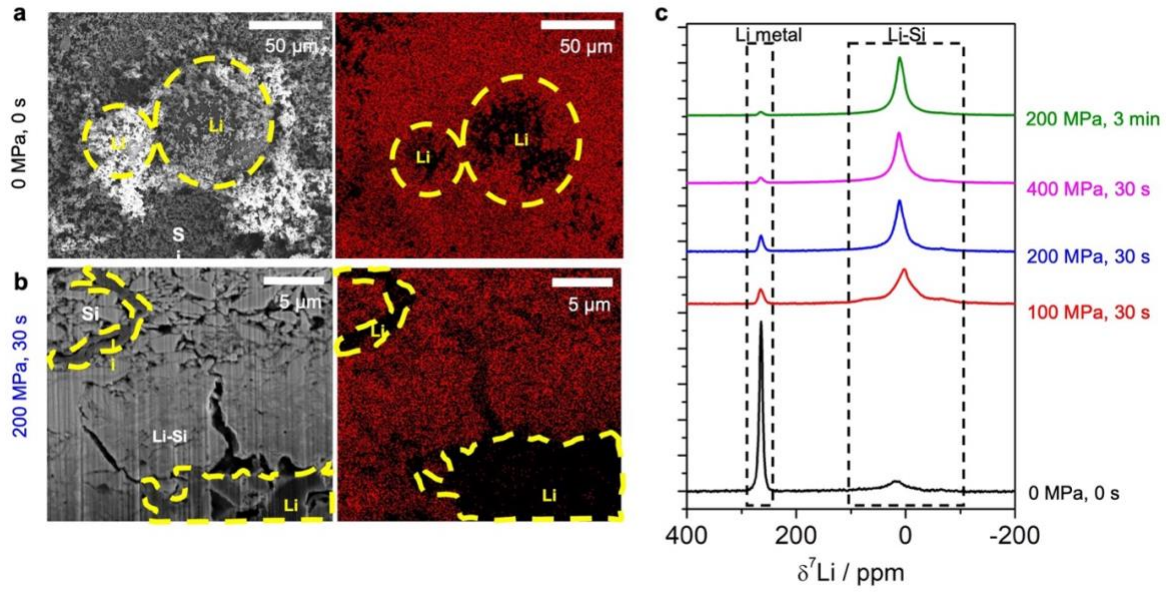

Figure 3.3 Morphology and NMR spectra of pressure-induced lithiation of Si. a) FIB/SEM cross-sectional image of non-pressed (0 MPa, 0 s) and b) pressed (200 MPa, 30 s) Li_1Si pellet before cycling. c) ^7Li NMR spectra of Li_1Si with different pressure and time.

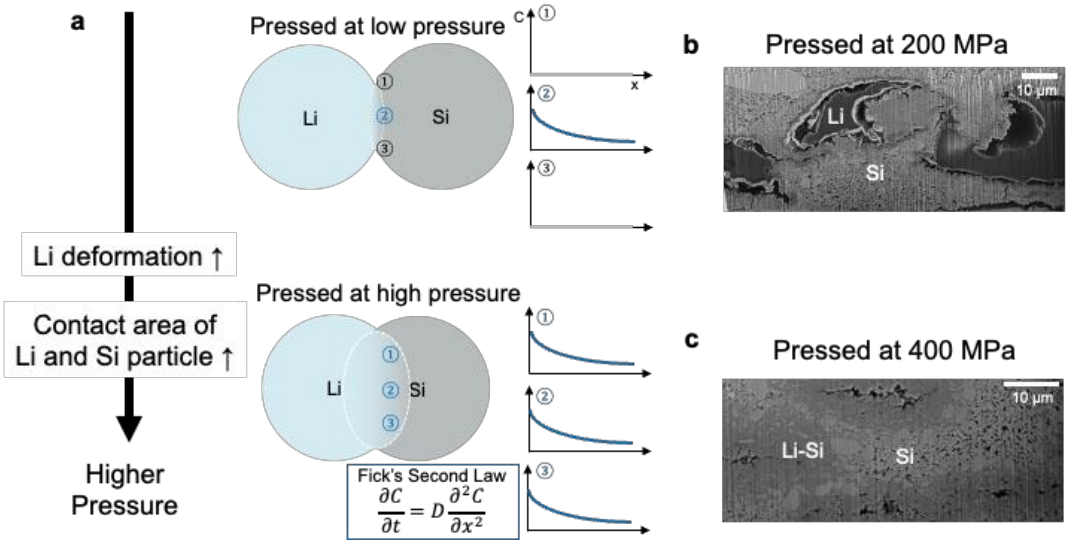

Figure 3.4 (a) Schematic of pressure-induced lithiation at low pressure (top) and high pressure (bottom). The hypothetical concentration of Li with respect to distance from the Li and Si contact point is shown on the right side. (b) Cross-sectional FIB/SEM image of Li_1Si at 200 MPa (c) Cross-sectional FIB/SEM image of Li_1Si at 400 MPa.

3.3.1.2 NMR of Pressure-induced Prelithiation of Si

To better understand the extent of alloy formation from pressurizing SLMP and μSi precursors, ^{7}Li ssNMR was used to probe the chemical state of bulk lithiated Si. ssNMR is crucial here, as lithiated Si is amorphous and cannot be studied using standard diffraction methods. ^{7}Li ssNMR, on the other hand, is sensitive to crystalline and amorphous phases alike and allows to distinguish and, in theory, quantify Li metal (265 ppm)[137] from the Li-Si alloy (broad signal centered around 0 ppm)[133] as their respective signals are well resolved. However, the penetration of the radiofrequency (RF) pulses used to excite the nuclear spins in a ssNMR measurement into metallic samples is limited and inversely proportional to the square root of the electronic conductivity. This results in a so-called "skin depth" of around 7.4 μm for Li metal (with an electronic conductivity of 1.1×10^7 S/cm)[138] under the chosen experimental conditions,[139] which is lower than the radius of some pristine SLMP particles (5 – 30 μm) and thus leads to an underestimation of the amount of metallic Li in the sample. The Li-Si alloy phases that form in the samples under consideration are many orders of magnitude less conductive than Li metal, as will be discussed in the next section, and their minimum skin depth of ~570 μm (calculated based on Li_2Si electronic conductivity) ensures that such regions can be probed quantitatively with ^{7}Li ssNMR. We note, however, that the Li-Si alloy signal likely overlaps with minor diamagnetic impurity phases that inevitably form at the surface of metallic Li (even when air/moisture exposure was avoided by handling the samples in the glovebox at all times), including LiOH and Li_2CO_3 resonating at ~0 ppm.[140] In **Figure 3.3c**, ^{7}Li ssNMR was conducted on several SLMP + μSi samples subjected to pressures varying from 0 to 400 MPa for 30 s to 3 minutes to determine the conditions under which maximum Si prelithiation is achieved. Given that the size distribution of metallic Li sub-domains in the pressed samples is on par with the particle size distribution of the

SLMP precursor, the relative amount of Li metal detected by ^{7}Li ssNMR follows the same trend as the actual amount of metallic Li in the samples of interest to this work, despite skin depth issues. This allows us to use the relative integrated intensity of the Li metal and Li-Si alloy signals in the ^{7}Li ssNMR spectra to follow the incorporation of Li into Si as a function of sample processing conditions. The impact of ssNMR signal (T_2*) relaxation during data acquisition was accounted for in the quantification of the observable Li signals (see results in **Table 3.1)** for all samples except the unpressed Li_1Si for which a T_2* measurement could not be conducted due to sample evolution in the spectrometer. The unpressed Li_1Si sample contains the most Li metal and a smaller fraction of the Li-Si phase, with the 0 ppm resonance accounting for 27.8 % of the total ^{7}Li ssNMR signal intensity. Despite the lack of T_2* adjustment for this sample, these results are expected to hold as the changes in Li molar % from T_2* adjustment of Li metal or diamagnetic phases for other samples are smaller than 1%. Conversely, pressed Li_1Si samples exhibit > 92% of the total ^{7}Li signal intensity at 0 ppm, indicating the presence of a major Li-Si alloy phase. The relative intensity of the 0 ppm signal as compared to the Li metal signal increases with higher pressure and longer pressing time, indicating an increased fraction of Li-Si alloy in the sample. For example, applying 200 MPa of pressure for 3 min (green) leads to greater Li incorporation into the Si phase than applying the same amount of pressure for 30 s (blue), as evidenced by the 98.2 and 92.9% of the total ^{7}Li ssNMR signal intensity present at 0 ppm for these two samples, respectively. Those results indicate that a Li-Si alloy can be formed by pressurizing the SLMP and μSi precursor powders in the absence of electrolyte, demonstrating that the latter is not required to facilitate the alloying reaction unlike previously thought.[141] Interestingly, unpressed Li_xSi samples evolve over the course of the ssNMR measurements, while the composition of pressed samples remains stable. This is shown in **Figure 3.5**, where ^{7}Li ssNMR spectra collected on four different Li_xSi samples

(Li_1Si and Li_2Si non-pressurized and pressurized at 200 MPa for 30 s) before, during, and after a T_2* relaxation time measurement, are compared. For the unpressed samples, the 0 ppm signal increases over the course of the measurement, indicating that Li-Si alloying is taking place over time. On the other hand, the spectra of the pressed samples do not evolve because Si has already been lithiated at 200 MPa and is stable under ambient conditions. The homogeneity of NMR spectra with the fitting is provided in **Figure 3.6**.

Table 3.1 Relative ratio (in Li mol.%) of observed ^{7}Li ssNMR signal intensity corresponding to metallic Li and to a Li-Si alloy. ^{7}Li ssNMR spectra were acquired on vortex-mixed powders with nominal composition Li_1Si after application of pressures varying from 0 to 400 MPa for 30 s to 3 minutes. The relative ratios are given before and after adjusting for spin-spin (T_2*) relaxation of the ^{7}Li ssNMR signal during data acquisition. The T_2* relaxation time of Li metal was measured on a pure SLMP sample, fitted to a single stretched exponential decay function, and used to scale the metallic Li signal observed in the spectra obtained on all samples. The T_2* relaxation time for the diamagnetic components, including the Li-Si alloy phase, was measured on each sample due to expected changes in Li-Si alloy composition with pressure, and fitted to a stretched exponential. For the unpressed sample, the T_2* of the Li-Si signal could not be determined as it evolved during the T_2* measurement (see Figure 3.5).

Li_1Si Pressing Condition	Relative Li mol.% (not T2 adjusted)	Relative Li-Si mol.% (not T2 adjusted)	Li T2 (stretched exp) [s]	Li-Si T2 (stretched exp) [s]	Normalized Relative Li mol.% (T2 adjusted)	Normalized Relative Li-Si mol.% (T2 adjusted)
0 MPa, 0 s	**75.8**	**24.2**	0.000467	N/A	N/A	N/A
100 MPa, 30 s	7.7	92.3	0.000467	7.10E-05	**6.9**	**93.1**
200 MPa, 30 s	7.6	92.4	0.000467	1.08E-04	**7.1**	**92.9**
400 MPa, 30 s	3.4	96.6	0.000467	6.80E-05	**3.0**	**97.0**
200 MPa, 3 min	2.0	98.0	0.000467	6.90E-05	**1.8**	**98.2**

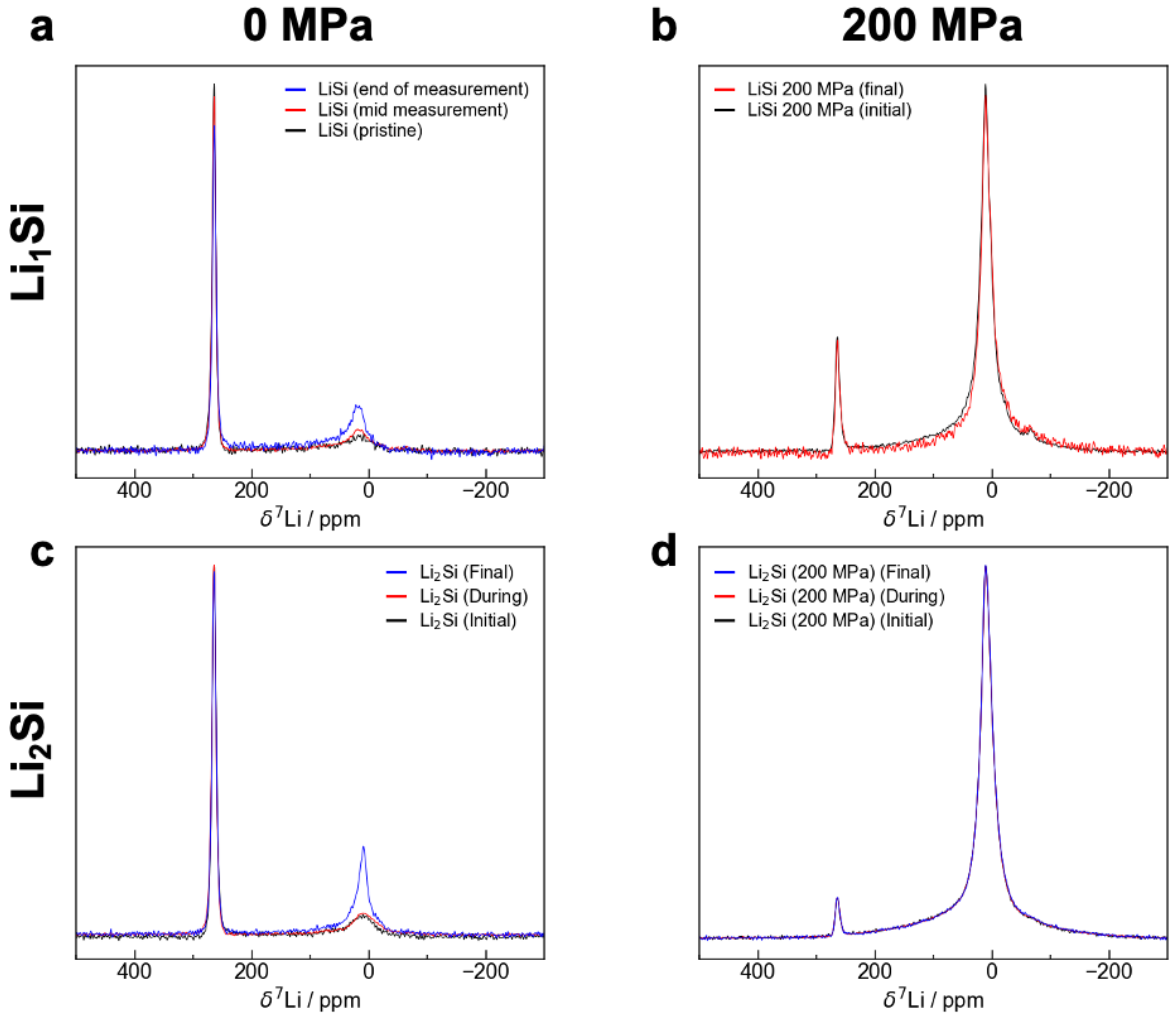

Figure 3.5 ^{7}Li ssNMR spectra of vortex-mixed (a, b) Li_1Si and (c, d) Li_2Si samples. The samples were either unpressed (a, c) or pressed at 200 MPa for 30 s. For each sample, ^{7}Li ssNMR spectra were obtained before, during, and after the spin-spin (T_2*) relaxation time measurement. For the two unpressurized samples (a, c), the Li-Si alloy signal grows during the T_2* measurement, precluding an accurate estimation of its T_2* relaxation time.

Regarding homogeneity of NMR spectra, we conducted additional fits on each of the spectra presented in **Figure 3.3c** of the manuscript. Fits are presented in **Figure 3.6** below. The Li-Si resonance for the unpressed sample is centered at 16.5 ppm, which corresponds well to the reported resonance for Li_7Si_{31}. The spectrum obtained on the sample pressed at 100 MPa for 30 s exhibits resonances at 69.4 ppm and 3 ppm, which are tentatively assigned to $Li_{21}Si_5$ and $Li_{15}Si_4$,

respectively.[1] Fits for the spectra obtained on the samples pressed at 200 MPa and 400 MPa for 30 s as well as 200 MPa for 3 min are nearly identical and are fit with a single sharp resonance centered between 10.2-11.5 ppm, and a much broader resonance centered between 15-30 ppm. The sharp resonance in these samples is tentatively assigned to $Li_{13}Si_4$, while the broad component is due to a combination of other Li_xSi_y phases present.[142] An additional, weak signal at –67 ppm is observed in each spectrum and could not be assigned to a known Li-Si phase.

Based on the above results, it appears that the least homogenous sample is the sample pressed at 100 MPa for 30 s as it likely contains both $Li_{21}Si_5$ and $Li_{15}Si_4$. While the unpressed sample spontaneously formed some Li_7Si_3, it is still mostly composed of unincorporated Li metal. Pressing the Li-Si mixtures at higher pressures and for longer durations forms a larger phase fraction of the Li-Si alloy and appears to yield a more consistent mixture of Li_xSi_y phases, mostly consisting of $Li_{13}Si_4$. While consistency across samples should not be conflated with a homogenous distribution of phases throughout individual samples (NMR does not provide any information on the spatial distribution of the phases), the larger pressure applied on these samples likely forces more intimate contact and reactions between the SLMP and Si alloy that drives the formation of mostly $Li_{13}Si_4$.

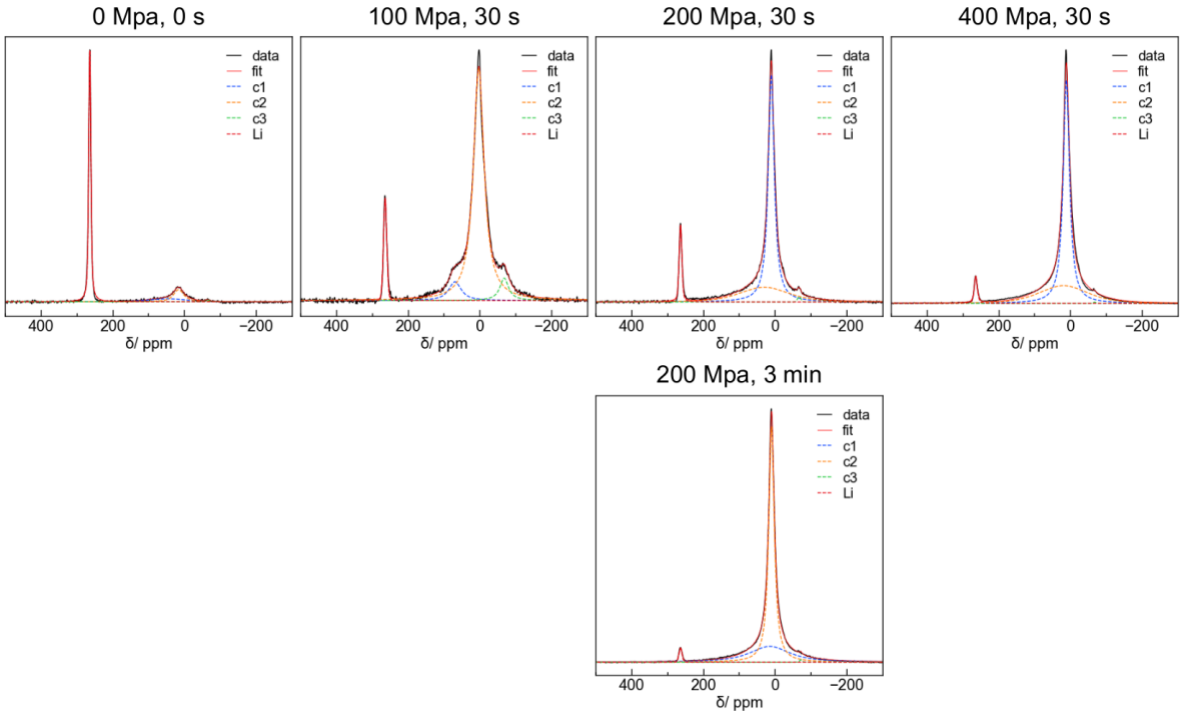

Figure 3.6 Fits conducted on ^{7}Li ssNMR spectra obtained on Li_1Si mixtures pressed under various conditions. All spectra were obtained at 18.8 T with a spin-echo pulse sequence using 30° and 60° flip angles under static conditions.

3.3.2 Electrochemical comparison of Li_xSi in symmetric, half, and full cells

Although Si is a semiconductor, its low electronic conductivity (in the range of 10^{-4} S cm^{-1}), results in a large overpotential within the cell. The conventional way to overcome this barrier is to add carbon or some conductive agent, creating a silicon composite anode. However, the addition of Li into silicon could be another way to increase the electronic conductivity of Si dramatically. **Figure 3.7a** shows that as Li content increases, the Li_xSi electronic conductivity increases from 10^{-4} (Li_0Si) to 10 S cm^{-1} (Li_2Si). Since pressure-induced lithiation of Si was proven to be an effective approach from the previous section, we evaluated the electrochemical properties of Li_xSi in the cell configuration of symmetric, half and full cells. In **Figure 3.7b**, the plating and stripping of Li_xSi symmetric cells were conducted to evaluate the overpotential of each cell. The

overpotentials of cells decrease with more Li in Si, which is consistent with higher electronic conductivity of higher Li content Si from **Figure 3.7a**. The high electronically conductive Li_2Si symmetric cell had much smaller overpotential than $Li_{0.25}Si$ symmetric cell. Electrochemical impedance spectroscopy (EIS) was used to evaluate the resistance of Li_xSi symmetric cells before and after lithiation and delithiation respectively in **Figure 3.7c** and **Figure 3.7d**. Before plating and stripping, the resistance of $Li_{0.25}Si$ is higher than that of Li_1Si or Li_2Si due to the poor contact between two electrodes and LPSCl electrolyte pellet because of stiffness of low lithiated silicon (please note that the resistance of around 35 Ohm mainly comes from the ionic conductivity of LPSCl pellet between two electrode (~ 2.2 mS cm^{-1}). The resistance value slightly decreased after plating and stripping, maintaining the trend of higher Li content in Si resulting in lower impedance. The resistance values of Li_1Si and Li_2Si before and after plating were comparable to the ionic conductivity of the sulfide electrolyte Li_6PS_5Cl (LPSCl) electrolyte layer, indicating Li_1Si nor Li_2Si is not a dominant component of the cell resistance. **Figure 3.7e** shows the half-cell configuration of Li_xSi with Li metal. All Li_xSi was first lithiated for 1-hour and then delithiated for 1-hour at the same current density. Interestingly, all Li_xSi exhibited similar overpotential during the lithiation, indicating that Li reacting with Si into Li_xSi requires a similar amount of overpotential. The non-prelithiated Si clearly showed a higher overpotential when it was first lithiated due to its poorer electronic conductivity. However, the overpotential of the delithiated process is prominently different depending on the degree of prelithiation. This indicates that the amount of prelithiation eventually affects the electronic/ionic conductivity of silicon during charge and discharge. There are two sources of irreversible capacity during the first cycle; one is the electrolyte decomposition on the interface and the other is Li trapped inside Si,[91] which are successfully compensated for by our prelithiation strategy.

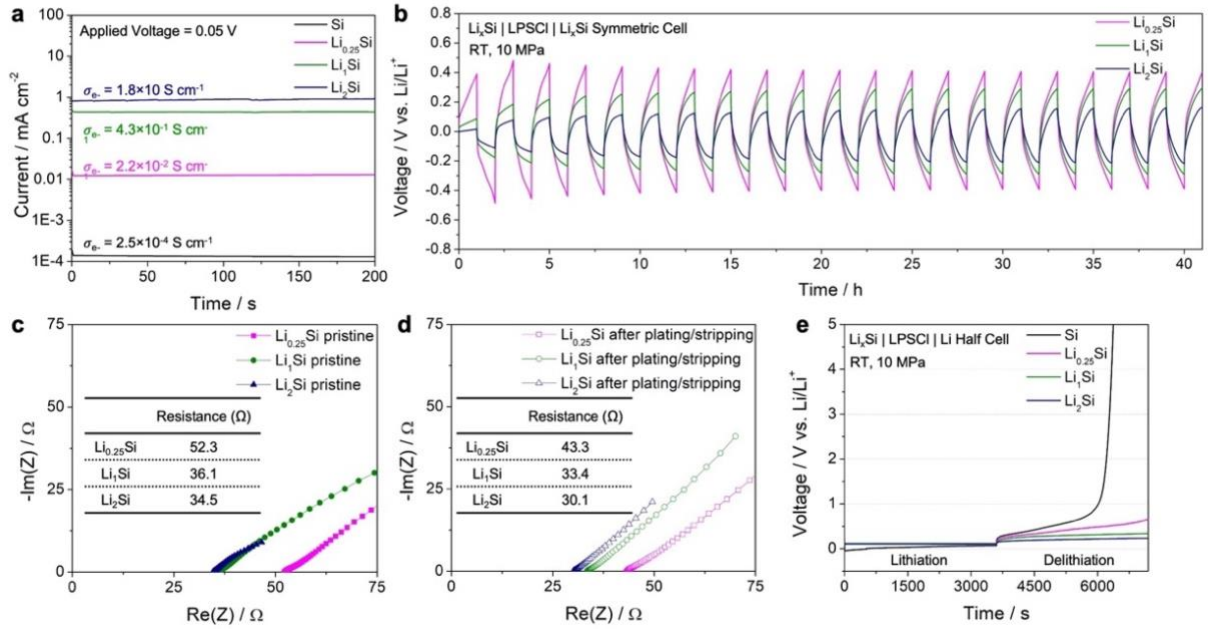

Figure 3.7 Conductivites and electrochemical properties of Li_xSi in symmetric and half-cells. a) The electronic conductivity of Si and vortex mixed Li_1Si using direct current polarization. b) Plating and stripping of Li_xSi (x=0.25, 1, and 2) for 20 cycles at 0.2 mA cm^{-2}. c) EIS measurement of Li_xSi symmetric cell before plating/stripping. d) EIS measurement of Li_1Si symmetric cell after plating/stripping at 0.2 mA cm^{-2}. e) Lithiation and delithiation of Li_xSi half-cells with different lithiation states.

In **Figure 3.8a**, full cells with the following configuration, Li_xSi | LPSCl | LCO, were fabricated and cycled at C/20 to study the effect of various prelithiation amounts in Si, which was to evaluate the first cycle performance with limited lithium inventory. Although the charge capacities of all Li_xSi were similar, the discharge capacity of Li_xSi showed significant differences. This result is also reflected in the half-cell configuration in **Figure 3.7e**, where lithiation of Si (charging) is comparable but delithiation of Si (discharging) shows a dramatic change in ICE. The ICE of the LCO-Si full cell was 78.3% whereas the ICE of LCO-Li_1Si and LCO-Li_2Si was increased to over 95% (**Figure 3.8b**).

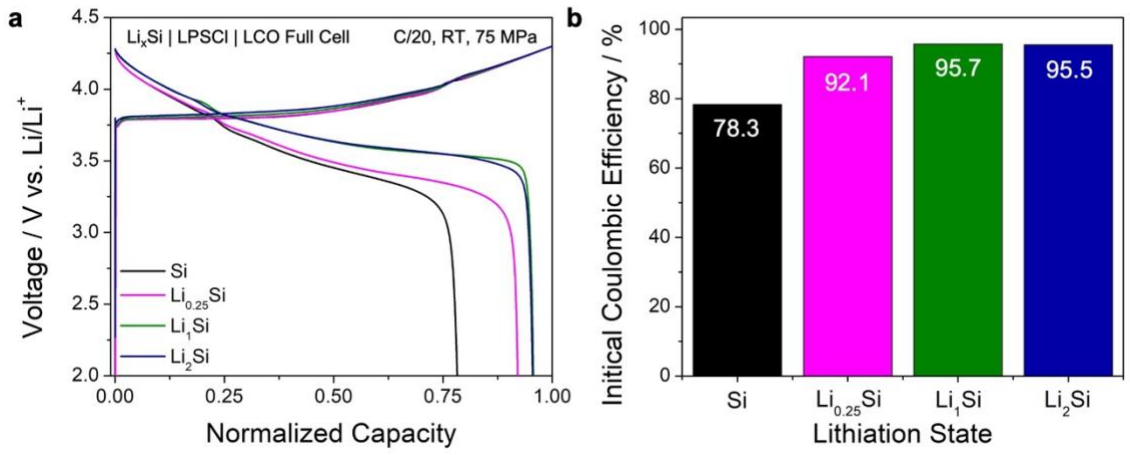

Figure 3.8 First cycle performances of Li_xSi full-cells. a) 1st cycle voltage curve of Li_xSi full cells with different lithiation states. LCO | LPSCl | Li_xSi cells were cycled at room temperature and 75 MPa. b) Initial Coulombic efficiency trend of Li_xSi (x = 0, 0.25, 1, and 2).

3.3.3 Full Cell ICE: Irreversible Capacity of Electrodes and N/P Ratio

3.3.3.1 Cathode limiting or anode limiting: NCM811/LCO and Si/Li_1Si

Two different cathodes were paired with Si and Li_1Si to elucidate the limiting component of the system (**Figure 3.9**). Based on the half-cell data of each component with a Li counter electrode, we can assume ICE of **NCM** as 75%, Si as 80%, and LCO as 95% (**Figure 3.10**). For NCM and LCO cathode paired with Si and lithiated Si, we can assume four cases. (**Figure 3.9a**) For the NCM/Si full-cell, the overall ICE is limited by the ICE of NCM, while the Si ICE determines the ICE of the LCO/Si full-cell. Therefore, pairing NCM with lithiated Si with excess Li on the anode side, the cell will still be limited by the ICE of NCM and will be unable to utilize the excess Li. However, by pairing LCO with lithiated Si, we can utilize the excess Li during the first discharge, and the cell can reach the ICE limit of LCO yielding 95%. Therefore, Case 1 (NCM/Si) and 3 (NCM/Li_xSi) can be regarded as the cathode-limiting system, while Case 2 (LCO/Si) is anode-limiting system. This means that prelithiation is only effective if the full-cell is

anode limited. Cells corresponding to each of these four cases were fabricated to demonstrate this hypothesis. In **Figure 3.9b**, which shows the NCM811 case, the ICE improvement at C/20 was marginal after prelithiation. However, the ICE of LCO cells increased significantly from 78.3% to 95.7% **(Figure 3.9c)**. The first-cycle voltage profiles from these cells were consistent with the hypothesis illustrated in **Figure 3.9a** Case 2 and Case 4. As the **Figure 3.9a** Case 4 achieved the highest ICE of 95.7%, the further long cycling and higher loading efforts are all made in this configuration. For From the rate tests in **Figure 3.11a** and **b**, lithiated Si always showed higher discharge capacity than non-lithiated Si for all current densities.

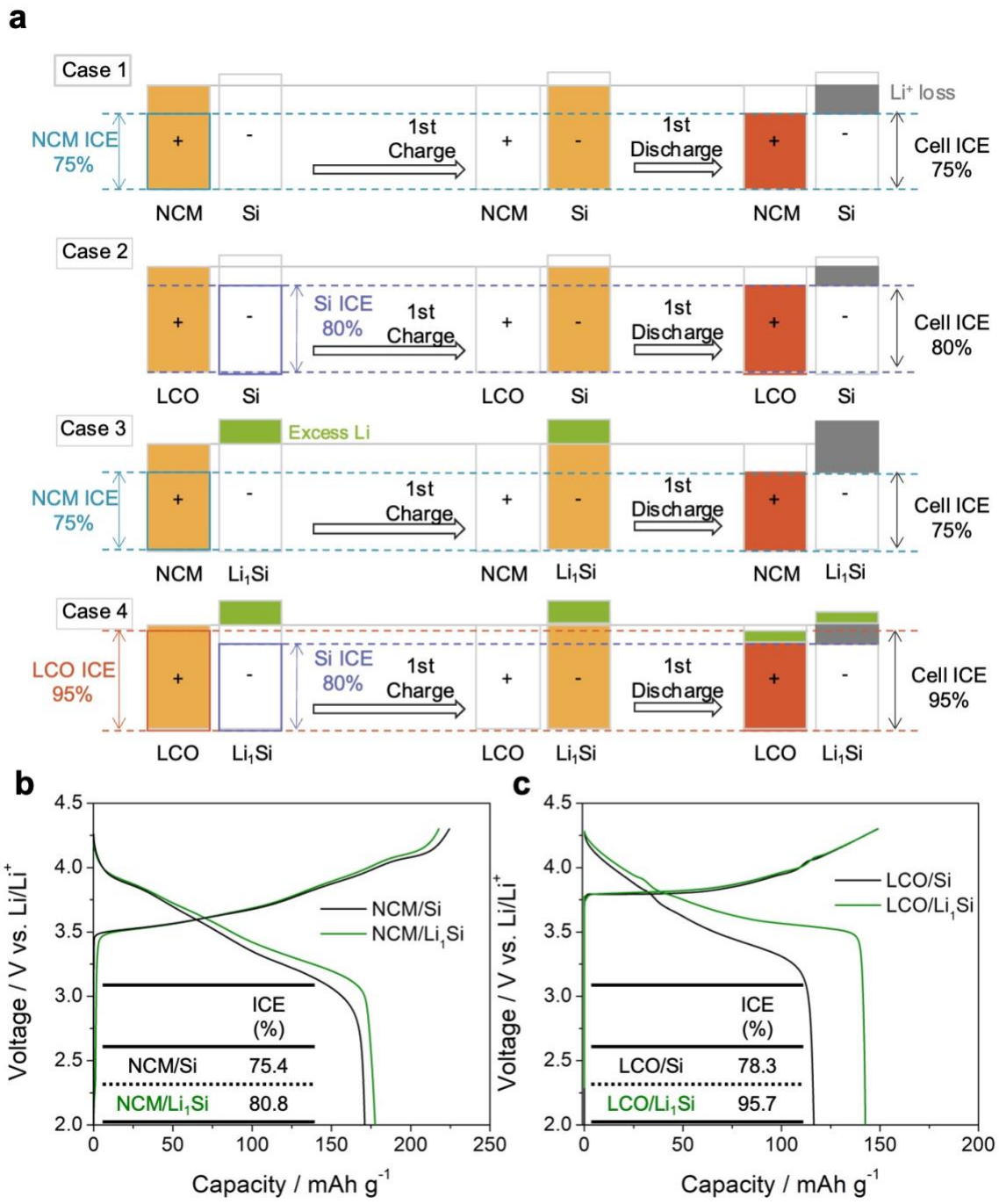

Figure 3.9 Prelithiation driven improvement of cathode anode limiting cases. a) Schematic illustrating ICE estimates of the Si and Li_1Si paired with NCM and LCO cathodes. First-cycle voltage profiles of b) NCM811 and c) LCO paired with Si and Li_1Si at C/20

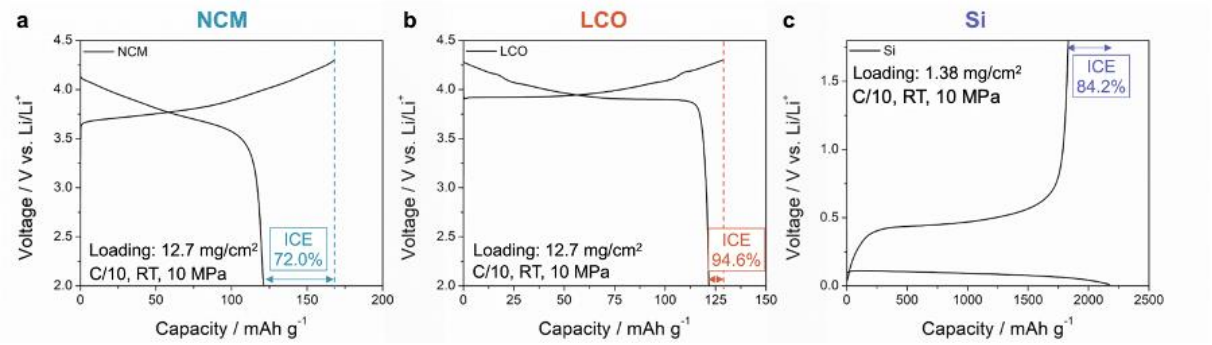

Figure 3.10 Half-cell data of (a) NCM, (b) LCO, and (c) Si with Li metal counter electrode. All cells were cycled at C/10, room temperature, and 10 MPa.

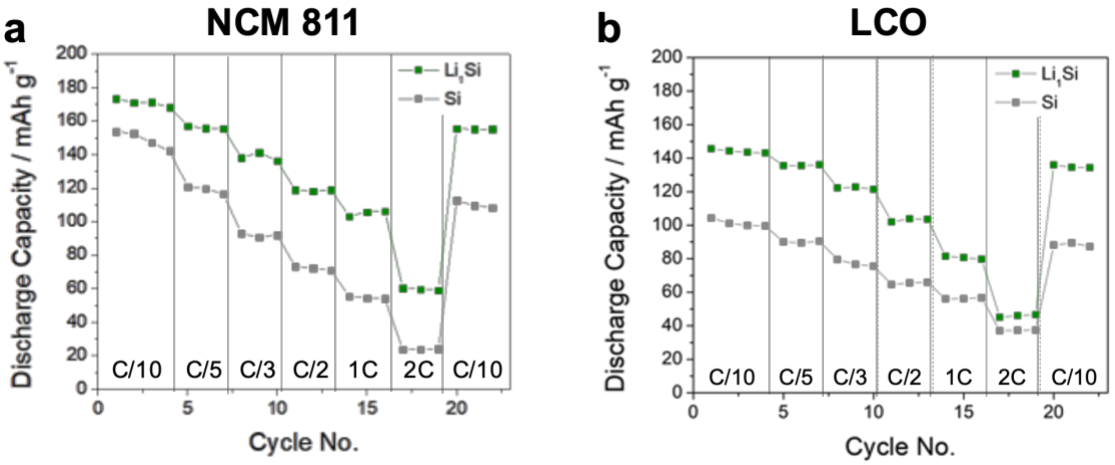

Figure 3.11 Rate tests of (a) NCM 811 and (b) LCO paired with Si and Li_1Si

3.3.3.2 N/P Ratio Consideration

There is one more important point regarding the N/P ratio. Although the illustration in **Figure 3.9a** explained the ICE of full-cell depending on the cathode-/anode-limiting system based on the N/P ratio of around 1, we obtained the experimental results (**Figure 3.9b** and **3.9c**) at the relatively high N/P ratio of 4.4. A high N/P ratio generally decreases ICE since irreversible lithium/electron consumption happens at a relatively high voltage (the initial stage of the lithiation process). However, our results show that the full-cell which has a wide range of N/P ratio (1~3.3)

exhibits similar ICE values (**Figure 3.12**), because some anode parts practically don't participate in the lithiation process (**Figure 3.13**). It makes the effective N/P ratio of our solid-state cell around 1, consistent with the illustration. Therefore, the discussion at the beginning of this section of Case 1 to Case 4 is valid even with higher loading of Si.

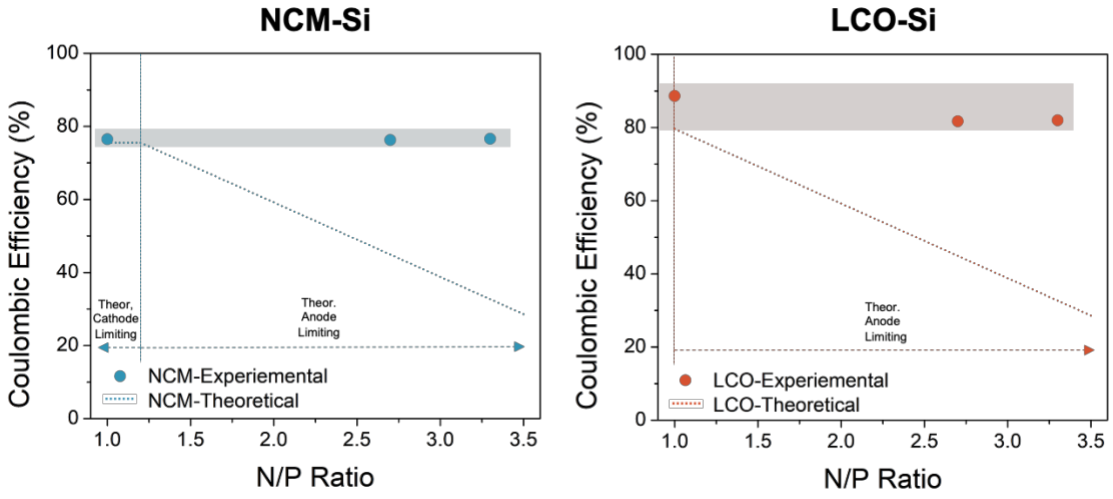

Figure 3.12 Theoretical and experimental Coulombic efficiency of NCM-Si and LCO Si of N/P 1 to 3.3.

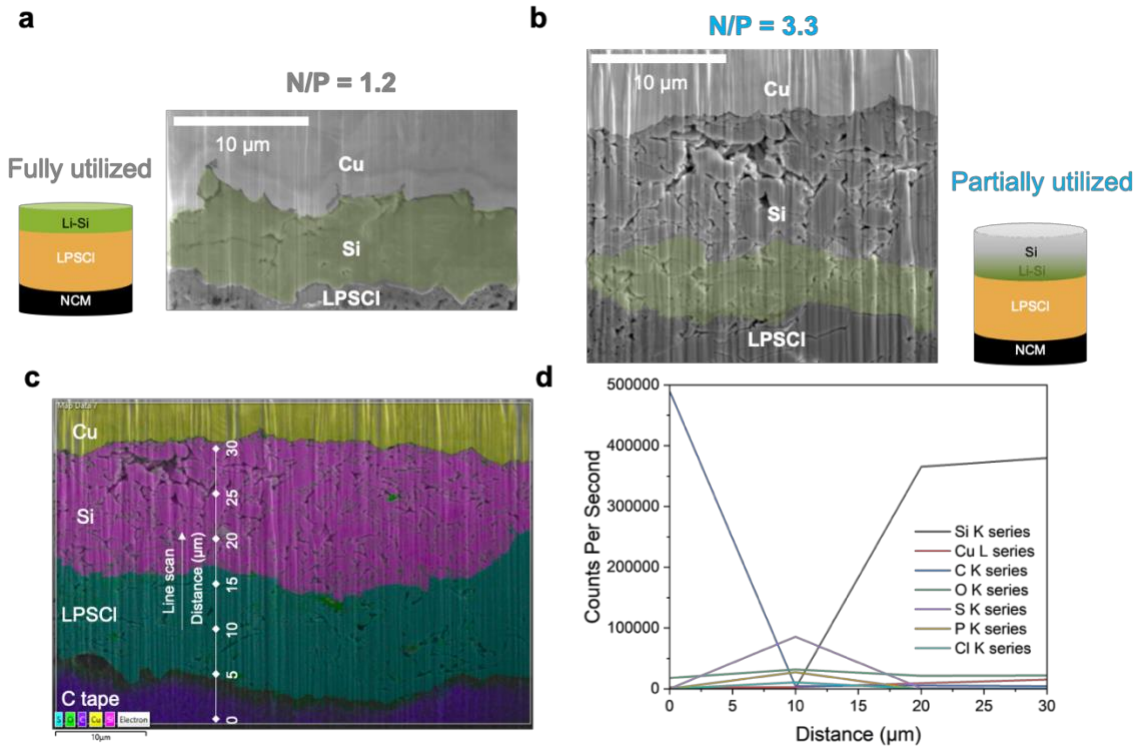

Figure 3.13 Cross-sectional FIB/SEM image of charged Si full cell of (a) N/P 1.2 and (b) 3.3. (c) EDS mapping of the charged N/P 3.3 Si cell. (d) Line scan of the charged N/P 3.3 Si cell. The line scan points and distance were denoted in Figure S8c.

The morphology of Li_1Si upon charging and discharging was demonstrated in **Figure 3.14**. The charged Li_1Si cross-sectional image shows that the partial utilization of Si is valid even in the Li_1Si case, meaning only the LPSCl facing side of Li_1Si gets lithiated whereas the opposite current collector side still has unreacted Li metal (dark) as we discussed earlier. The discharged sample exhibited surface cracks in some parts of the electrode (**Figure 3.14f**) where the cross-sectional image of the non-cracked part was shown in **Figure 3.14d** and the cracked part shown in **Figure 3.14e**, which indicated the existence of a huge volume change of the silicon electrode. In addition, the volume expansion from pristine to charged state was ~200% (**Figure 3.14**), and the discharged state showed minimal difference in thickness compared to the pristine state. The volume expansion

rate seems to be below the reported lithiated Si, but this is mostly because Li_1Si was partially lithiated where part of the anode was not utilized. Still, the relatively lower volume expansion rate could benefit the long-term cycling of Li_1Si.

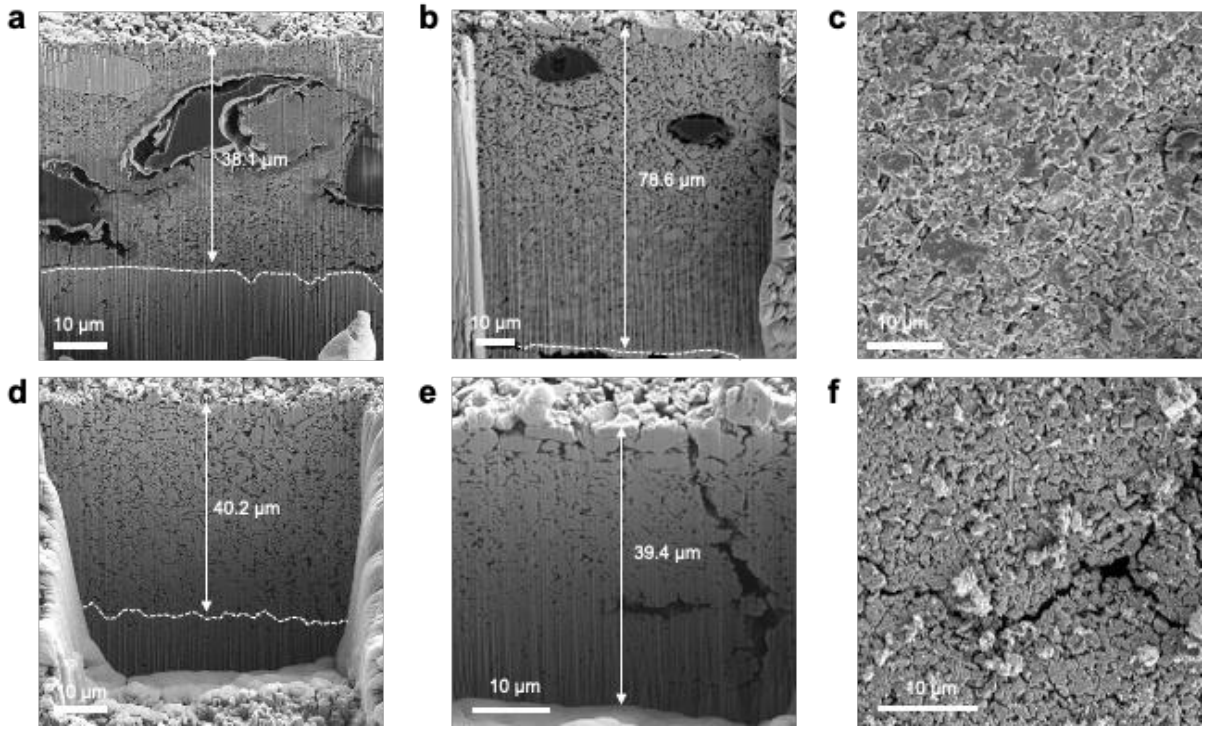

Figure 3.14 Cross-sectional FIB/SEM image of (a) pristine, (b) charged (d) discharged non-cracked spot (e) discharged cracked spot. Surface SEM image of (c) charged and (f) discharged. All images were obtained from Li_1Si samples. The charged and discharged samples were all first cycle results of Li_1Si cells.

3.3.4 Ramping test and long cycling of prelithiated Si

A ramping test using Si (**Figure 3.15a**) and Li_1Si (**Figure 3.15b**) was conducted to evaluate the lithiation effect on critical current density. Both Si and Li_1Si did not short, even up to 10 mA cm^{-2}. The areal capacities of a LCO cathode composite in all cells were 4 mAh cm^{-2}. For the first cycle at 0.25 mA cm^{-2}, both cells showed similar charge capacity suggesting good utilization of

the cathode materials from the same loading. However, from the first discharge step, the difference in capacity begins to dominate, which is always higher when paired with Li_1Si. The cycling stability of both Si and Li_1Si full cells, cycled at 5 mA cm^{-2} is shown in **Figure 3.15c**. Even with the high rate of 1.25C (1C = 4.0 mAh cm^{-2}), the retention of Li_1Si cell was 73.8% after 1000 cycles with an average CE of 99.9%, whereas the non-lithiated Si cell demonstrated 58.7% retention after 1000 cycles. As discussed in Figure 3e, for the Si full-cell, decrease in reversible capacity originates from electrolyte decomposition at the interface (especially LPSCl/Si interface) and Li trapped in Si. Even though stabilized LPSCl/Si interface after first few cycles helps the Si full-cells to have excellent CE and cyclability, it can be clearly seen that cells with more Li inventory (excess Li by prelithiation) have better cyclability. This further supports the room temperature lithiated Si could work at high rates for extended cycling.

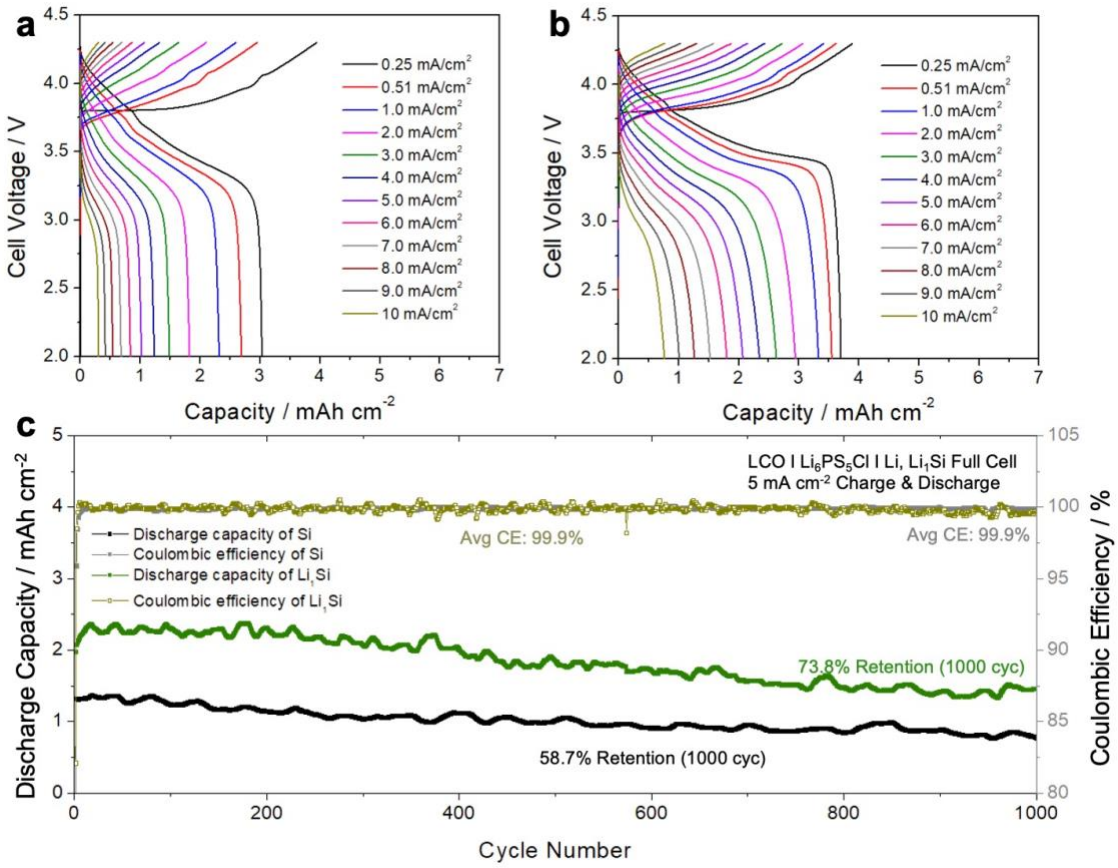

Figure 3.15 Cycling performance of Si and Li_1Si full cells. Ramping test to evaluate the critical current density of (a) Si and (b) Li_1Si. (c) Cycling performance of Si and Li_1Si cell at 5 mA cm^{-2}.

Interestingly, the cycling trend of lithiated Si shows an initial discharge capacity increase rather than decay. To better understand the full cells, EIS was measured for both cases upon cycling. This initial increase in discharge capacity could be attributed to residual Li metal not lithiated to Li_xSi which then becomes lithiated electrochemically in subsequent cycles. In **Figure 3.16**, in-situ EIS of the full cell using both Si and Li_xSi shows a decrease in resistance as it cycles. However, the magnitude of the resistance decrease is much higher for the Li_xSi. This implies that the remaining Li in Li_xSi would keep lithiating the unlithiated Si as it cycles.

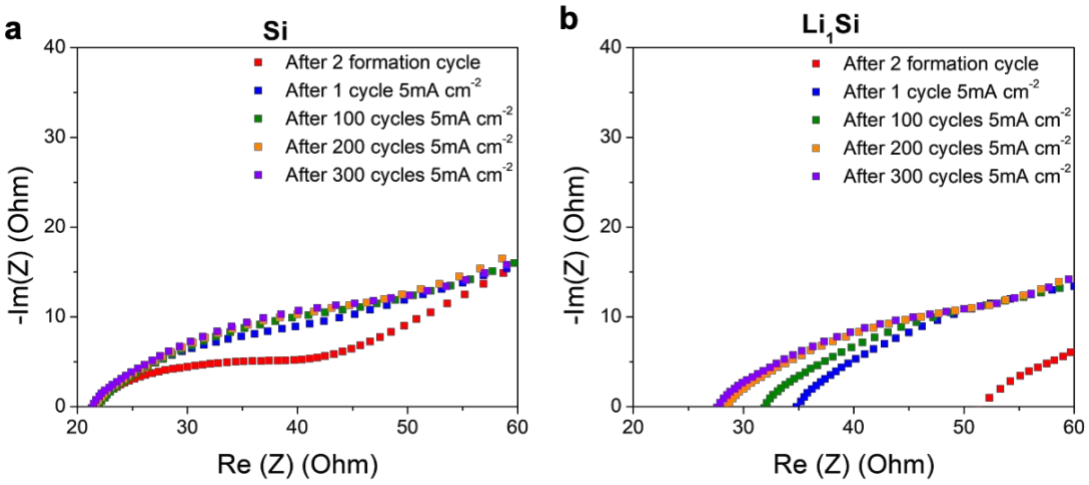

Figure 3.16 EIS of Si and Li_1Si upon cycling

3.3.5 High Loading Full Cell with Improved ICE

Considering the amount of Si used in the cell, all cells exhibit a high N/P ratio. The amount of Si used was fixed to 5 mg for all cells, yielding ~14 mAh of theoretical anode capacity and N/P ~ 4.4. As such, increasing the cathode loading to match the high capacity of anode was needed. However, with regards to the high-loading thick electrode, an inhomogeneous reaction within the thick electrode has been reported previously, showing lithium-ion diffusion limitation which resulted in the state of charge variation.[143,144] Therefore, a dry processing of cathode film consisting of cathode, catholyte and polytetrafluoroethylene (PTFE) binder was fabricated to achieve a better homogeneous electrochemical pathway within the thick electrode.[145] The cathode loadings were further increased in **Figure 3.17**, from dry process LCO loading of 22 mg to 42 mg and 57 mg, each corresponding to 3.7 mAh cm^{-2}, 8.0 mAh cm^{-2} and 10.8 mAh cm^{-2} of theoretical cathode capacity. The areal capacity from three different cathode loadings corresponds well with these theoretical cathode capacities. (**Figure 3.17a**) The gravimetric capacity of two higher loading cells decreased by 10 mAh g^{-1}, however, even for the 10 mAh cm^{-2} cell, capacity close to

theoretical capacity of LCO was achieved. This demonstrates the high capacity of lithiated Si in the full cell configuration. The energy density of the high loading cell has been calculated to be 236 Wh kg^{-1} and 947 Wh L^{-1} for the high loading 10.8 mAh cm^{-2} cell shown in Figure S11, which is based on the assumption that the solid electrolyte layer is 30 µm.

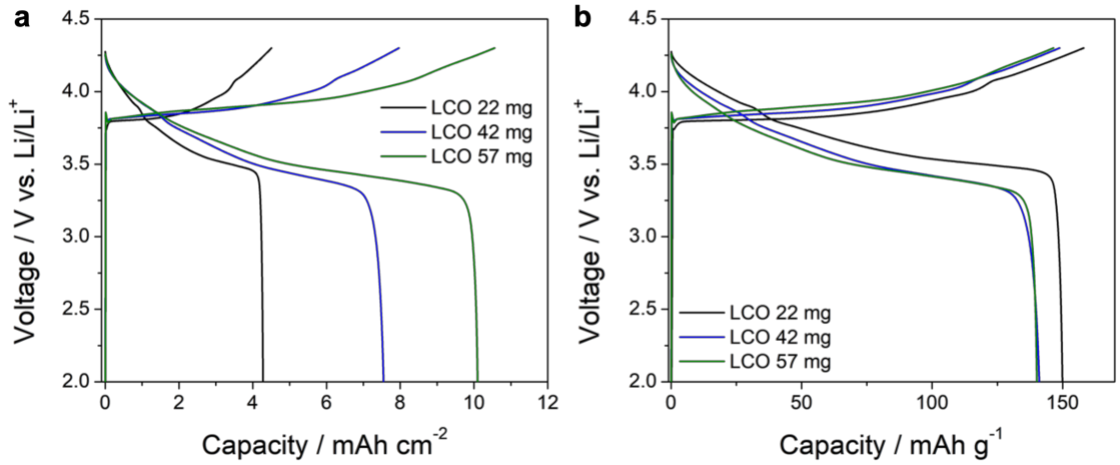

Figure 3.17 Voltage profiles of LCO cathode high loading cell paired with Li_1Si (a) areal capacity, (b) gravimetric capacity.

3.4 Conclusion

All-solid-state Si batteries have shown promising potential to enable high-capacity anode without continual SEI growth. However, the low ICE of Si remained a challenge to overcome for all-solid-state batteries. Here, a prelithiation strategy using the stabilized lithium was adopted to improve the ICE and conductivity of anodes. The lithiated Si was examined in symmetric-, half-, and full-cell configuration to understand the cell- level improvement of each component. With Li_1Si and LCO used as the anode and cathode, respectively, the full cell showed over 95% of ICE. In this work, we have identified why the prelithiation effect would dominate only for the anode-limited cases by comparing NCM and LCO paired with Si and Li_xSi. The ramping test and the long cycling performance were evaluated for both Si and Li_1Si cells. The Li_1Si demonstrated a large

improvement of 73.8% after 1000 cycles, a 15% improvement in retention. Furthermore, using Li_1Si, a high areal capacity of 10 mAh cm^{-2} was achieved and demonstrated using a dry-process LCO film, demonstrating that the lithiated Si could be a suitable candidate to be used in high-energy-density next-generation batteries.

Acknowledgement

Chapter 3, in full, is a reprint of the material as it appears in "S.-Y. Ham, E. Sebti, A. Cronk, T. Pennebaker, G. Deysher, Y.-T. Chen, J.A.S. Oh, J.B. Lee, M.S. Song, P. Ridley, D.H.S. Tan, R.J. Clément, J. Jang, Y.S. Meng, Overcoming low initial coulombic efficiencies of Si anodes through prelithiation in all-solid-state batteries, *Nat Commun* **15** (2024) 2991."

Chapter 4 Summary and Perspective

All-solid-state batteries (ASSBs) have gained significant attention from both academia and industry in recent years. The progress made in the past five years has been remarkable, with groundbreaking papers being published regularly. The growth in this field is accelerating as ASSBs benefit from the application of cathode and anode materials traditionally used in conventional lithium-ion batteries (LIBs). Notably, ASSBs have achieved breakthroughs such as anode-free configurations and pure silicon anodes, which can significantly improve gravimetric energy density and offer unprecedented cyclability compared to LIBs.

Major companies from Japan (Nissan, Toyota, Honda) and Korea (Samsung and LG Energy Solution), along with U.S. startups like SolidPower, have publicly announced plans to commercialize ASSBs by 2030. Although previous target dates for commercial production have not always been met, the presence of pilot production lines for ASSBs is increasing. Assuming these companies succeed in mass-producing ASSBs and they become a viable option for electric vehicles (EVs), electric vertical take-off and landing (eVTOL) aircraft, or small electronics, the best choice will depend on several factors. Realistically, ASSBs will likely have a higher price point compared to mass-produced LIBs. Therefore, to justify the cost, ASSBs must offer significantly superior features, such as extremely high energy density enabled by silicon or lithium metal anodes, and enhanced safety due to non-flammable solid electrolytes. The most promising market for such batteries would be premium EVs with energy densities of around 500 Wh/kg that could promise the longer driving range.

Despite significant progress, several challenges remain unresolved in the development of ASSBs. The primary obstacles are as follows:

1. Stack pressure management: The most critical issue is managing stack pressure, including both external pressure and pressure changes during cell cycling. ASSBs depend on solid-to-solid contact, and materials with high volume changes can lead to contact loss and cell degradation over time. To address pressure issues, a stable pressure application setup is necessary to operate ASSBs within an appropriate pressure range. While proof-of-concept studies have demonstrated constant pressure and isostatic pressure setups, these methods have yet to be scaled to industrial levels. Additionally, designing cells with zero net volume expansion could mitigate pressure changes. High-capacity anodes like lithium metal and silicon undergo significant volume expansion. Although various strategies, such as using nanostructures, have been developed to reduce this expansion, it is unlikely that these anodes will experience no volume change during cycling. Pairing these high-volume change anodes (Li metal or Si) with other volume-changing cathodes (sulfur) could be a solution. With proper calculations, the net volume change could be zero, thereby alleviating pressure concerns.
2. Operating temperature: Current ASSBs require high temperatures to operate efficiently. For example, the state-of-the-art cell showed impressive cyclability at 60°C, but the capacity obtained at room temperature was significantly lower.
3. Fast discharge (high-power viability) and fast charge capability: The current state of fast discharge or high-power capability is insufficient for applications such as eVTOL (electric vertical takeoff and landing). Because Li metal anode is not limited by low diffusivity like Si, it is more likely to achieve fast discharge. The fast charging capability also needs

improvement, as lengthy charging processes would make ASSBs unsuitable as a power source for eVTOL. Due to the low critical current density of Li metal cells, Si would be a better anode candidate for fast charging cells.

4. Cycle life: The cycle life of ASSBs is a major concern. Given the high projected cost of ASSBs, frequent replacement after a few hundred cycles would not be commercially viable. Repeated charge and discharge cycles can cause mechanical stress and material degradation, leading to capacity fade over time.
5. Solid electrolyte improvement: The current solid electrolytes, such as lithium argyrodite sulfide, have limited electrochemical windows, ionic conductivity, processability, and moisture sensitivity. Improving the solid electrolyte material itself could lower the solid electrolyte fraction in the cathode composite, resulting in higher active loading.
6. Manufacturing costs: ASSBs are currently more expensive to manufacture than conventional batteries, losing cost competitiveness. Both material and processing costs need to be reduced. The current warm isostatic press method for ASSB fabrication is limited to batch processing and has not been translated to a continuous process. The combined high cost of materials and processing results in a higher price compared to conventional batteries.

By addressing these challenges and leveraging the inherent advantages of ASSBs, commercial production and widespread adoption in high-performance applications can be achieved. This dissertation focused on high-capacity anodes for ASSBs. The use of lithium metal anodes in ASSBs requires solving cell shorting driven by dendrite propagation, thus critical current density evaluation and volume expansion accommodation through a modified cycling framework were revisited. Silicon anodes were also discussed, with a prelithiation strategy to overcome the

first cycle capacity loss. Prelithiated silicon cells achieved high initial capacity with higher operational current density, and the formation of silicon alloys within thick anode layers was examined to further understand silicon in ASSBs. Overall, this dissertation aimed to deepen the understanding of high-capacity anodes for ASSBs and address the challenges outlined above.

REFERENCES

(1) Dixit, M.; Bisht, A.; Essehli, R.; Amin, R.; Kweon, C.-B. M.; Belharouak, I. Lithium-Ion Battery Power Performance Assessment for the Climb Step of an Electric Vertical Takeoff and Landing (eVTOL) Application. *ACS Energy Lett.* **2024**, *9* (3), 934–940. https://doi.org/10.1021/acsenergylett.3c02385.

(2) Liu, X.; Zhao, F.; Geng, J.; Hao, H.; Liu, Z. Comprehensive Assessment for Different Ranges of Battery Electric Vehicles: Is It Necessary to Develop an Ultra-Long Range Battery Electric Vehicle? *iScience* **2023**, *26* (6), 106654. https://doi.org/10.1016/j.isci.2023.106654.

(3) Asenbauer, J.; Eisenmann, T.; Kuenzel, M.; Kazzazi, A.; Chen, Z.; Bresser, D. The Success Story of Graphite as a Lithium-Ion Anode Material – Fundamentals, Remaining Challenges, and Recent Developments Including Silicon (Oxide) Composites. *Sustainable Energy Fuels* **2020**, *4* (11), 5387–5416. https://doi.org/10.1039/D0SE00175A.

(4) Chang, Z.; Yang, H.; Zhu, X.; He, P.; Zhou, H. A Stable Quasi-Solid Electrolyte Improves the Safe Operation of Highly Efficient Lithium-Metal Pouch Cells in Harsh Environments. *Nat Commun* **2022**, *13* (1), 1510. https://doi.org/10.1038/s41467-022-29118-6.

(5) Zhao, Q.; Stalin, S.; Zhao, C.-Z.; Archer, L. A. Designing Solid-State Electrolytes for Safe, Energy-Dense Batteries. *Nat Rev Mater* **2020**, *5* (3), 229–252. https://doi.org/10.1038/s41578-019-0165-5.

(6) Han, L.; Wang, L.; Chen, Z.; Kan, Y.; Hu, Y.; Zhang, H.; He, X. Incombustible Polymer Electrolyte Boosting Safety of Solid-State Lithium Batteries: A Review. *Adv Funct Materials* **2023**, 2300892. https://doi.org/10.1002/adfm.202300892.

(7) Guo, Y.; Wu, S.; He, Y.-B.; Kang, F.; Chen, L.; Li, H.; Yang, Q.-H. Solid-State Lithium Batteries: Safety and Prospects. *eScience* **2022**, *2* (2), 138–163. https://doi.org/10.1016/j.esci.2022.02.008.

(8) Meabe, L.; Aldalur, I.; Lindberg, S.; Arrese-Igor, M.; Armand, M.; Martinez-Ibañez, M.; Zhang, H. Solid-State Electrolytes for Safe Rechargeable Lithium Metal Batteries: A Strategic View. *Mater. Futures* **2023**. https://doi.org/10.1088/2752-5724/accdf3.

(9) Tan, D. H. S.; Meng, Y. S.; Jang, J. Scaling up High-Energy-Density Sulfidic Solid-State Batteries: A Lab-to-Pilot Perspective. *Joule* **2022**, *6* (8), 1755–1769. https://doi.org/10.1016/j.joule.2022.07.002.

(10) He, L.; Sun, Q.; Lu, L.; Adams, S. Understanding and Preventing Dendrite Growth in Lithium Metal Batteries. *ACS Appl. Mater. Interfaces* **2021**, *13* (29), 34320–34331. https://doi.org/10.1021/acsami.1c08268.

(11) Lee, H. G.; Kim, S. Y.; Lee, J. S. Dynamic Observation of Dendrite Growth on Lithium Metal Anode during Battery Charging/Discharging Cycles. *npj Comput Mater* **2022**, *8* (1), 103. https://doi.org/10.1038/s41524-022-00788-6.

(12) Wang, S.; Xu, H.; Li, W.; Dolocan, A.; Manthiram, A. Interfacial Chemistry in Solid-State Batteries: Formation of Interphase and Its Consequences. *J. Am. Chem. Soc.* **2018**, *140* (1), 250–257. https://doi.org/10.1021/jacs.7b09531.

(13) Richards, W. D.; Miara, L. J.; Wang, Y.; Kim, J. C.; Ceder, G. Interface Stability in Solid-State Batteries. *Chem. Mater.* **2016**, *28* (1), 266–273. https://doi.org/10.1021/acs.chemmater.5b04082.

(14) Tan, D. H. S.; Banerjee, A.; Chen, Z.; Meng, Y. S. From Nanoscale Interface Characterization to Sustainable Energy Storage Using All-Solid-State Batteries. *Nat. Nanotechnol.* **2020**, *15* (3), 170–180. https://doi.org/10.1038/s41565-020-0657-x.

(15) Banerjee, A.; Wang, X.; Fang, C.; Wu, E. A.; Meng, Y. S. Interfaces and Interphases in All-Solid-State Batteries with Inorganic Solid Electrolytes. *Chem. Rev.* **2020**, *120* (14), 6878–6933. https://doi.org/10.1021/acs.chemrev.0c00101.

(16) Kamaya, N.; Homma, K.; Yamakawa, Y.; Hirayama, M.; Kanno, R.; Yonemura, M.; Kamiyama, T.; Kato, Y.; Hama, S.; Kawamoto, K.; Mitsui, A. A Lithium Superionic Conductor. *Nature Mater* **2011**, *10* (9), 682–686. https://doi.org/10.1038/nmat3066.

(17) Seino, Y.; Ota, T.; Takada, K.; Hayashi, A.; Tatsumisago, M. A Sulphide Lithium Super Ion Conductor Is Superior to Liquid Ion Conductors for Use in Rechargeable Batteries. *Energy Environ. Sci.* **2014**, *7* (2), 627–631. https://doi.org/10.1039/C3EE41655K.

(18) Tan, D. H. S.; Wu, E. A.; Nguyen, H.; Chen, Z.; Marple, M. A. T.; Doux, J.-M.; Wang, X.; Yang, H.; Banerjee, A.; Meng, Y. S. Elucidating Reversible Electrochemical Redox of Li_6PS_5Cl Solid Electrolyte. *ACS Energy Lett.* **2019**, *4* (10), 2418–2427. https://doi.org/10.1021/acsenergylett.9b01693.

(19) Wu, E. A.; Jo, C.; Tan, D. H. S.; Zhang, M.; Doux, J.-M.; Chen, Y.-T.; Deysher, G.; Meng, Y. S. A Facile, Dry-Processed Lithium Borate-Based Cathode Coating for Improved All-Solid-State Battery Performance. *J. Electrochem. Soc.* **2020**, *167* (13), 130516. https://doi.org/10.1149/1945-7111/abb8b3.

(20) Walther, F.; Strauss, F.; Wu, X.; Mogwitz, B.; Hertle, J.; Sann, J.; Rohnke, M.; Brezesinski, T.; Janek, J. The Working Principle of a Li_2CO_3/$LiNbO_3$ Coating on NCM for Thiophosphate-Based All-Solid-State Batteries. *Chem. Mater.* **2021**, *33* (6), 2110–2125. https://doi.org/10.1021/acs.chemmater.0c04660.

(21) Liang, Y.; Liu, H.; Wang, G.; Wang, C.; Ni, Y.; Nan, C.; Fan, L. Challenges, Interface Engineering, and Processing Strategies toward Practical SULFIDE-BASED ALL-SOLID-STATE Lithium Batteries. *InfoMat* **2022**, *4* (5), e12292. https://doi.org/10.1002/inf2.12292.

(22) Asano, T.; Sakai, A.; Ouchi, S.; Sakaida, M.; Miyazaki, A.; Hasegawa, S. Solid Halide Electrolytes with High Lithium-Ion Conductivity for Application in 4 V Class Bulk-Type All-Solid-State Batteries. *Adv. Mater.* **2018**, *30* (44), 1803075. https://doi.org/10.1002/adma.201803075.

(23) Park, K.-H.; Kaup, K.; Assoud, A.; Zhang, Q.; Wu, X.; Nazar, L. F. High-Voltage Superionic Halide Solid Electrolytes for All-Solid-State Li-Ion Batteries. *ACS Energy Lett.* **2020**, *5* (2), 533–539. https://doi.org/10.1021/acsenergylett.9b02599.

(24) Wang, C.; Fu, K.; Kammampata, S. P.; McOwen, D. W.; Samson, A. J.; Zhang, L.; Hitz, G. T.; Nolan, A. M.; Wachsman, E. D.; Mo, Y.; Thangadurai, V.; Hu, L. Garnet-Type Solid-State Electrolytes: Materials, Interfaces, and Batteries. *Chem. Rev.* **2020**, *120* (10), 4257–4300. https://doi.org/10.1021/acs.chemrev.9b00427.

(25) Masias, A.; Felten, N.; Garcia-Mendez, R.; Wolfenstine, J.; Sakamoto, J. Elastic, Plastic, and Creep Mechanical Properties of Lithium Metal. *J Mater Sci* **2019**, *54* (3), 2585–2600. https://doi.org/10.1007/s10853-018-2971-3.

(26) Ding, S.; Fairgrieve-Park, L.; Sendetskyi, O.; Fleischauer, M. D. Compressive Creep Deformation of Lithium Foil at Varied Cell Conditions. *Journal of Power Sources* **2021**, *488*, 229404. https://doi.org/10.1016/j.jpowsour.2020.229404.

(27) Zhang, X.; Wang, Q. J.; Harrison, K. L.; Roberts, S. A.; Harris, S. J. Pressure-Driven Interface Evolution in Solid-State Lithium Metal Batteries. *Cell Reports Physical Science* **2020**, *1* (2), 100012. https://doi.org/10.1016/j.xcrp.2019.100012.

(28) Ham, S.-Y.; Yang, H.; Nunez-cuacuas, O.; Tan, D. H. S.; Chen, Y.-T.; Deysher, G.; Cronk, A.; Ridley, P.; Doux, J.-M.; Wu, E. A.; Jang, J.; Meng, Y. S. Assessing the Critical Current Density of All-Solid-State Li Metal Symmetric and Full Cells. *Energy Storage Materials* **2023**, *55*, 455–462. https://doi.org/10.1016/j.ensm.2022.12.013.

(29) Zhang, L.; Yang, T.; Du, C.; Liu, Q.; Tang, Y.; Zhao, J.; Wang, B.; Chen, T.; Sun, Y.; Jia, P.; Li, H.; Geng, L.; Chen, J.; Ye, H.; Wang, Z.; Li, Y.; Sun, H.; Li, X.; Dai, Q.; Tang, Y.; Peng, Q.; Shen, T.; Zhang, S.; Zhu, T.; Huang, J. Lithium Whisker Growth and Stress Generation in an in Situ Atomic Force Microscope–Environmental Transmission Electron Microscope Set-Up. *Nat. Nanotechnol.* **2020**, *15* (2), 94–98. https://doi.org/10.1038/s41565-019-0604-x.

(30) Kalnaus, S.; Dudney, N. J.; Westover, A. S.; Herbert, E.; Hackney, S. Solid-State Batteries: The Critical Role of Mechanics. *Science* **2023**, *381* (6664), eabg5998. https://doi.org/10.1126/science.abg5998.

(31) Sarkar, S.; Thangadurai, V. Critical Current Densities for High-Performance All-Solid-State Li-Metal Batteries: Fundamentals, Mechanisms, Interfaces, Materials, and Applications. *ACS Energy Lett.* **2022**, *7* (4), 1492–1527. https://doi.org/10.1021/acsenergylett.2c00003.

(32) Yan, H.; Tantratian, K.; Ellwood, K.; Harrison, E. T.; Nichols, M.; Cui, X.; Chen, L. How Does the Creep Stress Regulate Void Formation at the Lithium-Solid Electrolyte Interface during Stripping? *Advanced Energy Materials* **2022**, *12* (2), 2102283. https://doi.org/10.1002/aenm.202102283.

(33) Schwietert, T. K.; Arszelewska, V. A.; Wang, C.; Yu, C.; Vasileiadis, A.; De Klerk, N. J. J.; Hageman, J.; Hupfer, T.; Kerkamm, I.; Xu, Y.; Van Der Maas, E.; Kelder, E. M.; Ganapathy, S.; Wagemaker, M. Clarifying the Relationship between Redox Activity and Electrochemical Stability in Solid Electrolytes. *Nat. Mater.* **2020**, *19* (4), 428–435. https://doi.org/10.1038/s41563-019-0576-0.

(34) Han, F.; Zhu, Y.; He, X.; Mo, Y.; Wang, C. Electrochemical Stability of Li $_{10}$ GeP $_{2}$ S $_{12}$ and Li $_{7}$ La $_{3}$ Zr $_{2}$ O $_{12}$ Solid Electrolytes. *Advanced Energy Materials* **2016**, *6* (8), 1501590. https://doi.org/10.1002/aenm.201501590.

(35) Cronk, A.; Chen, Y.-T.; Deysher, G.; Ham, S.-Y.; Yang, H.; Ridley, P.; Sayahpour, B.; Nguyen, L. H. B.; Oh, J. A. S.; Jang, J.; Tan, D. H. S.; Meng, Y. S. Overcoming the Interfacial Challenges of LiFePO $_{4}$ in Inorganic All-Solid-State Batteries. *ACS Energy Lett.* **2023**, *8* (1), 827–835. https://doi.org/10.1021/acsenergylett.2c02138.

(36) Bron, P.; Dehnen, S.; Roling, B. Li10Si0.3Sn0.7P2S12 – A Low-Cost and Low-Grain-Boundary-Resistance Lithium Superionic Conductor. *Journal of Power Sources* **2016**, *329*, 530–535. https://doi.org/10.1016/j.jpowsour.2016.08.115.

(37) Krauskopf, T.; Hartmann, H.; Zeier, W. G.; Janek, J. Toward a Fundamental Understanding of the Lithium Metal Anode in Solid-State Batteries—An Electrochemo-Mechanical Study on the Garnet-Type Solid Electrolyte Li $_{6.25}$ Al $_{0.25}$ La $_{3}$ Zr $_{2}$ O $_{12}$. *ACS Appl. Mater. Interfaces* **2019**, *11* (15), 14463–14477. https://doi.org/10.1021/acsami.9b02537.

(38) Davis, A. L.; Kazyak, E.; Liao, D. W.; Wood, K. N.; Dasgupta, N. P. Operando Analysis of Interphase Dynamics in Anode-Free Solid-State Batteries with Sulfide Electrolytes. *J. Electrochem. Soc.* **2021**, *168* (7), 070557. https://doi.org/10.1149/1945-7111/ac163d.

(39) Jang, J.; Chen, Y.-T.; Deysher, G.; Cheng, D.; Ham, S.-Y.; Cronk, A.; Ridley, P.; Yang, H.; Sayahpour, B.; Han, B.; Li, W.; Yao, W.; Wu, E. A.; Doux, J.-M.; Nguyen, L. H. B.; Oh, J. A. S.; Tan, D. H. S.; Meng, Y. S. Enabling a Co-Free, High-Voltage LiNi $_{0.5}$ Mn $_{1.5}$ O $_{4}$ Cathode in All-Solid-State Batteries with a Halide Electrolyte. *ACS Energy Lett.* **2022**, *7* (8), 2531–2539. https://doi.org/10.1021/acsenergylett.2c01397.

(40) Auvergniot, J.; Cassel, A.; Ledeuil, J.-B.; Viallet, V.; Seznec, V.; Dedryvère, R. Interface Stability of Argyrodite Li $_{6}$ PS $_{5}$ Cl toward LiCoO $_{2}$, LiNi $_{1/3}$ Co $_{1/3}$ Mn $_{1/3}$ O $_{2}$, and LiMn $_{2}$ O $_{4}$ in Bulk All-Solid-State Batteries. *Chem. Mater.* **2017**, *29* (9), 3883–3890. https://doi.org/10.1021/acs.chemmater.6b04990.

(41) Ke, X.; Wang, Y.; Ren, G.; Yuan, C. Towards Rational Mechanical Design of Inorganic Solid Electrolytes for All-Solid-State Lithium Ion Batteries. *Energy Storage Materials* **2020**, *26*, 313–324. https://doi.org/10.1016/j.ensm.2019.08.029.

(42) Hikima, K.; Totani, M.; Obokata, S.; Muto, H.; Matsuda, A. Mechanical Properties of Sulfide-Type Solid Electrolytes Analyzed by Indentation Methods. *ACS Appl. Energy Mater.* **2022**, *5* (2), 2349–2355. https://doi.org/10.1021/acsaem.1c03829.

(43) Sakuda, A.; Hayashi, A.; Tatsumisago, M. Sulfide Solid Electrolyte with Favorable Mechanical Property for All-Solid-State Lithium Battery. *Sci Rep* **2013**, *3* (1), 2261. https://doi.org/10.1038/srep02261.

(44) Kato, A.; Yamamoto, M.; Sakuda, A.; Hayashi, A.; Tatsumisago, M. Mechanical Properties of Li_2S–P_2S_5 Glasses with Lithium Halides and Application in All-Solid-State Batteries. *ACS Appl. Energy Mater.* **2018**, *1* (3), 1002–1007. https://doi.org/10.1021/acsaem.7b00140.

(45) Marbella, L. E.; Zekoll, S.; Kasemchainan, J.; Emge, S. P.; Bruce, P. G.; Grey, C. P. ^{7}Li NMR Chemical Shift Imaging To Detect Microstructural Growth of Lithium in All-Solid-State Batteries. *Chem. Mater.* **2019**, *31* (8), 2762–2769. https://doi.org/10.1021/acs.chemmater.8b04875.

(46) Han, F.; Westover, A. S.; Yue, J.; Fan, X.; Wang, F.; Chi, M.; Leonard, D. N.; Dudney, N. J.; Wang, H.; Wang, C. High Electronic Conductivity as the Origin of Lithium Dendrite Formation within Solid Electrolytes. *Nat Energy* **2019**, *4* (3), 187–196. https://doi.org/10.1038/s41560-018-0312-z.

(47) Zhong, X.; Wade, C. A.; Withers, P. J.; Zhou, X.; Cai, C.; Haigh, S. J.; Burke, M. G. Comparing Xe^+ pFIB and Ga^+ FIB for TEM Sample Preparation of Al Alloys: Minimising FIB-induced Artefacts. *Journal of Microscopy* **2021**, *282* (2), 101–112. https://doi.org/10.1111/jmi.12983.

(48) Lu, Y.; Zhao, C.-Z.; Hu, J.-K.; Sun, S.; Yuan, H.; Fu, Z.-H.; Chen, X.; Huang, J.-Q.; Ouyang, M.; Zhang, Q. The Void Formation Behaviors in Working Solid-State Li Metal Batteries. *Sci. Adv.* **2022**, *8* (45), eadd0510. https://doi.org/10.1126/sciadv.add0510.

(49) Cheng, D.; Wynn, T. A.; Wang, X.; Wang, S.; Zhang, M.; Shimizu, R.; Bai, S.; Nguyen, H.; Fang, C.; Kim, M.; Li, W.; Lu, B.; Kim, S. J.; Meng, Y. S. Unveiling the Stable Nature of the Solid Electrolyte Interphase between Lithium Metal and LiPON via Cryogenic Electron Microscopy. *Joule* **2020**, *4* (11), 2484–2500. https://doi.org/10.1016/j.joule.2020.08.013.

(50) Scharf, J.; Chouchane, M.; Finegan, D. P.; Lu, B.; Redquest, C.; Kim, M.; Yao, W.; Franco, A. A.; Gostovic, D.; Liu, Z.; Riccio, M.; Zelenka, F.; Doux, J.-M.; Meng, Y. S. Bridging Nano- and Microscale X-Ray Tomography for Battery Research by Leveraging Artificial Intelligence. *Nat. Nanotechnol.* **2022**, *17* (5), 446–459. https://doi.org/10.1038/s41565-022-01081-9.

(51) Pietsch, P.; Wood, V. X-Ray Tomography for Lithium Ion Battery Research: A Practical Guide. *Annu. Rev. Mater. Res.* **2017**, *47* (1), 451–479. https://doi.org/10.1146/annurev-matsci-070616-123957.

(52) Lewis, J. A.; Cortes, F. J. Q.; Liu, Y.; Miers, J. C.; Verma, A.; Vishnugopi, B. S.; Tippens, J.; Prakash, D.; Marchese, T. S.; Han, S. Y.; Lee, C.; Shetty, P. P.; Lee, H.-W.; Shevchenko, P.; De Carlo, F.; Saldana, C.; Mukherjee, P. P.; McDowell, M. T. Linking Void and Interphase Evolution to Electrochemistry in Solid-State Batteries Using Operando X-Ray Tomography. *Nat. Mater.* **2021**, *20* (4), 503–510. https://doi.org/10.1038/s41563-020-00903-2.

(53) Sun, X.; Stavola, A. M.; Cao, D.; Bruck, A. M.; Wang, Y.; Zhang, Y.; Luan, P.; Gallaway, J. W.; Zhu, H. Operando EDXRD Study of All-Solid-State Lithium Batteries Coupling Thioantimonate Superionic Conductors with Metal Sulfide. *Adv. Energy Mater.* **2021**, *11* (3), 2002861. https://doi.org/10.1002/aenm.202002861.

(54) Doux, J.; Nguyen, H.; Tan, D. H. S.; Banerjee, A.; Wang, X.; Wu, E. A.; Jo, C.; Yang, H.; Meng, Y. S. Stack Pressure Considerations for Room-Temperature All-Solid-State Lithium Metal Batteries. *Adv. Energy Mater.* **2020**, *10* (1), 1903253. https://doi.org/10.1002/aenm.201903253.

(55) Han, G.; Yan, J.; Guo, Z.; Greenwood, D.; Marco, J.; Yu, Y. A Review on Various Optical Fibre Sensing Methods for Batteries. *Renewable and Sustainable Energy Reviews* **2021**, *150*, 111514. https://doi.org/10.1016/j.rser.2021.111514.

(56) Liu, Y.; Liu, Z.; Mei, W.; Han, X.; Liu, P.; Wang, C.; Xia, X.; Li, K.; Wang, S.; Wang, Q.; Guo, T. Operando Monitoring Lithium-Ion Battery Temperature via Implanting Femtosecond-Laser-Inscribed Optical Fiber Sensors. *Measurement* **2022**, *203*, 111961. https://doi.org/10.1016/j.measurement.2022.111961.

(57) Albero Blanquer, L.; Marchini, F.; Seitz, J. R.; Daher, N.; Bétermier, F.; Huang, J.; Gervillié, C.; Tarascon, J.-M. Optical Sensors for Operando Stress Monitoring in Lithium-

Based Batteries Containing Solid-State or Liquid Electrolytes. *Nat Commun* **2022**, *13* (1), 1153. https://doi.org/10.1038/s41467-022-28792-w.

(58) Bond, T.; Gauthier, R.; Gasilov, S.; Dahn, J. R. In-Situ Computed Tomography of Particle Microcracking and Electrode Damage in Cycled NMC622/Graphite Pouch Cell Batteries. *J. Electrochem. Soc.* **2022**, *169* (8), 080531. https://doi.org/10.1149/1945-7111/ac8a22.

(59) Davies, G.; Knehr, K. W.; Van Tassell, B.; Hodson, T.; Biswas, S.; Hsieh, A. G.; Steingart, D. A. State of Charge and State of Health Estimation Using Electrochemical Acoustic Time of Flight Analysis. *J. Electrochem. Soc.* **2017**, *164* (12), A2746–A2755. https://doi.org/10.1149/2.1411712jes.

(60) Yi, M.; Jiang, F.; Lu, L.; Hou, S.; Ren, J.; Han, X.; Huang, L. Ultrasonic Tomography Study of Metal Defect Detection in Lithium-Ion Battery. *Front. Energy Res.* **2021**, *9*, 806929. https://doi.org/10.3389/fenrg.2021.806929.

(61) Deng, Z.; Huang, Z.; Shen, Y.; Huang, Y.; Ding, H.; Luscombe, A.; Johnson, M.; Harlow, J. E.; Gauthier, R.; Dahn, J. R. Ultrasonic Scanning to Observe Wetting and "Unwetting" in Li-Ion Pouch Cells. *Joule* **2020**, *4* (9), 2017–2029. https://doi.org/10.1016/j.joule.2020.07.014.

(62) Wood, K. N.; Noked, M.; Dasgupta, N. P. Lithium Metal Anodes: Toward an Improved Understanding of Coupled Morphological, Electrochemical, and Mechanical Behavior. *ACS Energy Letters* **2017**, *2* (3), 664–672. https://doi.org/10.1021/acsenergylett.6b00650.

(63) Hatzell, K. B.; Chen, X. C.; Cobb, C. L.; Dasgupta, N. P.; Dixit, M. B.; Marbella, L. E.; McDowell, M. T.; Mukherjee, P. P.; Verma, A.; Viswanathan, V.; Westover, A. S.; Zeier, W. G. Challenges in Lithium Metal Anodes for Solid-State Batteries. *ACS Energy Lett.* **2020**, *5* (3), 922–934. https://doi.org/10.1021/acsenergylett.9b02668.

(64) Wang, C.; Liang, J.; Zhao, Y.; Zheng, M.; Li, X.; Sun, X. All-Solid-State Lithium Batteries Enabled by Sulfide Electrolytes: From Fundamental Research to Practical Engineering Design. *Energy and Environmental Science* **2021**, *14* (5), 2577–2619. https://doi.org/10.1039/d1ee00551k.

(65) Lee, Y. G.; Fujiki, S.; Jung, C.; Suzuki, N.; Yashiro, N.; Omoda, R.; Ko, D. S.; Shiratsuchi, T.; Sugimoto, T.; Ryu, S.; Ku, J. H.; Watanabe, T.; Park, Y.; Aihara, Y.; Im, D.; Han, I. T. High-Energy Long-Cycling All-Solid-State Lithium Metal Batteries Enabled by Silver–

Carbon Composite Anodes. *Nature Energy* **2020**, *5* (4), 299–308. https://doi.org/10.1038/s41560-020-0575-z.

(66) Dussart, T.; Rividi, N.; Fialin, M.; Toussaint, G.; Stevens, P.; Laberty-Robert, C. Critical Current Density Limitation of LLZO Solid Electrolyte: Microstructure vs Interface. *J. Electrochem. Soc.* **2021**, *168* (12), 120550. https://doi.org/10.1149/1945-7111/ac44be.

(67) Shen, F.; Dixit, M. B.; Xiao, X.; Hatzell, K. B. Effect of Pore Connectivity on Li Dendrite Propagation within LLZO Electrolytes Observed with Synchrotron X-Ray Tomography. *ACS Energy Lett.* **2018**, *3* (4), 1056–1061. https://doi.org/10.1021/acsenergylett.8b00249.

(68) Krauskopf, T.; Mogwitz, B.; Rosenbach, C.; Zeier, W. G.; Janek, J. Diffusion Limitation of Lithium Metal and Li–Mg Alloy Anodes on LLZO Type Solid Electrolytes as a Function of Temperature and Pressure. *Adv. Energy Mater.* **2019**, *9* (44), 1902568. https://doi.org/10.1002/aenm.201902568.

(69) Sharafi, A.; Meyer, H. M.; Nanda, J.; Wolfenstine, J.; Sakamoto, J. Characterizing the Li–Li7La3Zr2O12 Interface Stability and Kinetics as a Function of Temperature and Current Density. *Journal of Power Sources* **2016**, *302*, 135–139. https://doi.org/10.1016/j.jpowsour.2015.10.053.

(70) Xu, Z.; Zhang, H.; Yang, T.; Chu, X.; Xie, Y.; Wang, Q.; Xia, Y.; Yang, W. Physicochemically Dendrite-Suppressed Three-Dimensional Fluoridation Solid-State Electrolyte for High-Rate Lithium Metal Battery. *Cell Reports Physical Science* **2021**, *2* (11), 100644. https://doi.org/10.1016/j.xcrp.2021.100644.

(71) Chang, W.; May, R.; Wang, M.; Thorsteinsson, G.; Sakamoto, J.; Marbella, L.; Steingart, D. Evolving Contact Mechanics and Microstructure Formation Dynamics of the Lithium Metal-Li7La3Zr2O12 Interface. *Nat Commun* **2021**, *12* (1), 6369. https://doi.org/10.1038/s41467-021-26632-x.

(72) Wang, J.; Zhang, Z.; Ying, H.; Zhang, S.; Tan, H.; Han, G.; Han, W.-Q. An Effective Artificial Layer Boosting High-Performance All-Solid-State Lithium Batteries with High Coulombic Efficiency. *Journal of Materiomics* **2021**, S2352847821001490. https://doi.org/10.1016/j.jmat.2021.10.006.

(73) Palakkathodi Kammampata, S.; Yamada, H.; Ito, T.; Paul, R.; Thangadurai, V. The Activation Entropy for Ionic Conduction and Critical Current Density for Li Charge

Transfer in Novel Garnet-Type Li $_{6.5}$ La $_{2.9}$ A $_{0.1}$ Zr $_{1.4}$ Ta $_{0.6}$ O $_{12}$ (A = Ca, Sr, Ba) Solid Electrolytes. *J. Mater. Chem. A* **2020**, *8* (5), 2581–2590. https://doi.org/10.1039/C9TA12193E.

(74) Wang, M.; Wolfenstine, J. B.; Sakamoto, J. Temperature Dependent Flux Balance of the Li/Li7La3Zr2O12 Interface. *Electrochimica Acta* **2019**, *296*, 842–847. https://doi.org/10.1016/j.electacta.2018.11.034.

(75) Cheng, L.; Chen, W.; Kunz, M.; Persson, K.; Tamura, N.; Chen, G.; Doeff, M. Effect of Surface Microstructure on Electrochemical Performance of Garnet Solid Electrolytes. *ACS Appl. Mater. Interfaces* **2015**, *7* (3), 2073–2081. https://doi.org/10.1021/am508111r.

(76) Hongahally Basappa, R.; Ito, T.; Morimura, T.; Bekarevich, R.; Mitsuishi, K.; Yamada, H. Grain Boundary Modification to Suppress Lithium Penetration through Garnet-Type Solid Electrolyte. *Journal of Power Sources* **2017**, *363*, 145–152. https://doi.org/10.1016/j.jpowsour.2017.07.088.

(77) Huang, Y.; Chen, B.; Duan, J.; Yang, F.; Wang, T.; Wang, Z.; Yang, W.; Hu, C.; Luo, W.; Huang, Y. Graphitic Carbon Nitride (g-C $_3$ N $_4$): An Interface Enabler for Solid-State Lithium Metal Batteries. *Angew. Chem. Int. Ed.* **2020**, *59* (9), 3699–3704. https://doi.org/10.1002/anie.201914417.

(78) Fu, K. (Kelvin); Gong, Y.; Liu, B.; Zhu, Y.; Xu, S.; Yao, Y.; Luo, W.; Wang, C.; Lacey, S. D.; Dai, J.; Chen, Y.; Mo, Y.; Wachsman, E.; Hu, L. Toward Garnet Electrolyte–Based Li Metal Batteries: An Ultrathin, Highly Effective, Artificial Solid-State Electrolyte/Metallic Li Interface. *Sci. Adv.* **2017**, *3* (4), e1601659. https://doi.org/10.1126/sciadv.1601659.

(79) Wang, C.; Gong, Y.; Dai, J.; Zhang, L.; Xie, H.; Pastel, G.; Liu, B.; Wachsman, E.; Wang, H.; Hu, L. In Situ Neutron Depth Profiling of Lithium Metal–Garnet Interfaces for Solid State Batteries. *J. Am. Chem. Soc.* **2017**, *139* (40), 14257–14264. https://doi.org/10.1021/jacs.7b07904.

(80) Deng, T.; Ji, X.; Zhao, Y.; Cao, L.; Li, S.; Hwang, S.; Luo, C.; Wang, P.; Jia, H.; Fan, X.; Lu, X.; Su, D.; Sun, X.; Wang, C.; Zhang, J. Tuning the Anode–Electrolyte Interface Chemistry for Garnet-Based Solid-State Li Metal Batteries. *Adv. Mater.* **2020**, *32* (23), 2000030. https://doi.org/10.1002/adma.202000030.

(81) Xiong, S.; Liu, Y.; Jankowski, P.; Liu, Q.; Nitze, F.; Xie, K.; Song, J.; Matic, A. Design of a Multifunctional Interlayer for NASCION-Based Solid-State Li Metal Batteries. *Adv. Funct. Mater.* **2020**, *30* (22), 2001444. https://doi.org/10.1002/adfm.202001444.

(82) Ji, X.; Hou, S.; Wang, P.; He, X.; Piao, N.; Chen, J.; Fan, X.; Wang, C. Solid-State Electrolyte Design for Lithium Dendrite Suppression. *Adv. Mater.* **2020**, *32* (46), 2002741. https://doi.org/10.1002/adma.202002741.

(83) Huo, H.; Liang, J.; Zhao, N.; Li, X.; Lin, X.; Zhao, Y.; Adair, K.; Li, R.; Guo, X.; Sun, X. Dynamics of the Garnet/Li Interface for Dendrite-Free Solid-State Batteries. *ACS Energy Lett.* **2020**, *5* (7), 2156–2164. https://doi.org/10.1021/acsenergylett.0c00789.

(84) Yao, X.; Liu, D.; Wang, C.; Long, P.; Peng, G.; Hu, Y.-S.; Li, H.; Chen, L.; Xu, X. High-Energy All-Solid-State Lithium Batteries with Ultralong Cycle Life. *Nano Lett.* **2016**, *16* (11), 7148–7154. https://doi.org/10.1021/acs.nanolett.6b03448.

(85) Kraft, M. A.; Ohno, S.; Zinkevich, T.; Koerver, R.; Culver, S. P.; Fuchs, T.; Senyshyn, A.; Indris, S.; Morgan, B. J.; Zeier, W. G. Inducing High Ionic Conductivity in the Lithium Superionic Argyrodites $Li_{6+x}P_{1-x}Ge_xS_5I$ for All-Solid-State Batteries. *J. Am. Chem. Soc.* **2018**, *140* (47), 16330–16339. https://doi.org/10.1021/jacs.8b10282.

(86) Zhang, W.; Weber, D. A.; Weigand, H.; Arlt, T.; Manke, I.; Schröder, D.; Koerver, R.; Leichtweiss, T.; Hartmann, P.; Zeier, W. G.; Janek, J. Interfacial Processes and Influence of Composite Cathode Microstructure Controlling the Performance of All-Solid-State Lithium Batteries. *ACS Appl. Mater. Interfaces* **2017**, *9* (21), 17835–17845. https://doi.org/10.1021/acsami.7b01137.

(87) Su, Y.; Ye, L.; Fitzhugh, W.; Wang, Y.; Gil-González, E.; Kim, I.; Li, X. A More Stable Lithium Anode by Mechanical Constriction for Solid State Batteries. *Energy Environ. Sci.* **2020**, *13* (3), 908–916. https://doi.org/10.1039/C9EE04007B.

(88) Hitz, G. T.; McOwen, D. W.; Zhang, L.; Ma, Z.; Fu, Z.; Wen, Y.; Gong, Y.; Dai, J.; Hamann, T. R.; Hu, L.; Wachsman, E. D. High-Rate Lithium Cycling in a Scalable Trilayer Li-Garnet-Electrolyte Architecture. *Materials Today* **2019**, *22*, 50–57. https://doi.org/10.1016/j.mattod.2018.04.004.

(89) Peng, J.; Wu, D.; Song, F.; Wang, S.; Niu, Q.; Xu, J.; Lu, P.; Li, H.; Chen, L.; Wu, F. High Current Density and Long Cycle Life Enabled by Sulfide Solid Electrolyte and Dendrite-

Free Liquid Lithium Anode. *Adv Funct Materials* **2022**, *32* (2), 2105776. https://doi.org/10.1002/adfm.202105776.

(90) Ye, L.; Li, X. A Dynamic Stability Design Strategy for Lithium Metal Solid State Batteries. *Nature* **2021**, *593* (7858), 218–222. https://doi.org/10.1038/s41586-021-03486-3.

(91) Tan, D. H. S.; Chen, Y.-T.; Yang, H.; Bao, W.; Sreenarayanan, B.; Doux, J.-M.; Li, W.; Lu, B.; Ham, S.-Y.; Sayahpour, B.; Scharf, J.; Wu, E. A.; Deysher, G.; Han, H. E.; Hah, H. J.; Jeong, H.; Lee, J. B.; Chen, Z.; Meng, Y. S. Carbon-Free High-Loading Silicon Anodes Enabled by Sulfide Solid Electrolytes. *Science* **2021**, *373* (6562), 1494–1499. https://doi.org/10.1126/science.abg7217.

(92) Lu, Y.; Zhao, C.; Yuan, H.; Cheng, X.; Huang, J.; Zhang, Q. Critical Current Density in Solid-State Lithium Metal Batteries: Mechanism, Influences, and Strategies. *Adv. Funct. Mater.* **2021**, *31* (18), 2009925. https://doi.org/10.1002/adfm.202009925.

(93) Lewis, J. A.; Lee, C.; Liu, Y.; Han, S. Y.; Prakash, D.; Klein, E. J.; Lee, H.-W.; McDowell, M. T. Role of Areal Capacity in Determining Short Circuiting of Sulfide-Based Solid-State Batteries. *ACS Appl. Mater. Interfaces* **2022**, *14* (3), 4051–4060. https://doi.org/10.1021/acsami.1c20139.

(94) Chen, Y.; Li, W.; Sun, C.; Jin, J.; Wang, Q.; Chen, X.; Zha, W.; Wen, Z. Sustained Release-Driven Formation of Ultrastable SEI between Li $_6$ PS $_5$ Cl and Lithium Anode for Sulfide-Based Solid-State Batteries. *Adv. Energy Mater.* **2021**, *11* (4), 2002545. https://doi.org/10.1002/aenm.202002545.

(95) Chen, Y.; Yao, L.; Chen, X.; Jin, J.; Wu, M.; Wang, Q.; Zha, W.; Wen, Z. Double-Faced Bond Coupling to Induce an Ultrastable Lithium/Li $_6$ PS $_5$ Cl Interface for High-Performance All-Solid-State Batteries. *ACS Appl. Mater. Interfaces* **2022**, *14* (9), 11950–11961. https://doi.org/10.1021/acsami.1c24506.

(96) Kasemchainan, J.; Zekoll, S.; Spencer Jolly, D.; Ning, Z.; Hartley, G. O.; Marrow, J.; Bruce, P. G. Critical Stripping Current Leads to Dendrite Formation on Plating in Lithium Anode Solid Electrolyte Cells. *Nat. Mater.* **2019**, *18* (10), 1105–1111. https://doi.org/10.1038/s41563-019-0438-9.

(97) Wang, M. J.; Choudhury, R.; Sakamoto, J. Characterizing the Li-Solid-Electrolyte Interface Dynamics as a Function of Stack Pressure and Current Density. *Joule* **2019**, *3* (9), 2165–2178. https://doi.org/10.1016/j.joule.2019.06.017.

(98) Yan, H.; Tantratian, K.; Ellwood, K.; Harrison, E. T.; Nichols, M.; Cui, X.; Chen, L. How Does the Creep Stress Regulate Void Formation at the Lithium-Solid Electrolyte Interface during Stripping? *Advanced Energy Materials* **2022**, *12* (2), 2102283. https://doi.org/10.1002/aenm.202102283.

(99) LePage, W. S.; Chen, Y.; Kazyak, E.; Chen, K.-H.; Sanchez, A. J.; Poli, A.; Arruda, E. M.; Thouless, M. D.; Dasgupta, N. P. Lithium Mechanics: Roles of Strain Rate and Temperature and Implications for Lithium Metal Batteries. *J. Electrochem. Soc.* **2019**, *166* (2), A89–A97. https://doi.org/10.1149/2.0221902jes.

(100) Liu, G.; Weng, W.; Zhang, Z.; Wu, L.; Yang, J.; Yao, X. Densified Li6PS5Cl Nanorods with High Ionic Conductivity and Improved Critical Current Density for All-Solid-State Lithium Batteries. *Nano Letters* **2020**, *20* (9), 6660–6665. https://doi.org/10.1021/acs.nanolett.0c02489.

(101) Xu, B.; Li, X.; Yang, C.; Li, Y.; Grundish, N. S.; Chien, P.-H.; Dong, K.; Manke, I.; Fang, R.; Wu, N.; Xu, H.; Dolocan, A.; Goodenough, J. B. Interfacial Chemistry Enables Stable Cycling of All-Solid-State Li Metal Batteries at High Current Densities. *J. Am. Chem. Soc.* **2021**, *143* (17), 6542–6550. https://doi.org/10.1021/jacs.1c00752.

(102) Lu, Y.; Zhao, C. Z.; Yuan, H.; Cheng, X. B.; Huang, J. Q.; Zhang, Q. Critical Current Density in Solid-State Lithium Metal Batteries: Mechanism, Influences, and Strategies. *Advanced Functional Materials* **2021**. https://doi.org/10.1002/adfm.202009925.

(103) Lee, J. Z.; Wynn, T. A.; Schroeder, M. A.; Alvarado, J.; Wang, X.; Xu, K.; Meng, Y. S. Cryogenic Focused Ion Beam Characterization of Lithium Metal Anodes. *ACS Energy Letters* **2019**, *4* (2), 489–493. https://doi.org/10.1021/acsenergylett.8b02381.

(104) Ding, S.; Fairgrieve-Park, L.; Sendetskyi, O.; Fleischauer, M. D. Compressive Creep Deformation of Lithium Foil at Varied Cell Conditions. *Journal of Power Sources* **2021**, *488*, 229404. https://doi.org/10.1016/j.jpowsour.2020.229404.

(105) Zhang, X.; Wang, Q. J.; Harrison, K. L.; Roberts, S. A.; Harris, S. J. Pressure-Driven Interface Evolution in Solid-State Lithium Metal Batteries. *Cell Reports Physical Science* **2020**, *1* (2), 100012. https://doi.org/10.1016/j.xcrp.2019.100012.

(106) Chen, S.; Niu, C.; Lee, H.; Li, Q.; Yu, L.; Xu, W.; Zhang, J.-G.; Dufek, E. J.; Whittingham, M. S.; Meng, S.; Xiao, J.; Liu, J. Critical Parameters for Evaluating Coin Cells and Pouch Cells of Rechargeable Li-Metal Batteries. *Joule* **2019**, *3* (4), 1094–1105. https://doi.org/10.1016/j.joule.2019.02.004.

(107) Banerjee, A.; Wang, X.; Fang, C.; Wu, E. A.; Meng, Y. S. Interfaces and Interphases in All-Solid-State Batteries with Inorganic Solid Electrolytes. *Chem. Rev.* **2020**, *120* (14), 6878–6933. https://doi.org/10.1021/acs.chemrev.0c00101.

(108) Lewis, J. A.; Cavallaro, K. A.; Liu, Y.; McDowell, M. T. The Promise of Alloy Anodes for Solid-State Batteries. *Joule* **2022**, *6* (7), 1418–1430. https://doi.org/10.1016/j.joule.2022.05.016.

(109) Huang, Y.; Shao, B.; Han, F. Li Alloy Anodes for High-Rate and High-Areal-Capacity Solid-State Batteries. *J. Mater. Chem. A* **2022**, *10* (23), 12350–12358. https://doi.org/10.1039/D2TA02339C.

(110) Lee, Y.-G.; Fujiki, S.; Jung, C.; Suzuki, N.; Yashiro, N.; Omoda, R.; Ko, D.-S.; Shiratsuchi, T.; Sugimoto, T.; Ryu, S.; Ku, J. H.; Watanabe, T.; Park, Y.; Aihara, Y.; Im, D.; Han, I. T. High-Energy Long-Cycling All-Solid-State Lithium Metal Batteries Enabled by Silver–Carbon Composite Anodes. *Nat Energy* **2020**, *5* (4), 299–308. https://doi.org/10.1038/s41560-020-0575-z.

(111) Iwamura, S.; Nishihara, H.; Ono, Y.; Morito, H.; Yamane, H.; Nara, H.; Osaka, T.; Kyotani, T. Li-Rich Li-Si Alloy As A Lithium-Containing Negative Electrode Material Towards High Energy Lithium-Ion Batteries. *Sci Rep* **2015**, *5* (1), 8085. https://doi.org/10.1038/srep08085.

(112) Wang, G.; Xu, B.; Shi, J.; Wu, M.; Su, H.; Ouyang, C. New Insights into Li Diffusion in Li–Si Alloys for Si Anode Materials: Role of Si Microstructures. *Nanoscale* **2019**, *11* (29), 14042–14049. https://doi.org/10.1039/C9NR03986D.

(113) Jing, W.; Zou, K.; Dai, X.; Sun, J.; Tan, Q.; Chen, Y.; Liu, Y. Li-Indium Alloy Anode for High-Performance Li-Metal Batteries. *Journal of Alloys and Compounds* **2022**, *924*, 166517. https://doi.org/10.1016/j.jallcom.2022.166517.

(114) Luo, S.; Wang, Z.; Li, X.; Liu, X.; Wang, H.; Ma, W.; Zhang, L.; Zhu, L.; Zhang, X. Growth of Lithium-Indium Dendrites in All-Solid-State Lithium-Based Batteries with Sulfide Electrolytes. *Nat Commun* **2021**, *12* (1), 6968. https://doi.org/10.1038/s41467-021-27311-7.

(115) Il'ina, E.; Druzhinin, K.; Lyalin, E.; Talankin, I. In Situ Li-In Anode Formation on the Li7La3Zr2O12 Solid Electrolyte in All-Solid-State Battery. *Batteries* **2022**, *8* (11), 226. https://doi.org/10.3390/batteries8110226.

(116) Sedlmeier, C.; Schuster, R.; Schramm, C.; Gasteiger, H. A. A Micro-Reference Electrode for Electrode-Resolved Impedance and Potential Measurements in All-Solid-State Battery Pouch Cells and Its Application to the Study of Indium-Lithium Anodes. *J. Electrochem. Soc.* **2023**, *170* (3), 030536. https://doi.org/10.1149/1945-7111/acc699.

(117) Mou, H.; Xiao, W.; Miao, C.; Li, R.; Yu, L. Tin and Tin Compound Materials as Anodes in Lithium-Ion and Sodium-Ion Batteries: A Review. *Front. Chem.* **2020**, *8*, 141. https://doi.org/10.3389/fchem.2020.00141.

(118) Pan, H.; Zhang, M.; Cheng, Z.; Jiang, H.; Yang, J.; Wang, P.; He, P.; Zhou, H. Carbon-Free and Binder-Free Li-Al Alloy Anode Enabling an All-Solid-State Li-S Battery with High Energy and Stability. *Sci. Adv.* **2022**, *8* (15), eabn4372. https://doi.org/10.1126/sciadv.abn4372.

(119) Chen, S.; Yang, X.; Zhang, J.; Ma, J.; Meng, Y.; Tao, K.; Li, F.; Geng, J. Aluminum−lithium Alloy as a Stable and Reversible Anode for Lithium Batteries. *Electrochimica Acta* **2021**, *368*, 137626. https://doi.org/10.1016/j.electacta.2020.137626.

(120) He, J.; Wei, Y.; Zhai, T.; Li, H. Antimony-Based Materials as Promising Anodes for Rechargeable Lithium-Ion and Sodium-Ion Batteries. *Mater. Chem. Front.* **2018**, *2* (3), 437–455. https://doi.org/10.1039/C7QM00480J.

(121) Kong, L.; Wang, L.; Ni, Z.; Liu, S.; Li, G.; Gao, X. Lithium–Magnesium Alloy as a Stable Anode for Lithium–Sulfur Battery. *Adv. Funct. Mater.* **2019**, *29* (13), 1808756. https://doi.org/10.1002/adfm.201808756.

(122) Zhang, C.; Wang, F.; Han, J.; Bai, S.; Tan, J.; Liu, J.; Li, F. Challenges and Recent Progress on Silicon-Based Anode Materials for Next-Generation Lithium-Ion Batteries. *Small Structures* **2021**, *2* (6), 2100009. https://doi.org/10.1002/sstr.202100009.

(123) Zhang, X.; Wang, D.; Qiu, X.; Ma, Y.; Kong, D.; Müllen, K.; Li, X.; Zhi, L. Stable High-Capacity and High-Rate Silicon-Based Lithium Battery Anodes upon Two-Dimensional Covalent Encapsulation. *Nat Commun* **2020**, *11* (1), 3826. https://doi.org/10.1038/s41467-020-17686-4.

(124) Berhaut, C. L.; Dominguez, D. Z.; Tomasi, D.; Vincens, C.; Haon, C.; Reynier, Y.; Porcher, W.; Boudet, N.; Blanc, N.; Chahine, G. A.; Tardif, S.; Pouget, S.; Lyonnard, S. Prelithiation of Silicon/Graphite Composite Anodes: Benefits and Mechanisms for Long-Lasting Li-Ion Batteries. *Energy Storage Materials* **2020**, *29*, 190–197. https://doi.org/10.1016/j.ensm.2020.04.008.

(125) Min, X.; Xu, G.; Xie, B.; Guan, P.; Sun, M.; Cui, G. Challenges of Prelithiation Strategies for next Generation High Energy Lithium-Ion Batteries. *Energy Storage Materials* **2022**, *47*, 297–318. https://doi.org/10.1016/j.ensm.2022.02.005.

(126) Pan, Q.; Zuo, P.; Mu, T.; Du, C.; Cheng, X.; Ma, Y.; Gao, Y.; Yin, G. Improved Electrochemical Performance of Micro-Sized SiO-Based Composite Anode by Prelithiation of Stabilized Lithium Metal Powder. *Journal of Power Sources* **2017**, *347*, 170–177. https://doi.org/10.1016/j.jpowsour.2017.02.061.

(127) Sun, C.; Zhang, X.; Li, C.; Wang, K.; Sun, X.; Ma, Y. Recent Advances in Prelithiation Materials and Approaches for Lithium-Ion Batteries and Capacitors. *Energy Storage Materials* **2020**, *32*, 497–516. https://doi.org/10.1016/j.ensm.2020.07.009.

(128) Yang, S.-Y.; Yue, X.-Y.; Xia, H.-Y.; Li, X.-L.; Wang, T.; Li, H.; Fu, Z.-W. Battery Prelithiation Enabled by Lithium Fixation on Cathode. *Journal of Power Sources* **2020**, *480*, 229109. https://doi.org/10.1016/j.jpowsour.2020.229109.

(129) Liu, Q.; Du, C.; Shen, B.; Zuo, P.; Cheng, X.; Ma, Y.; Yin, G.; Gao, Y. Understanding Undesirable Anode Lithium Plating Issues in Lithium-Ion Batteries. *RSC Adv.* **2016**, *6* (91), 88683–88700. https://doi.org/10.1039/C6RA19482F.

(130) Cao, Z.; Xu, P.; Zhai, H.; Du, S.; Mandal, J.; Dontigny, M.; Zaghib, K.; Yang, Y. Ambient-Air Stable Lithiated Anode for Rechargeable Li-Ion Batteries with High Energy

Density. *Nano Lett.* **2016**, *16* (11), 7235–7240. https://doi.org/10.1021/acs.nanolett.6b03655.

(131) Ai, G.; Wang, Z.; Zhao, H.; Mao, W.; Fu, Y.; Yi, R.; Gao, Y.; Battaglia, V.; Wang, D.; Lopatin, S.; Liu, G. Scalable Process for Application of Stabilized Lithium Metal Powder in Li-Ion Batteries. *Journal of Power Sources* **2016**, *309*, 33–41. https://doi.org/10.1016/j.jpowsour.2016.01.061.

(132) Forney, M. W.; Ganter, M. J.; Staub, J. W.; Ridgley, R. D.; Landi, B. J. Prelithiation of Silicon–Carbon Nanotube Anodes for Lithium Ion Batteries by Stabilized Lithium Metal Powder (SLMP). *Nano Lett.* **2013**, *13* (9), 4158–4163. https://doi.org/10.1021/nl401776d.

(133) Bärmann, P.; Mohrhardt, M.; Frerichs, J. E.; Helling, M.; Kolesnikov, A.; Klabunde, S.; Nowak, S.; Hansen, M. R.; Winter, M.; Placke, T. Mechanistic Insights into the Pre-Lithiation of Silicon/Graphite Negative Electrodes in "Dry State" and After Electrolyte Addition Using Passivated Lithium Metal Powder. *Adv. Energy Mater.* **2021**, *11* (25), 2100925. https://doi.org/10.1002/aenm.202100925.

(134) Ji, W.; Zhang, X.; Liu, M.; Ding, T.; Qu, H.; Qiu, D.; Zheng, D.; Qu, D. High-Performance All-Solid-State Li–S Batteries Enabled by an All-Electrochem-Active Prelithiated Si Anode. *Energy Storage Materials* **2022**, *53*, 613–620. https://doi.org/10.1016/j.ensm.2022.10.003.

(135) Jang, E.; Ryu, S.; Kim, M.; Choi, J.; Yoo, J. Silicon-Stabilized Lithium Metal Powder (SLMP) Composite Anodes for Fast Charging by in-Situ Prelithiation. *Journal of Power Sources* **2023**, *580*, 233326. https://doi.org/10.1016/j.jpowsour.2023.233326.

(136) Lee, J.; Jin, D.; Kim, J. Y.; Roh, Y.; Lee, H.; Kang, S. H.; Choi, J.; Jo, T.; Lee, Y.; Lee, Y. M. Dry Pre-Lithiation for Graphite-Silicon Diffusion-Dependent Electrode for All-Solid-State Battery. *Advanced Energy Materials* **2023**, *13* (25), 2300172. https://doi.org/10.1002/aenm.202300172.

(137) Hope, M. A.; Rinkel, B. L. D.; Gunnarsdóttir, A. B.; Märker, K.; Menkin, S.; Paul, S.; Sergeyev, I. V.; Grey, C. P. Selective NMR Observation of the SEI–Metal Interface by Dynamic Nuclear Polarisation from Lithium Metal. *Nat Commun* **2020**, *11* (1), 2224. https://doi.org/10.1038/s41467-020-16114-x.

(138) R. Lide, D. In *CRC Handbook of Chemistry and Physics*; CRC Press: Boca Raton, Florida, 2003; p Section 12, Properties of Solids; Electrical Resistivity of Pure Metals.

(139) Gunnarsdóttir, A. B.; Amanchukwu, C. V.; Menkin, S.; Grey, C. P. Noninvasive *In Situ* NMR Study of "Dead Lithium" Formation and Lithium Corrosion in Full-Cell Lithium Metal Batteries. *J. Am. Chem. Soc.* **2020**, *142* (49), 20814–20827. https://doi.org/10.1021/jacs.0c10258.

(140) Meyer, B. M.; Leifer, N.; Sakamoto, S.; Greenbaum, S. G.; Grey, C. P. High Field Multinuclear NMR Investigation of the SEI Layer in Lithium Rechargeable Batteries. *Electrochem. Solid-State Lett.* **2005**, *8* (3), A145. https://doi.org/10.1149/1.1854117.

(141) Kim, H. J.; Choi, S.; Lee, S. J.; Seo, M. W.; Lee, J. G.; Deniz, E.; Lee, Y. J.; Kim, E. K.; Choi, J. W. Controlled Prelithiation of Silicon Monoxide for High Performance Lithium-Ion Rechargeable Full Cells. *Nano Lett.* **2016**, *16* (1), 282–288. https://doi.org/10.1021/acs.nanolett.5b03776.

(142) Key, B.; Bhattacharyya, R.; Morcrette, M.; Seznéc, V.; Tarascon, J.-M.; Grey, C. P. Real-Time NMR Investigations of Structural Changes in Silicon Electrodes for Lithium-Ion Batteries. *J. Am. Chem. Soc.* **2009**, *131* (26), 9239–9249. https://doi.org/10.1021/ja8086278.

(143) Park, K.-Y.; Park, J.-W.; Seong, W. M.; Yoon, K.; Hwang, T.-H.; Ko, K.-H.; Han, J.-H.; Jaedong, Y.; Kang, K. Understanding Capacity Fading Mechanism of Thick Electrodes for Lithium-Ion Rechargeable Batteries. *Journal of Power Sources* **2020**, *468*, 228369. https://doi.org/10.1016/j.jpowsour.2020.228369.

(144) Kim, H.; Oh, S. K.; Lee, J.; Doo, S. W.; Kim, Y.; Lee, K. T. Failure Mode of Thick Cathodes for Li-Ion Batteries: Variation of State-of-Charge along the Electrode Thickness Direction. *Electrochimica Acta* **2021**, *370*, 137743. https://doi.org/10.1016/j.electacta.2021.137743.

(145) Yao, W.; Chouchane, M.; Li, W.; Bai, S.; Liu, Z.; Li, L.; Chen, A. X.; Sayahpour, B.; Shimizu, R.; Raghavendran, G.; Schroeder, M. A.; Chen, Y.-T.; Tan, D. H. S.; Sreenarayanan, B.; Waters, C. K.; Sichler, A.; Gould, B.; Kountz, D. J.; Lipomi, D. J.; Zhang, M.; Meng, Y. S. A 5 V-Class Cobalt-Free Battery Cathode with High Loading Enabled by Dry Coating. *Energy Environ. Sci.* **2023**, *16* (4), 1620–1630. https://doi.org/10.1039/D2EE03840D.